DESIGN OF A GAS DIFFUSION LAYER FOR A POLYMER ELECROLYTE MEMBRANE FUEL CELL WITH A GRADUATED RESISTANCE TO FLOW

A Thesis
Presented to
The Academic Faculty

by

Terry Brett Caston

In Partial Fulfillment
of the Requirements for the Degree
Master of Science in the
School of Mechanical Engineering

Georgia Institute of Technology
August 2010

DESIGN OF A GAS DIFFUSION LAYER FOR A POLYMER ELECROLYTE MEMBRANE FUEL CELL WITH A GRADUATED RESISTANCE TO FLOW

Approved by:

Dr. Tequila Harris, Advisor
School of Mechanical Engineering
Georgia Institute of Technology

Dr. Sankar Nair
School of Chemical and Biomolecular Engineering
Georgia Institute of Technology

Dr. Mostafa Ghiaasiaan
School of Mechanical Engineering
Georgia Institute of Technology

Date Approved: April 19, 2010

To the advancement of renewable energy.

ACKNOWLEDGEMENTS

I have received a great deal of support throughout the course of this project. First, I would like to thank my research advisor, Dr. Tequila Harris, for her guidance through my research and my educational development and the engaging discussions that directed my path through the project. I would also like to thank my committee members, Dr. Mostafa Ghiaasiaan and Dr. Sankar Nair for taking the time to review my thesis and for their suggestions.

I would like extend my gratitude to Haley Carney for her help in developing the weaving project and her insight into the technique and design of experiments. I would like acknowledge Dr. Michael Ellis from the Virginia Polytechnic Institute for allowing us to use his lab and equipment in evaluating the potential for the manufacture of woven gas diffusion layers. I would like to thank Cytec Inc. for supplying our group with the T-300 carbon fiber to run the experiments. I must acknowledge Jeff Gostick for his invaluable help with trouble shooting our test system and for taking the time to help us understand the test set-up. The experimental test set-up would not have been possible without the help of Louie Boulanger and John Graham in the machine shop, who built the test equipment for the permeability experiments. Finally, it would have been impossible to finish the experiments without the dedication of Andrew Murphy, who conducted a significant amount of the experiments and whose suggestions helped establish the technique.

I would like to acknowledge Kanthi Bhamidipati for her help with the Fluent study and the brain storming sessions which helped advance the project tremendously. I

would also like to thank Jay Johnson for his insight into the project and the rest of the Dames Lab for providing an enjoyable and inspiring work environment. I would also like to extend my thanks to Azam Thatte, whose knowledge of Comsol was invaluable in finishing the simulations and anybody else at the Georgia Institute of Technology who helped me throughout the course of this project.

Lastly I would like to thank my parents and friends for their love and support. My parents have always supported me to do what makes me happy and gives me a sense of purpose, and I would not be where I am today without them. Most importantly, I am grateful for my wife, Sarah, whose unconditional love and encouragement inspired me through the best and most difficult times.

TABLE OF CONTENTS

ACKNOWLEDGEMENTS **iv**
LIST OF TABLES **ix**
LIST OF FIGURES **xi**
NOMENCLATURE **xv**
SUMMARY **xixx**
CHAPTER 1: INTRODUCTION **1**
1.1 Energy Situation and Renewable Energy Sources 1
1.2 Fuel Cells 3
1.2.1 Fuel Cell Types 4
1.3 PEM Fuel Cell Components 5
1.3.1 Bipolar Plate 6
1.3.2 Gas Diffusion Layer 8
1.3.3 Catalyst Layer 8
1.3.4 Membrane 8
1.4 Limitations to Growth 9
1.5 Motivation for this Work 10
1.6 Structure of the Thesis 14
CHAPTER 2: LITERATURE REVIEW **16**
2.1 Introduction 16
2.2 Fuel Cell Performance 16
2.2.1 Nernst Potential 16
2.2.2 The Polarization Curve and Irreversibilities 18
2.3 Fuel Cell Modeling Methodology 20
2.3.1 Zero Dimensional Models 20
2.3.2 One Dimensional Sandwich Models 21
2.3.3 Two Dimensional Flow Models 22
2.3.4 Three Dimensional Flow Models 23
2.4 Diffusion Media Modeling 24
2.5 Models with Varying Porosity and Permeability 27
2.5.1 Porosity Gradient Models 28
2.5.2 Compressed GDL Models 31
2.5.3 Anisotropic Permeability Modeling 33
2.6 Permeability Testing 35
2.6.1 Experimental Permeability Testing 35
2.6.2 Permeability of Woven Structures 44
2.7 Summary 47
CHAPTER 3: FLUENT MODEL WITH CHANGE IN PERMEABILITY **48**
3.1 Motivation 48
3.2 Computational Model 49
3.2.1 Modeling Domain 49
3.2.2 Problem Solving Methodology 51
3.2.3 Modeling Assumptions 53

3.2.3.1 Isothermal Assumption 54
3.2.4 Governing Equations 55
3.2.4.1 Continuity 56
3.2.4.2 Momentum and Mass Transport 57
3.2.5 Boundary Conditions 57
3.2.6 Validation Study 58
3.3 Simulations 60
3.3.1 Effects of Graduating Permeability on Distribution 62
3.3.2 Effect of Changing Thickness 66
3.3.3 Effect of Gas Stoichiometry 68
3.3.4 Conclusions 70
CHAPTER 4: FULLY COUPLED 3-D COMSOL MODEL 72
4.1 Motivation 72
4.1.1 Changes from Previous Model 73
4.2 Modeling Parameter Study (Operating Conditions) 73
4.3 Computational Model 77
4.3.1 Modeling Domain 78
4.3.2 Modeling Assumptions 79
4.3.3 Governing Equations 79
4.3.3.1 Continuity 80
4.3.3.2 Charge Transport 80
4.3.3.3 Mass and Momentum Transport 81
4.3.3 Boundary Conditions 82
4.3.4 Model Solution 83
4.3.5 Grid Independence and Validation 84
4.3.5.1 Grid Independence 84
4.3.5.2 Validation 87
4.4 Results 88
4.4.1 Permeability Profiles 89
4.4.2 Scaling of the Cell 92
4.4.3 Effect of Changing Permeability Profiles 93
4.4.4 Effect of GDL Thickness 96
4.4.5 Effect of Gas Stoichiometry 97
4.4.6 Comparison to Parallel and Serpentine Flow Field 99
4.4.7 Tradeoff with Pressure Drop 103
4.5 Conclusions 105
CHAPTER 5: EXPERIMENTAL PERMEABILITY TESTING 107
5.1 Introduction and Motivation 107
5.2 Methodology 107
5.2.1 Through-Plane Permeability Test Set-up 108
5.2.2 In-Plane Permeability Test Set-up 109
5.2.3 Hand Loom 111
5.2.4 Materials 112
5.3 Analysis 112
5.3.1 Darcy-Forchheimer Formulation: Permeability 113
5.3.2 Calculation of Uncompressed Porosity for In-Plane Tests 115

5.4 Design of Experiments 117
5.5 Through-Plane Permeability Results 119
5.5.1 Validation 119
5.5.2 Through-Plane Permeability of Woven GDLs 120
5.6 In Plane Permeability Results 123
5.6.1 Validation 123
5.6.2 In-plane Permeability of Woven GDLs 124
5.6.3 Mercury Intrusion Porosimetry Measurements 127
CHAPTER 6: CONCLUSIONS 133
6.1 Overall Conclusions 133
6.2 Contributions 135
CHAPTER 7: FUTURE WORK 137
7.1 Simulations 137
7.2 Permeability Testing 139
REFERENCES 140

LIST OF TABLES

Table 1: Comparison of Power Density from Different Fuel Cell Stack Designs [22] 13

Table 2: Operating Conditions and Design Parameters 52

Table 3: Operating Conditions for Validation Model 59

Table 4: Permeability Values in GDL (m^2) 62

Table 5: Ratio of Standard Deviation of Current Density at Varying Thicknesses 67

Table 6: Ratio of Standard Deviation of Current Density to Average Current Density for Different Gas Stoichiometries 69

Table 7: Modeling Parameter Study 74

Table 8: Operating Conditions and Modeling Parameters 77

Table 9: Different Mesh Patterns and Corresponding Aspect Ratio 85

Table 10: Ratio of Standard Deviation of Current Density/Average Current Density at Different Cell Sizes 93

Table 11: Design of Experiments for Simulations 94

Table 12: Effect of Graduating Permeability with Unconventional GDL 94

Table 13: Current Density with GDLs of Varying Isotropic Permeability 95

Table 14: Current Density at Varying GDL Thickness 97

Table 15: Current Density at Different Air Stoichiometries 99

Table 16: Current Density Comparing the Unconventional Model with Graduated Permeability to a State-of-the-Art Parallel Channel Model 100

Table 17: Comparison of Range of Current Density Distribution 102

Table 18: Effect of Permeability Profile on Pressure Drop 104

Table 19: Effect of Flow Field Design on Pressure Drop 105

Table 20: Weave Samples 118

Table 21: Through-Plane Permeability of Woven Samples 121

Table 22: Uncompressed In-Plane Permeability for Woven Patterns 126

Table 23: Percentage of Each Type of Pore Based on Mercury Intrusion Porosimetry . 131

Table 24: Current Density as a Function of Rate of Consumption, ai_{0c} 138

LIST OF FIGURES

Figure 1: US Electricity Generation by Fuel, adapted from Data Given in [1] 2

Figure 2: Energy Conversion Process for (a) Combustion Engine and (b) Fuel Cell..... 4

Figure 3: Schematic of a PEM Fuel Cell 6

Figure 4: Flow Field Designs [7] 7

Figure 5: (a) Stack Design by Bhamidipati et al. [22] (b) Traditional Stack with Internal Manifolding, adapted from [23]..... 11

Figure 6: Close-up of Manifolds and GDLS in New Stack Design..... 12

Figure 7: Polarization Curve adapted from [24] 18

Figure 8: Typical One Dimensional Sandwich Model adapted from [25]..... 21

Figure 9: (Along the Channel Model and (b) Under-the-Rib Model [6] 23

Figure 10: Three Dimensional Under-the-Rib Model Showing Velocity Profile and Mass Fractions of Oxygen at a Cross-Section in a Channel adapted from [26] 24

Figure 11: Simulation Configuration for Chen et al. adapted from [43] 28

Figure 12: Polarization Curve for Different Values of ε_l adapted from [43] 29

Figure 13: Porosity Distribution as Function of Position for 4 Models adapted from [44] 30

Figure 14: Effect of Porosity Change Model on Polarization Curve adapted from [44].. 30

Figure 15: (a) Photograph of GDL under Compression [49] and (b) Model of GDL Under Compression adapted from [27]..... 32

Figure 16: Oxygen Molar Fraction at GDL/Catalyst Layer Interface at a Cell Voltage of 0.5 V [49]..... 33

Figure 17: Effect of Anisotropic Permeability on Channel Pressure Drop [42]..... 34

Figure 18: Radial Flow Apparatus used by Feser [50] 35

Figure 19: Permeability vs. Compression for Various GDLs [50] 36

Figure 20: Pressure Gradient vs. Velocity for Various Carbon Cloth Samples [51] 37

Figure 21: Through-Plane Permeability Test Set-Up [52] 38

Figure 22: Pressure Gradient vs. Mass Flux for Through-Plane Permeability of GDL Samples [52] 39

Figure 23: Limiting Current vs. Permeability Coefficient for GDLs [53] 40

Figure 24: Pore Volume vs. Permeability Coefficient for Measured GDLs [53] 41

Figure 25: (a) In-Plane Permeability Testing Device, (b) Exploded View, and (c) Cutout View of the Inside of the Device [34] 42

Figure 26: Pressure Gradient vs. Mass Flux for SGL 34BA [34] 42

Figure 27: Permeabiliity vs. (a) Compressed Volume Fraction and (b) Porosity [34] 43

Figure 28: (a) Through-Plane Permeability Measurement Device, (b) Exploded View, and (c) Cutout View [34] 43

Figure 29: Diagram of Plain-Woven Fabric adapted from [54] 45

Figure 30: Twill Weave 46

Figure 31: Side View of Modeling Domain 50

Figure 32: GDL and Catalyst with Subdomains Labeled 51

Figure 33: Polarization Curve 53

Figure 34: Interdigitated Flow Field Polarization Curve Developed by Wang et al. [61] 59

Figure 35: Mass Flux of Oxygen into Cathode Catalyst Layer vs. Position at 11.5 mm Cross Section 60

Figure 36: Effects of Varying Permeability on Current Density Distribution with a 0.4 mm Thick GDL at 1.33 Gas Stoichiometry: (1) Case 1, (b) Case 2, (c) Case 3, and (d) Conventional Case [62] 64

Figure 37: Average Current Density with Standard Deviation of Current Density for Each Case 65

Figure 38: Average Current Density at Different Thicknesses 66

Figure 39: Gas Stoichiometry vs. Average Current Density 69

Figure 40: Modeling Domain..... 78

Figure 41: 3-D Modeling Domain with GDL, Catalyst and Membrane..... 79

Figure 42: Solution Method adapted from [38] 84

Figure 43: Effect of Changing Number of Elements in the In-Plane and Through-Plane 86

Figure 44: Validation 87

Figure 45: In-Plane x- Permeability Profiles as a Function of x- Position 90

Figure 46: Through-Plane z- Permeability as a Function of x- Position 91

Figure 47: Effect of Changing the Size of the Cell on the Average Current Density..... 93

Figure 48: Effect of GDL Thickness on Average Current Density 96

Figure 49: Stoichiometry vs. Average Current Density..... 98

Figure 50: Parallel Flow Field 100

Figure 51: Current Density Profile for (a) Unconventional GDL and (b) Parallel Flow Field 101

Figure 52: (a) Through-Plane Permeability Set-up and (b) Close up of the Device with Mass Flow Controller and Differential Pressure Sensor..... 109

Figure 53: (a) In-Plane Permeability Test Set-up and (b) In-Plane Permeability Test Device 111

Figure 54: Hand Loom Used to Weave the Woven GDLs 112

Figure 55: Representative Plot for Permeability Test..... 115

Figure 56: Mass Flux vs. Pressure Gradient Term for Twill 8x4 at 3 Levels of Compression 116

Figure 57: Permeability vs. Porosity for a Twill 8x8 Weave 117

Figure 58: Plain-Woven Fabric with a Tightness of 8x8..... 118

Figure 59: Pressure Gradient Term vs. Mass Flux for Validation..... 120

Figure 60: Through-Plane Permeability of Twill Woven GDL with Varying Tightness 122

Figure 61: Through-Plane Permeability of Plain Woven GDL with Varying Tightness 122

Figure 62: Pressure Gradient Term vs. Mass Flux for Validation 124

Figure 63: Naming Convention for 8x4 Sample 125

Figure 64: Example of a Sample Slightly Smaller than the In-Plane Test Device Allowing Air to Pass around the Sample Resulting in a Decreased Pressure Drop 126

Figure 65: Pore Size Distribution for an 8x8 Plain Weave 128

Figure 66: Graphical Representation of the Pores Between Interlacing Tows 129

Figure 67: High Resolution Microscope Image of (a) Macropores and (b) Micropores and Nanopores 130

Figure 68: Cumulative Pore Distribution for an 8x8 Plain Weave 131

Figure 69: Graded Reaction Rate due to Non-Uniform Catalyst Loading as Oxygen is Consumed through the Cell 137

NOMENCLATURE

Symbols

A	Area
ai_{0c}	(Specific Surface Area of Catalyst) x (Exchange Current Density)
a_{ratio}	Aspect Ratio
c	Concentration
c_{ref}	Reference Concentration
D	Diffusion Coefficient
D	Effective Diffusion Coefficient
d_f	Fiber Diameter
E	Nernst Potential
E^0	Standard Nernst Potential
F	Faraday's Constant
G	Gibbs Free Energy
G^0	Gibbs Free Energy at STP
H	Net Rate of Production/Consumption
h	Height
I	Current
i	Current Density
i_0	Exchange Current Density
j	Reaction Rate
K	Permeability
k	Diffusion Prefactor

L	Length
M	Molecular Weight
m'	Mass Flux
$\dot{m}$	Mass Flow Rate
N	Diffusive Flux Vector
Nu	Nusselt Number
n	Electrons Transferred per Reaction
P	Total Pressure
Pr	Prandtl Number
p	Partial Pressure
Q	Heating Rate
q	Mass Flux
R	Universal Gas Constant
Re	Reynolds Number
r	Resistance
S	Source Term
s	Tomadakis-Sotirchos Fitting Parameter
T	Temperature
V	Operating Voltage
$\forbar{V}$	Volume
$\forbar{V}_{p,C}$	Compressed Pore Volume
$\forbar{V}_{b,C}$	Compressed Bulk Volume
v	Velocity
w	Width
X	Mol/Weight Fraction

x	x- position

Greek Symbols

α	Charge Transfer Coefficient
β	Forchheimer Coefficient
γ	Product
δ	Thickness
ε	Porosity
ε_0	Original Porosity
ε_C	Compressed Porosity
ε_p	Tomadakis-Sotirchos Fitting Parameter
μ	Dynamic Viscosity
η	Overpotential
ρ	Density
Φ	Potential
σ	Conductivity
τ	Reactant
ψ	Diffusion Volume
ξ	Stoichiometry

Subscripts

activation	Referring to Activation Losses
avg	Average
C	Compressed
c	Cathode
CK	Carman-Kozeny
Catalyst	Catalyst Layer

concentration	Referring to Concentration Losses
e	Electronic
electode	Electrode
GDL	Gas Diffusion Layer
H_2	Hydrogen
H_2O	Water
i	Ionic
inlet	Inlet
l	Limiting (for Limiting Current)
m	Mass
membrane	Membrane
ohmic	Referring to Ohmic Losses
T	Total
O_2	Oxygen

SUMMARY

Due to escalating energy costs and limited fossil fuel resources, much attention has been given to polymer electrolyte membrane (PEM) fuel cells. Gas diffusion layers (GDLs) play a vital role in a fuel cell such as (1) water removal, (2) cooling, (3) structural backing, (4) electrical conduction and (5) transporting gases towards the active catalyst sites where the reactions take place. The power density of a PEM fuel cell in part is dependent upon how uniform the gases are distributed to the active sites. To this end, research is being conducted to understand the mechanisms that influence gas distribution across the fuel cell. Emerging PEM fuel cell designs have shown that higher power density can be achieved; however this requires significant changes to existing components, particularly the GDL. For instance, some emerging concepts require higher through-plane gas permeability than in-plane gas permeability (i.e., anisotropic resistance) which is contrary to conventional GDLs (e.g., carbon paper and carbon cloth), to obtain a uniform gas distribution across the active sites. This is the foundation on which this thesis is centered.

A numerical study is conducted in order to investigate the effect of the gas permeability profile on the expected current density in the catalyst layer. An experimental study is done to characterize the effects of the weave structure on gas permeability in woven GDLs. Numerical simulations are developed using Fluent version 6.3.26 and COMSOL Multiphysics version 3.5 to create an anisotropic resistance profile in the unconventional GDL, while maintaining similar performance to conventional GDL designs. The effects of (1) changing the permeability profile in the in-plane and through-

plane direction, (2) changing the thickness of the unconventional GDL and (3) changing the gas stoichiometry on the current density and pressure drop through the unconventional GDL are investigated. It is found that the permeability profile and thickness of the unconventional GDL have a minimal effect on the average current density and current density distribution. As a tradeoff, an unconventional GDL with a lower permeability will exhibit a higher pressure drop. Once the fuel cell has a sufficient amount of oxygen to sustain reactions, the gas stoichiometry has a minimal effect on increases in performance.

Woven GDL samples with varying tightness and weave patterns are made on a hand loom, and their in-plane and through-plane permeability are measured using in-house test equipment. The porosity of the samples is measured using mercury intrusion porosimetry. It is found that the in-plane permeability is higher than the through-plane permeability for all weave patterns tested, except for the twill weave with 8 tows/cm in the warp direction and 4 tows/cm in the weft direction, which exhibited a through-plane permeability which was 20% higher than the in-plane permeability. It is also concluded that the permeability of twill woven fabrics is higher than the permeability of plain woven fabrics, and that the percentage of macropores, ranging in size from 50-400 μm, is a driving force in determining the through-plane permeability of a woven GDL.

From these studies, it was found that the graduated permeability profile in the unconventional GDL had a minimal effect on gas flow. However, a graduated permeability may have an impact on liquid water transport. In addition, it was found that graduating the catalyst loading, thereby employing a non-uniform catalyst loading has a

greater effect on creating a uniform current density than graduating the permeability profile.

CHAPTER 1

INTRODUCTION

1.1 Energy Situation and Renewable Energy Sources

The global energy demand has reached record highs, which has lead to unprecedented cost for fossil fuel based energy resources. Escalating competition between established industrial nations and rapidly developing economies for remaining fossil fuel resources will continue to drive energy prices to record highs. In the United States (US), the highest demand for energy is along the coast-lines, (e.g., New York, Miami, Los Angeles…etc). The two primary energy resources to harvest electricity were coal and natural gas. As shown in Figure 1, nearly 70 percent of electricity generation is based on fossil fuels. It is well understood that combustion of fossil fuels pumps a tremendous amount of carbon dioxide into the atmosphere, and is arguably the greatest contributing factor to the rampant global warming of the past century. Pollution and climate change have greatly increased the attention given to renewable energy sources as a means to provide clean electrical power in the future.

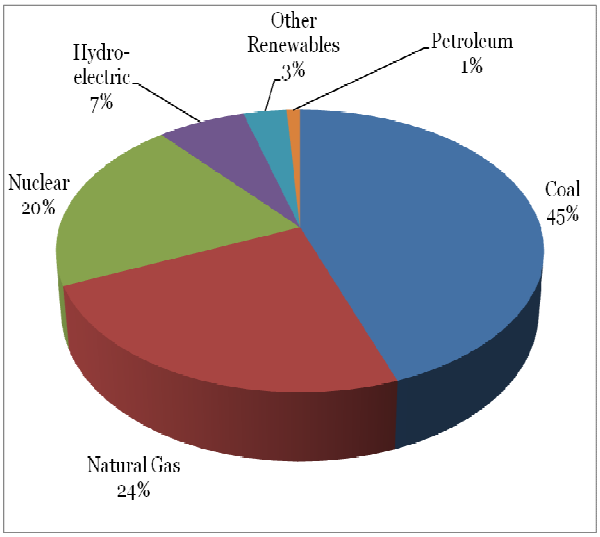

Figure 1: US Electricity Generation by Fuel, adapted from Data Given in [1]

Most renewable energy resources (e.g., solar, wind, geothermal, etc…) have a major disadvantage; they are most efficient or are only usable in locales that cater to their method of power generation. For example, most of the direct solar energy is located in the western United States in the Mojave Desert, while much of the reliable wind energy is located in the central plains and off the coasts. Further, while there is an ample supply of offshore wind near the coasts, offshore wind has been criticized because it is dangerous to navigation vessels, aesthetically unpleasing and much more expensive to build and maintain than onshore wind farms [2]. Thus, more flexible types of renewable energy resources are desired, such as fuel cells. Fuel cells offer the benefits of fossil fuels in that they can be used at any time regardless of the uncertainty of the forces of nature, and some benefits of renewable energy sources such as lower emissions. However, to become viable, many changes must be overcome.

1.2 Fuel Cells

There are six main types of fuel cells; solid oxide fuel cells, molten carbonate fuel cells, alkaline fuel cells, phosphoric acid fuel cells, direct methanol fuel cells and polymer electrolyte membrane (PEM) fuel cells. Similar to combustion engines, ideally they do not degrade over time and will run continuously if supplied with a continuous stream of reactants. In addition, a fuel cell's power capacity and fuel capacity scale independently [3]. Due to a lack of moving parts, fuel cells have the potential to provide reliable and long lasting systems, and produce significantly lower emissions of greenhouse gases than conventional burning of fossil fuels [3-4]. To this end, fuel cells have attracted significant attention due to their high efficiency, 40-50%, compared to internal combustion engines, which is limited to a range of 30-35% [5-6]. Fuel cells are electrochemical systems which directly convert chemical energy into electrical energy. However, the means by which this is achieved are different for fuel cells and combustion engines, as depicted in Figure 2. While for fuel cells, this is a direct process, the conversion for combustion engines is more cumbersome, i.e., chemical energy is converted to thermal energy which is converted into mechanical energy which is finally converted into electrical energy. Since fuel cells directly convert the chemical energy into electrical energy there are less opportunities for losses.

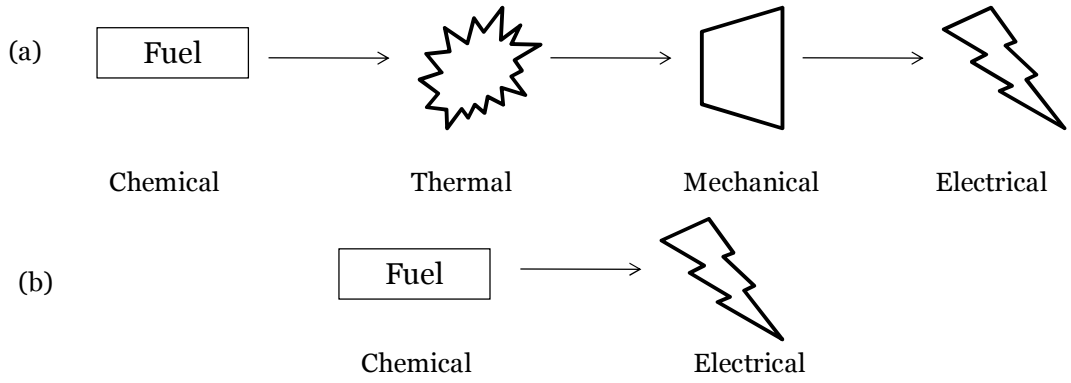

Figure 2: Energy Conversion Process for (a) Combustion Engine and (b) Fuel Cell

1.2.1 Fuel Cell Types

Solid oxide fuel cells and molten carbonate fuel cells have higher efficiencies, but are primarily used for stationary applications due to high operating temperatures (600-1000 degrees Celsius) and slow start-up times. Alkaline fuel cells have high efficiencies, for a low temperature fuel cell, but the liquid electrolyte makes it difficult to maintain for portable applications. Phosphoric acid fuel cells are low temperature fuel cells that are tolerant of impurities in fuel, but they tend to be bulky and more suitable for stationary applications. Direct methanol fuel cells are convenient because they use methanol as fuel which is readily available. Unfortunately they are subject to high losses from fuel crossover in the membrane and low power densities [3-4].

PEM fuel cells have a number of advantages over other fuel cells which make them attractive for transportation and portable applications. They operate at a relatively low temperature, 60-80 degrees Celsius, which means they ideally have quick start-up times. PEM fuel cells also have a relatively high power density compared to other types of fuel cells. In addition, the solid-state membrane is easier to design and manage in

portable systems than a liquid membrane [3-4]. Because of their advantages and application flexibility, PEM fuel cells are the focus of this thesis.

1.3 PEM Fuel Cell Components

The basic components of a PEM fuel cell are an anode, a membrane, a cathode, and bipolar plate. Specifically, a PEM fuel cell is made up of two bipolar plates, and the membrane electrode assembly (MEA), which contains the gas diffusion layers (anode and cathode), the catalyst layers, and the membrane electrolyte layer. Sealing gaskets are used in between layers to prevent gas from leaking out of the cell. The basic operating principles and components of a PEMFC are shown in Figure 3. Fuel, such as hydrogen, is oxidized at the anode releasing electrons. An electrolyte layer separates the anode and cathode which only allows ions to pass from the anode to the cathode. The electrons then travel through an external circuit and are collected at the cathode, where a reduction reaction occurs recombining the electrons with the ions. In particular, in a PEM fuel cell, hydrogen and oxygen are converted into water, electricity and heat [3-4]. Each of the previously described components has a specific responsibility which is further discussed in Sections 1.3.1 – 1.3.3.

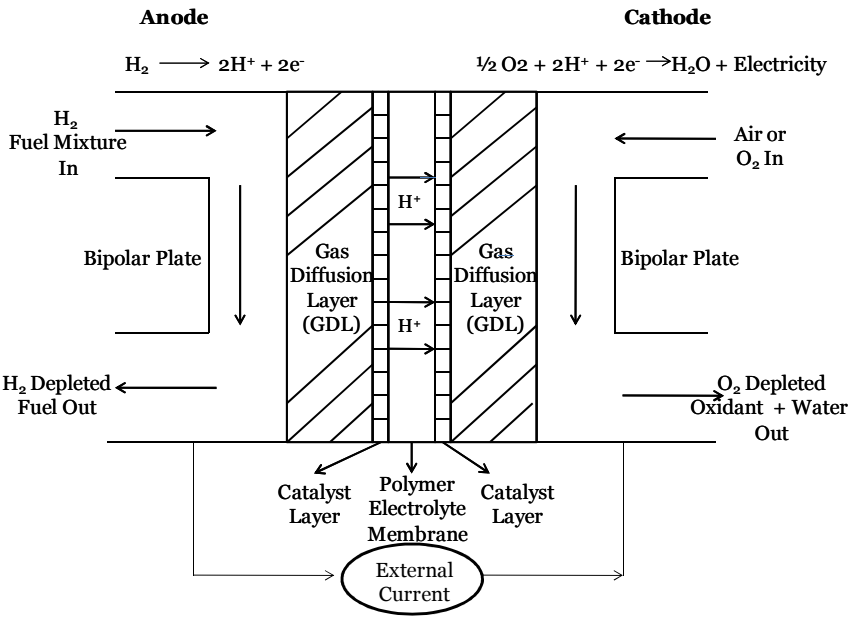

Figure 3: Schematic of a PEM Fuel Cell

1.3.1 Bipolar Plate

The bipolar plates are typically made of graphite which gives them high electrical conductivity to facilitate the transport of electrons with minimal losses, and a high thermal conductivity to remove the heat produced by the electrochemical reactions from the cell. Fuel streams are supplied through manifolds along the cell or stack. Manifolds supply fuel streams (hydrogen to the anode and either oxygen or air to the cathode) via flow channels which are typically machined into the bipolar plates. There are three major types of flow channel designs, known as flow fields (parallel, serpentine and interdigitated), which are shown in Figure 4. Each flow field design has its own pros and cons.

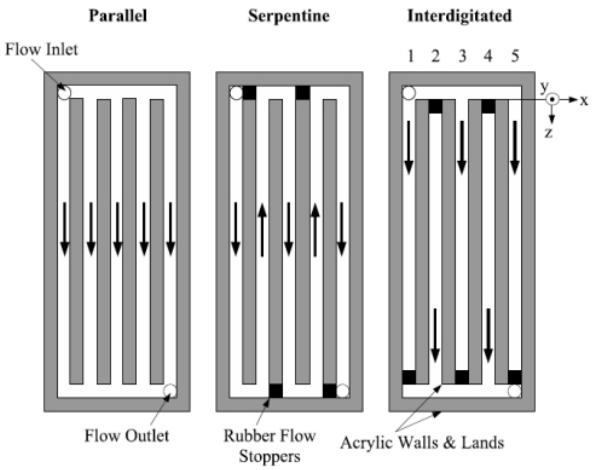

Figure 4: Flow Field Designs [7]

Parallel flow field designs allow many paths from the flow inlet to the flow outlet. However, if a water droplet blocks a channel, there may not be enough pressure to push the droplet through which will cut off flow to the affected part of the fuel cell. Serpentine designs are popular because if a water droplet is stuck in a channel, the pressure buildup will push the droplet out. However, these serpentine flow fields are known to experience high pressure drops and require more pumping power. These flow fields also suffer from poor reactant uniformity as there is only one path for the gas to travel. In interdigitated flow fields, the gas is forced into the GDL through convection rather than just diffusing to the catalyst due to concentration gradients. While interdigitated flow fields require more pumping power, they can push water out more effectively at higher current densities and show better performance over other flow field designs. It is important to achieve a uniform reactant distribution over the face of the cell so regions of the cell far from the inlet are not starved for reactants. This can create gradients in temperature and cause poor performance. To this end, research has been conducted regarding the design of flow fields achieve uniform reactant distribution in the catalyst layer [3-4, 8-14], such that areas of the electrode near the inlet are not oversaturated with fuel while areas near

the outlet are starved for fuel. Oversaturation can lead to increased water production which blocks pores, while reactant starvation can lead to structural integrity issues due to heat generation from a lack of water in the membrane [15].

1.3.2 Gas Diffusion Layer

The gas diffusion layer (GDL) is a porous structure either made by pressing carbon fibers into a carbon paper or by weaving carbon fibers into a carbon cloth. The GDL must be porous to allow the reactants in the channels of the bipolar plate to diffuse to the active sites at the catalyst layer. The GDL also provides a mechanical backing for the MEA, assists in heat and water removal from the cell, protects the catalyst layer from corrosion and erosion from flow, and must be electrically conductive to reduce ohmic losses in electron conduction [16-18].

1.3.3 Catalyst Layer

The catalyst layer is a mixture of carbon powder and platinum particles, which facilitate the electrochemical reactions. The 2-3 nm platinum particles are spread onto the surface of the larger carbon powder particles to maximize the effective area of the platinum, which is expensive and adds substantially to the cost of the cell. The catalyst mixture is then sprayed onto the GDL, or a catalyst paste is painted onto the GDL [17].

1.3.4 Membrane

The polymer electrolyte membrane is responsible for transporting the H^+ ions from the anode to the cathode, while preventing electrons from crossing the membrane and short circuiting the cell. There are two major classes of membrane, low temperature perfluoro sulfonic acid (PFSA) membranes and high temperature phosphoric acid doped

polybenzamidazole (PA/PBI) membranes. PFSA membranes consist of a backbone of a typical carbon-hydrogen polymer structure with fluorine replacing the hydrogen. During fuel cell operation, the H^+ ions travel from the anode to the cathode jumping across sulfonic acid side groups that protrude from the carbon-fluorine chain. The hydrophilic sulfonic acid side groups allow the H^+ ions to drag water molecules through the membrane, making the structure highly sensitive to drying out which drastically reduces performance. This drying of the membrane limits the operating temperature of these fuel cells to less than 100°C, hence the low temperature classification. Emerging membranes that are not sensitive to water content, such as PA/PBI membranes, allow the temperature of the fuel cell to increase above 100°C (hence the high temperature classification) to operate at higher efficiencies while eliminating the complexity of water management in the fuel cell [3-4].

1.4 Limitations to Growth

In order for PEM fuel cells to gain a foothold in the market, they must overcome several hurdles such as high cost, low power densities and poor water management. Cost is the most inhibiting factor and is caused by a number of factors, namely the platinum catalyst and bipolar plate. The high cost of platinum has historically been a major contributing factor to the total cost of the fuel cell. Recent advancements have reduced the amount of platinum loading by a factor of 10 from 4 mg/cm^2 to 0.4 mg/cm^2, which has significantly reduced the cost contribution to the cell [17]. Another major cost contributor is the bipolar plate. The machining of the flow channels is so expensive that the graphite bipolar plates can comprise half of the cost of the fuel cell [3, 19].

An additional limitation is low power density, which is especially important in transport applications. PEM fuel cells have a higher power density than most other fuel cells, but the power density needs to improve further to compete with internal combustion engines, which is currently around 1000 kW/m^3 [4]. Bipolar plates are by far the largest component of the fuel cell assembly and can take up to 80% of the volume and mass of the cell [19-20]. Because power is increased by stacking cells, this issue can quickly lead to heavy, bulky units which are not ideal for transportation or portable applications, also negatively affecting performance. If the size of a single cell could be reduced without affecting performance, more cells could be stacked in the same volume, which would drastically increase the power density.

Water management is another challenging issue at the cell level. On one hand, the membrane must be hydrated to allow the protons to jump sulfonic acid sites in the membrane. A lack of water in the membrane will decrease ionic conductivity and cell performance. On the other hand, too much water will flood the pores in the cathode GDL and prevent reactants from reaching the platinum sites where the reaction takes place. This balance between flooding and drying out is difficult to achieve and is a major consideration in design [21].

1.5 Motivation for this Work

As discussed in Section 1.4, reducing the size of the bipolar plate will significantly decrease the size of the PEM fuel cell. Or, the PEM fuel cell will produce more power per unit volume, hence increasing the power density. Bhamidipati et al. presented an unconventional PEM fuel cell stack design, shown in Figure 5 (a), which theoretically increases the power density of a PEM fuel cell stack while simultaneously

decreasing size, volume, mass and cost by replacing the bipolar plate with a flat metal sheet [22]. A fuel cell stack is a collection of individual fuel cells compressed together to obtain a certain power density. An example of a traditional PEM fuel cell stack is shown in Figure 5 (b), which exhibits internal manifolding.

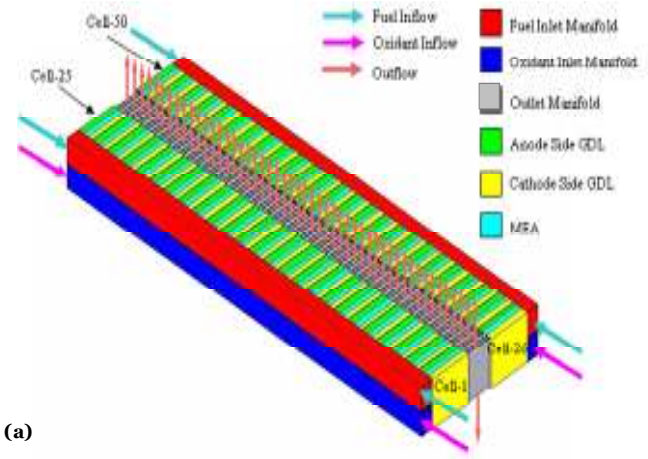

(a)

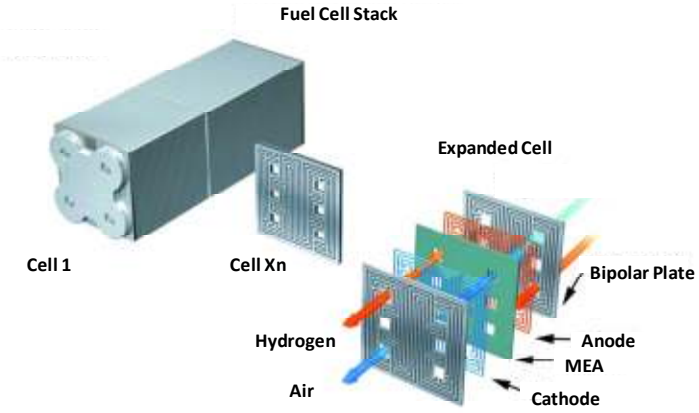

(b)

Figure 5: (a) Stack Design by Bhamidipati et al. [22] (b) Traditional Stack with Internal Manifolding, adapted from [23]

In the unconventional PEM fuel cell stack design, the cells are arranged in two columns to increase the number of cells in the stack, thereby increasing power density for a similar stack size comparing to a conventional fuel cell stack. Within a column, the

cells are arranged in the conventional manner with the cathode of one cell adjacent to the anode of the next cell. The thin conductive metal sheet acts as a separator and thermal conductor and decreases the size and weight of the cell. No additional machining is required for the metal sheet which significantly reduces the manufacturing cost for the bipolar plate. For the unconventional PEM fuel cell, the GDLs take over the role of delivering reactants to the active catalyst sites, traditionally performed by the bipolar plates, as shown in Figure 6.

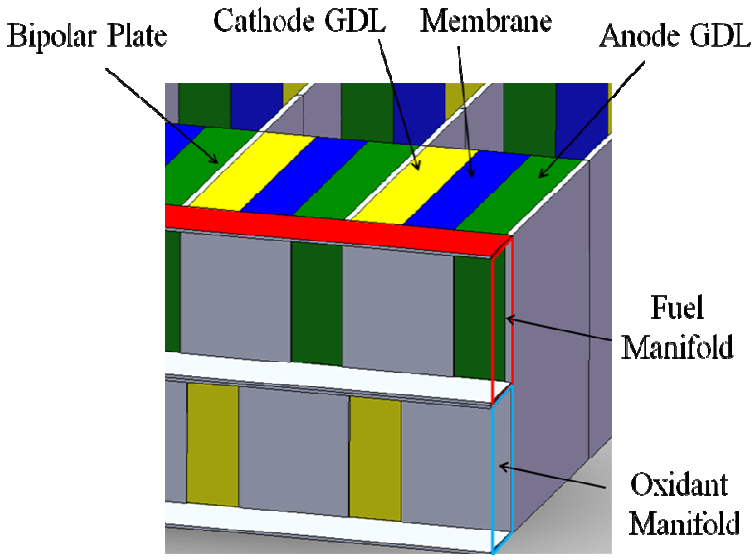

Figure 6: Close-up of Manifolds and GDLS in New Stack Design

The fuel manifolds and oxidant manifolds are placed along the length of the stack external to the cells (i.e., external manifold). To provide fuel and oxidant to the active catalyst sites, the internal wall of the manifolds are designed such that only ½ of every other GDL in the longitudinal direction is exposed. The preliminary study conducted by Bhamidipati et al. compared traditional stack designs having a Z or U shape to the unconventional design. The power densities they found for the three stack configurations are shown in Table 1.

Table 1: Comparison of Power Density from Different Fuel Cell Stack Designs [22]

	U Design	Z Design	Unconventional Design
Power Density (kW/m^3)	274.36	274.45	1065.76

It was found that the unconventional stack design has a power density almost 4 times higher than traditional stack designs. Since they were able to decrease the size of the stack by decreasing the size of the conducting plate, they could stack 4 times as many cells in a given volume giving the stack the ability to produce 4 times as much power.

In order to realize the potential benefits of the unconventional fuel cell stack, it is necessary to (1) develop a GDL that can accommodate the fuel and oxidant distribution requirements, (2) understand water management and thermal management issues, and (3) understand the transport phenomena involved in the porous GDL. This thesis will address one aspect of these issues; developing a GDL to accommodate the gas distribution into a cell. Since the reactants enter the GDL through the side, it is necessary to design a GDL with a graduated permeability and therefore a graduated resistance to flow to obtain uniform reactant distribution. This graduated GDL will have an anisotropic permeability profile with a different permeability in the in-plane and through-plane direction. The through-plane direction is perpendicular to the electrode face, while the in-plane direction is across the face of the GDL. The objective of this work is to characterize a permeability profile for this graduated resistance, using experimental and numerical approaches.

1.6 Structure of the Thesis

This thesis is split up into six main parts. The first part is a literature review, followed by two numerical studies, experimental work, conclusions and suggestions for future work. The beginning of Chapter 2, the literature review, focuses on existing fuel cell models and numerical studies where the authors investigate graduated porosity. After that, papers are studied where the investigators test the permeability of common gas diffusion layers to understand pearmeability testing methodology and to obtain reference data. The last part of the literature review covers papers which discuss the permeability of woven fabrics.

In Chapter 3, the first numerical study, the cathode of a fuel cell is modeled with commercial computational fluid dynamics (CFD) software Fluent Version 6.3.26, and the effect of permeability on expected current density is investigated. Average current densities are compared to standard deviation of the current density to investigate uniformity. While the study takes into account the equations for gas flow, the current density is not coupled to the mass concentrations of oxygen, and the equations for potential are not solved. Thus, a more robust numerical model and solver was needed.

In Chapter 4, the second numerical study, a fuel cell cathode is modeled with another commercial CFD software, COMSOL Mulitphysics version 3.5. In this model, permeability profiles are looked at in more detail throughout the GDL, and the current equations are coupled to the mass concentrations. This more complex model also takes into account the charge transport equations.

In Chapter 5, the experimental section, the design of experiments and the methodology for the design of the permeability testing device are discussed. Following

this, the results from the tests of permeability profiles are presented. Samples were also sent to Micromeritics to test the porosity and analyze pore structure. The pore analysis is used to explain experimental data.

In Chapter 6, conclusions from the preceding 3 chapters are summarized. In Chapter 7, suggestions for future work are discussed. A preliminary study into graduating the catalyst loading is conducted in order to achieve a more uniform current density distribution.

CHAPTER 2

LITERATURE REVIEW

2.1 Introduction

In this thesis, numerical studies are run to simulate the effect of changing the gas diffusion layer permeability and study the effect on performance. Also, experiments are conducted in which GDLs are woven from carbon fibers with varying weave pattern and tightness to measure the permeability. In this chapter, a review on the equations which describe fuel cell performance and fuel cell modeling approaches and are discussed. Following this, a literature review is presented on permeability modeling, experimental methods to test gas permeability in GDLs, and permeability of woven structures.

2.2 Fuel Cell Performance

Before fuel cell modeling is discussed, it is important to understand the basics of how a fuel cell's performance is judged. Thus, a basic overview on how a fuel cell's voltage is calculated and what contributes to losses in voltage and efficiency is given in Section 2.2, followed by a detailed description on various modeling approaches used to characterize not only PEM fuel cells, but also a porous media.

2.2.1 Nernst Potential

When a fuel cell draws no current, the cell voltage is at the reversible Nernst Potential, E, which is the maximum potential the cell can obtain before any of the irreversible losses take effect. This voltage takes into account the work potential of the

fuel, the temperature, pressure and the electrochemical reaction. The Gibbs Free Energy, *G*, is the energy required to create an electrochemical system, minus the energy contributed by the environment through spontaneous heat transfer. Since *G* encompasses all the energy used to create the electrochemical system, it is the theoretical maximum energy the system can provide [3]. For a hydrogen-oxygen fuel cell at standard temperature and pressure (STP) conditions, 25°C and 1 atmosphere respectively, the standard Nernst potential, E^0, is given by Equation 1 [3-4],

$$E^0 = -\frac{\Delta G^0}{nF} \tag{2.1}$$

where ΔG^0 is the change in Gibbs Free Energy at STP, *n* is the number of electrons transferred per reaction and *F* is Faraday's constant [3-4]. Therefore, E^0 is 1.23 V.

Most fuel cells do not run at standard conditions, these changes in temperature and pressure affect the Nernst Potential. For a fuel cell operating below 100°C, the corrected Nernst Potential is shown in Equation 2.2 [3].

$$E = E^0 - \frac{RT}{2F}\ln\left(\frac{1}{p_{H_2} p_{O_2}^{1/2}}\right) \tag{2.2}$$

where *E* is the corrected Nernst Potential, *R* is the universal gas constant, *T* is the temperature in Kelvin, p_{H_2} is the partial pressure of hydrogen in the fuel mixture, and p_{O_2} is the partial pressure of oxygen in the oxidant mixture.

2.2.2 The Polarization Curve and Irreversibilities

The metric used to measure fuel cell performance is the polarization curve. The polarization curve is a plot showing the drop in voltage as the average current density (the amount of current drawn through the cell) increases. A typical polarization curve is shown in Figure 7.

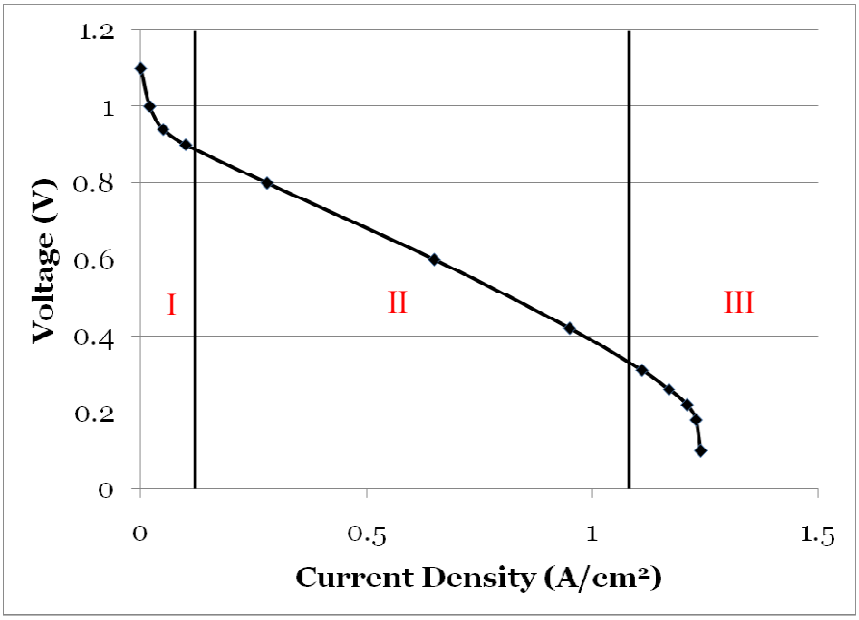

Figure 7: Polarization Curve adapted from [24]

As shown in Figure 7, the polarization curve is grouped into three regions. Region I is the activation loss region. Activation losses are described by the Butler-Volmer Equation[3], given by,

$$i = i_0 \left(\frac{c_\tau}{c_{\tau_0}} \exp^{\frac{\alpha n F \eta}{RT}} - \frac{c_\gamma}{c_{\gamma_0}} \exp^{\frac{-\alpha n F \eta}{RT}} \right) \tag{2.3}$$

where i is the current density, i_0 is the exchange current density, c_τ is the concentration of the reactant, c_{τ_0} is the reference concentration of the reactant, c_γ and c_{γ_0} are the

concentration and reference concentration of the product, α is the charge transfer coefficient and η is the activation voltage drop or voltage loss. Therefore, this relationship tells us there is an exponential relationship between an increase in current and the drop in voltage. This explains the exponential shape of the activation region. The kinetics of the hydrogen-oxidation reaction at the anode are much faster than the kinetics of the oxygen-reduction reaction at the cathode. This causes the activation voltage losses from the cathode reaction to be dominant over the losses from the anode reaction.

Region II is the ohmic region. These losses are due to electronic charge transfer resistance throughout the GDL, catalyst layer, and bipolar plate and ionic charge transfer resistance through the membrane. The ohmic losses, η_{ohmic}, are given by Equation 2.4 [25].

$$\eta_{ohmic} = ir_{ohmic} = i\left(r_{electronic} + r_{ionic}\right) \tag{2.4}$$

where r_{ohmic} is the ohmic resistance. The resistance can be split up into an electronic and ionic component. Since the GDL, catalyst layer, and bipolar plates are made of a combination of metal, graphite or carbon fibers, the electronic resistance is low due to the high electrical conductivity of these materials. Therefore, the ionic resistance dominates the ohmic resistance [3-4].

Region III is the concentration loss or mass transport loss region. As the fuel is depleted while travelling throughout the cell, there will be a reduction in the partial pressure of the hydrogen and oxygen. Also, as the current density is increased, more fuel must be supplied to sustain a higher reaction rate. At a certain point, all the catalyst sites

will be depleted and the current density can no longer increase. This is a compound effect of an inability to increase the current density with a decrease in voltage caused by the drop in partial pressure. This manifests itself as a concentration loss which can be estimated by Equation 2.5 [25].

$$\eta_{concentraiton} = \frac{RT}{2F}\ln\left(1-\frac{i}{i_l}\right) \tag{2.5}$$

where $\eta_{concentration}$ is the concentration overpotential, i_l is the limiting current density, or the current density at which the concentration losses become dominant. The limiting current density is a somewhat arbitrarily chosen number that will depend on operating conditions and the fuel cell's materials and geometry. The limiting current is better used as a curve fitting parameter than an actual modeling parameter [3-4].

2.3 Fuel Cell Modeling Methodology

In general, fuel cell models can be characterized by their physical dimension and their level of complexity. In the following section different levels of modeling complexity will be discussed to see the advantages and disadvantages of upgrading models.

2.3.1 Zero Dimensional Models

The simplest models are zero-dimensional models, which describe the polarization with a single equation. The voltage can be found at a range of current densities by subtracting the three types of losses from the Nernst Potential [25],

$$V = E - \eta_{activation} - \eta_{ohmic} - \eta_{concentration} \tag{2.6}$$

where V is the operating voltage of the cell. Zero dimensional models are best suited for fitting to empirical data rather than intensive modeling. They can be helpful to learn which type of loss is dominant with a set of operating parameters, but they are not useful for optimizing fuel cell performance [25].

2.3.2 One Dimensional Sandwich Models

In 1-D sandwich models, the individual layers of the cell are modeled, but transport is only solved in one direction, the direction perpendicular to the cell faces (the through-plane direction) as opposed to the in-plane direction which is the direction parallel to the cell faces, as seen in Figure 8.

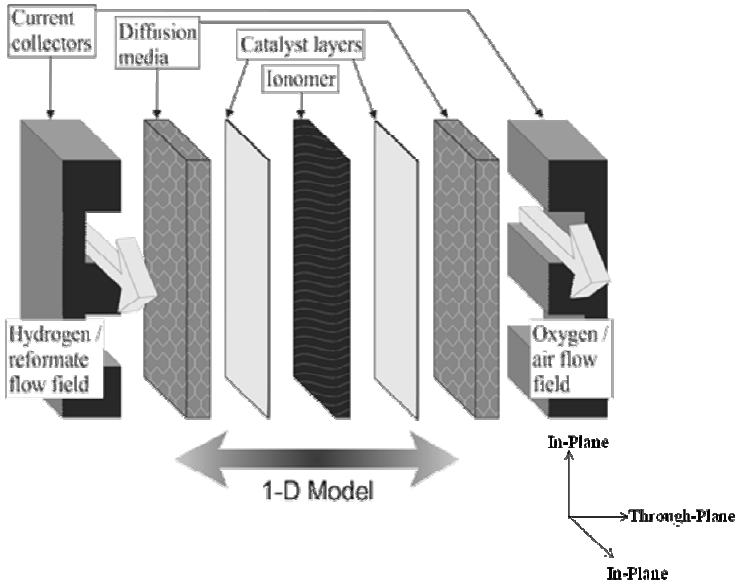

Figure 8: Typical One Dimensional Sandwich Model adapted from [25]

Material properties that affect transport such as electrical conductivity and air permeability can be set as 1-D space dependent variables through the layers, while boundary conditions for the transport processes that occur between layers can be used to couple transport properties across adjacent layers. While the complexity of the mass

transport is reduced, 1-D models allow investigation of other transport phenomena, which may be difficult to model in multiple spatial dimensions, at a lower computational cost. 1-D models are desirable when transport is considered isotropic, and the mass or charge distributions throughout the cell are unimportant [25].

2.3.3 Two Dimensional Flow Models

To model effects that can only be seen in multiple dimensions such as velocity fields, charge distribution and mass concentration profiles, a 2-D model can be used. There are two configurations of 2-D models shown in Figure 9 (a) and (b). Figure 9 (a) is an along-the-channel model. The inlet and outlet ports of the gas channel are modeled as part of the fuel cell sandwich. In this way, gas consumption and charge distribution can are analyzed along the length of the cell as the hydrogen is consumed. A limitation of this approach is that only one channel can be analyzed at a time, and the effects of flow through multiple channels in the plate cannot be visualized. Also flow under-the-ribs between the channels cannot be analyzed. To investigate flow into the GDL, one could use an under-the-rib model shown in Figure 9 (b), which represents the gas flow into the gas diffusion layer and under the section of the bipolar plate between two adjacent channels, called the rib. A limitation of this approach is that the flow cannot be analyzed as gas is used up along the channel.

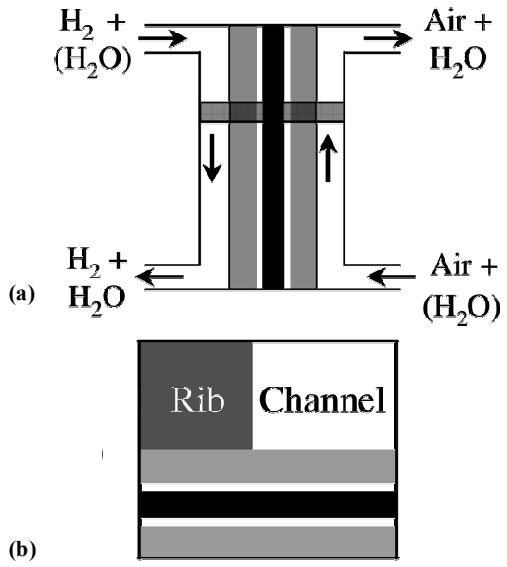

Figure 9: (Along the Channel Model and (b) Under-the-Rib Model [6]

2.3.4 Three Dimensional Flow Models

In 3-D models, it is common to extend the under-the-rib model, illustrated in 9 (b), along the rest of the channel forming a 3-D pattern, as shown in Figure 10. Using this method, gas consumption can be analyzed along the length of the channel and over the face of the cell at cross-sections in the channel. Unfortunately, modeling transport in three dimensions is computationally costly, and 3-D models usually focus on intensive modeling of one transport process. To cut down on computational costs, it is common to model one channel rather than an entire cell, as all the channels are symmetrical and should show similar velocity and concentration profiles [25].

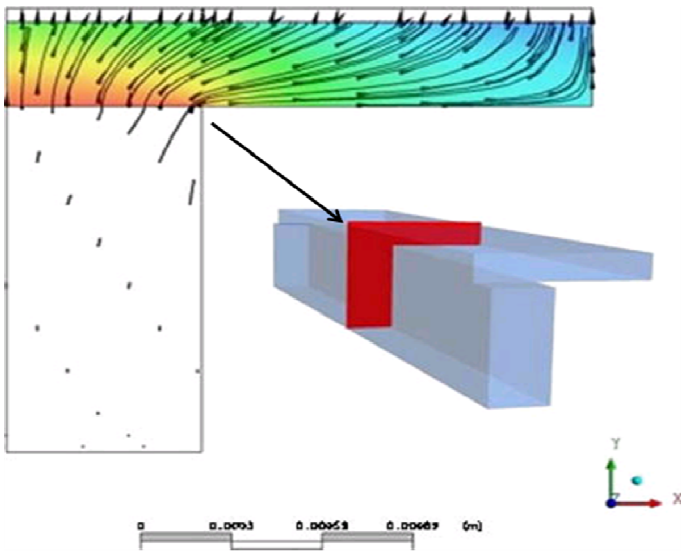

Figure 10: Three Dimensional Under-the-Rib Model Showing Velocity Profile and Mass Fractions of Oxygen at a Cross-Section in a Channel adapted from [26]

2.4 Diffusion Media Modeling

There are two primary transport mechanisms in the gas diffusion layer, diffusive transport and convective transport. Diffusive transport occurs naturally due to concentration gradients as reactants are consumed or produced. Reactant gases are consumed at the catalyst layer which creates a concentration gradient for hydrogen in the anode and oxygen in the cathode. As a result, fuel rich gas will flow towards the catalyst layer based on the rate of consumption. Convective transport occurs when a pressure gradient forces a fluid to flow towards a region of lower pressure. In interdigitated flow fields, the gas in an inlet channel must flow through the GDL to reach the lower pressure at the outlet. The pressure builds up in the inlet channel and forces the gas through the GDL to the outlet channel.

The Maxwell-Stefan Equation for diffusion, Equation 2.7, is often used to describe the diffusive flux in the fuel cell [25].

$$\nabla X_i = \sum_{j \neq i} \frac{X_i N_j - X_j N_i}{c_T D_{i,j}^{eff}} \tag{2.7}$$

where X is the mol fraction of species i, N is the diffusive flux vector for species i and j, c_T is the total concentration of the mixture, and $D_{i,j}^{eff}$ is effective diffusion coefficient. The diffusion coefficient in the porous media (i.e. the GDL) will be lower than diffusion in a non-porous media (i.e. the open flow channels) due to interaction with the pore walls. The decrease in the diffusion coefficient is modeled with the Bruggeman expression shown in Equation 2.8 [25, 27-31], which relates the bulk porosity, ε, and the binary diffusion coefficient, $D_{i,j}$, between two species to the effective diffusion coefficient.

$$D_{i,j}^{eff} = \varepsilon_o^{1.5} D_{i,j} \tag{2.8}$$

where the diffusion coefficient can be found from a formulation in Kinetic Gas Theory [32-33], given by Equation 2.9.

$$D_{i,j} = k \frac{T^{1.75} \times 10^{-3}}{P\left[\left(\sum_k \psi_i\right)^{1/3} + \left(\sum_k \psi_j\right)^{1/3}\right]^2} \left[\frac{1}{M_i} + \frac{1}{M_j}\right]^{1/2} \tag{2.9}$$

where k is a diffusion prefactor, P is the total pressure, ψ is the diffusion volume of species i or j, and M is the molecular weight of species i or j.

In fuel cells with parallel and serpentine flow fields the gas is not forced by a pressure gradient into the GDL. Therefore, diffusion is the dominant transport mechanism, and these types of fuel cells are often modeled only considering diffusion. In interdigitated flow fields, the operating principle is based on forced convection into the

GDL. To capture pressure losses throughout the GDL due to convection, the Darcy-Forchheimer equation is added to models, given by Equation 2.10 [34],

$$-\nabla P = \frac{\mu}{K} v + \beta \rho v^2 \tag{2.10}$$

where μ is the viscosity of the gas, K is the permeability, v is the velocity, and β is the Forchheimer coefficient. The Forchheimer term, $\beta \rho v^2$, is valid at higher flow velocities. At low flow velocities where the Reynolds number is smaller than 1, the Darcy-Forcheimmer Law reduces to Darcy's Law and is given by Equation 2.11 [3].

$$\nabla P = -\frac{\mu}{K} v \tag{2.11}$$

Darcy's law is added as a source term in the momentum equation. It can be seen that the value of the permeability in the denominator will significantly affect the velocity and the pressure drop through the GDL. The viscosity will remain nearly constant at a constant temperature, which makes the permeability the dominant parameter affecting the velocity of the gas. If the permeability is decreased by a factor of 10, the velocity will decrease by a factor of 10 for a given pressure drop. It is important to note that this equation is valid for gas phase flow only. If two-phase flow were considered, the relative permeability of both the liquid and gas phase would need to be addressed in the equation. As discussed at the beginning of this section, convective porous media treatment is important in interdigitated flow fields. In the unconventional design considered in this thesis, the gas travels due to an in-plane pressure gradient via forced convection through

the GDL; while diffusion is still considered, convection is the dominant transport mechanism.

2.5 Models with Varying Porosity and Permeability

Most models presented in literature treat the GDL with isotropic permeability [28-32, 35-40]. A few models consider the GDL to have an anisotropic permeability profile [41-42], while some other models attempt to create graded porosity models to represent different phenomena such as GDL compression and liquid water formation blocking the pores [43-44].

In the unconventional stack design, it has been hypothesized that the permeability in the gas diffusion layer will need to be controlled. To control the gas permeability, the porosity in the gas diffusion layer has to be designed such that desired gas permeability profile is created. Gas permeability is often related to the porosity using the Carman-Kozeny equation [45],

$$K = \frac{d_f^2 \varepsilon^3}{16 k_{CK} (1-\varepsilon)^2} \tag{2.12}$$

where d_f is the fiber diameter. The Carman-Kozeny model does not differentiate between isotropic and anisotropic permeability and is reliant on a fitting parameter, k_{CK}, which is different for all materials and fiber arrangements. Tomadakis and Sotirchos developed an equation to predict the anisotropic permeability of 1-D, 2-D and 3-D random fiber beds [46-48], which only relies on the average porosity and fiber diameter and is given by,

$$K = \frac{\varepsilon}{8\left(\ln \varepsilon^2\right)} \frac{\left(\varepsilon - \varepsilon_p\right)^{(s+2)} d_f^2}{\left(1-\varepsilon_p\right)^s \left[(s+1)\varepsilon - \varepsilon_p\right]^2} \tag{2.13}$$

where ε_p and s are fitting parameters depending on the geometry of the fibrous structure. For a 2-D random alignment of fibers, which is analogous to the carbon fiber structure in a conventional carbon paper GDL, ε_p is set to 0.11 while s is set to 0.521 in the in-plane direction and 0.785 in the through-plane direction.

2.5.1 Porosity Gradient Models

Chen et al. employ a 1-D, two-phase model with a porosity gradient in the GDL to simulate the addition of a microporous layer (MPL) [43]. An MPL is a layer between the GDL and the catalyst, which is infused with a hydrophobic material such as PTFE and is used to effectively push water away from the membrane and out of the GDL. The MPL has smaller pores than the GDL but bigger pores than the catalyst layer, which helps reduce the contact resistance between the GDL and catalyst. The configuration is shown in Figure 11.

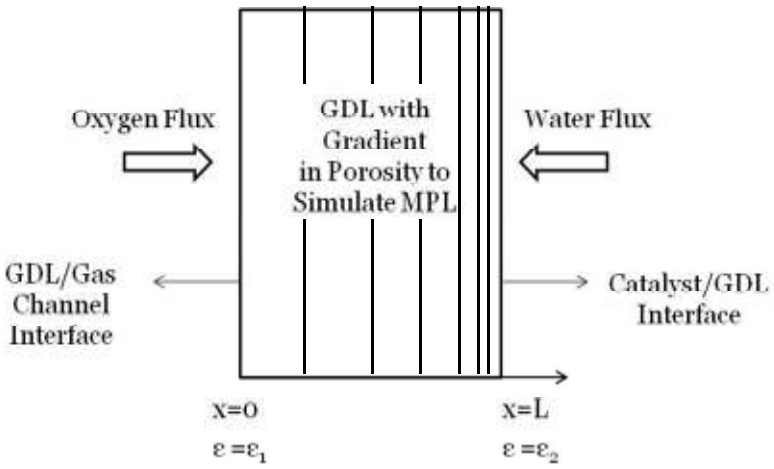

Figure 11: Simulation Configuration for Chen et al. adapted from [43]

The porosity decreases linearly from an initial value of ε_1 to a final value of ε_2 based on the following equation developed by Chen et al.,

$$\varepsilon(x) = \varepsilon_1 + (\varepsilon_1 - \varepsilon_2)\frac{x}{L}. \tag{2.14}$$

The porosity at the catalyst layer/GDL interface is set to 0.2, and the porosity at the gas channel/GDL interface is increased over a range of 0.2 to 0.8. Polarization curves for different values of gas channel/GDL interface porosity are shown in Figure 12.

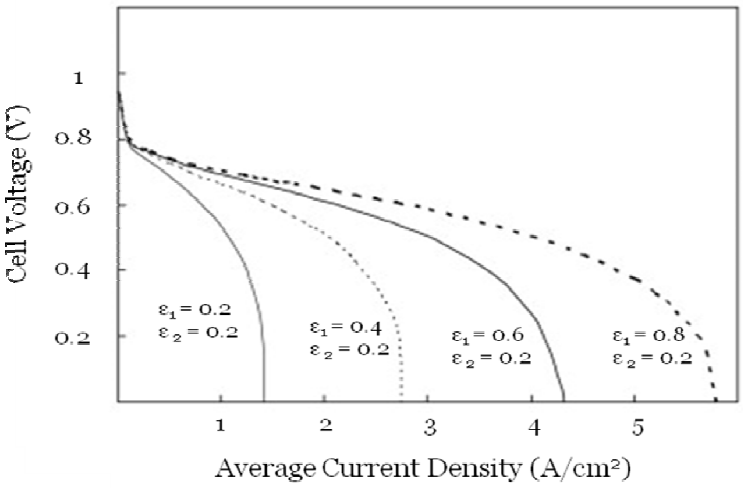

Figure 12: Polarization Curve for Different Values of ε_1 adapted from [43]

It was shown that a greater porosity gradient enhances the removal of liquid water, freeing up pores in the GDL and improving oxygen transport, which in turn increases the limiting current density and performance of the cell significantly [43].

Chu et al. developed a 1-D model to try to model liquid water saturation as a gradient in porosity [44]. They ran four simulations with four different porosity gradients through the GDL. In model 1 the porosity was constant at 0.4. In model 2, there was a linear decrease in porosity. In models 3 and 4, they used a concave and convex exponential function to model porosity as a function of position. The porosity gradients used by Chu et al. are shown in Figure 13. The effect of the porosity change on the

polarization curve is shown in Figure 14. A zero dimensional equation was used to generate the polarization curve, which has limitations as discussed in Section 2.2.1.

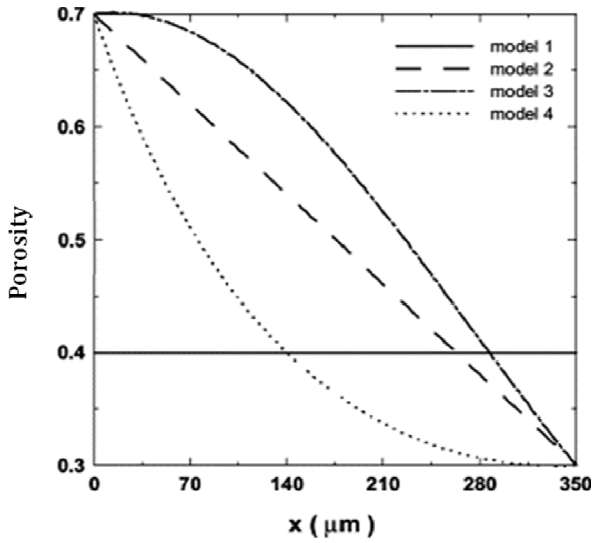

Figure 13: Porosity Distribution as Function of Position for 4 Models adapted from [44]

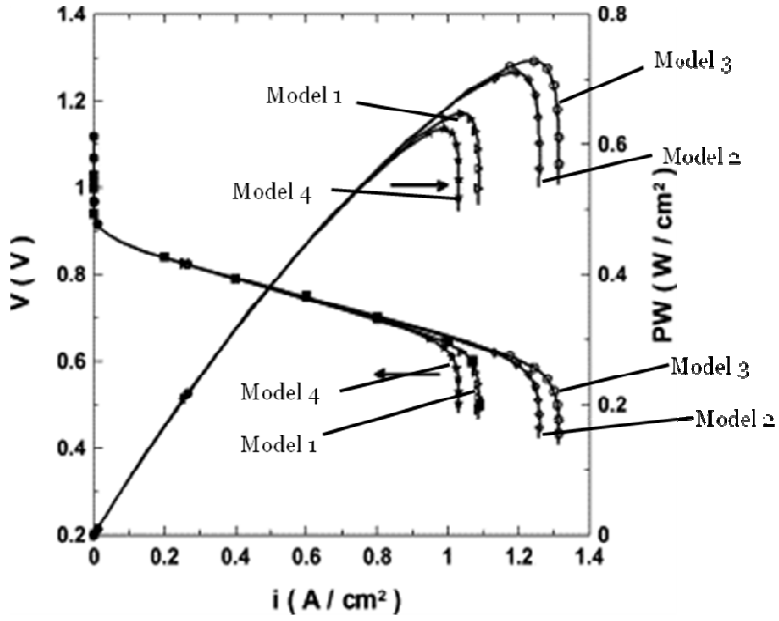

Figure 14: Effect of Porosity Change Model on Polarization Curve adapted from [44]

Model 3 represents the model with the convex exponential shape and the highest porosity. It was shown by Chu et al. that models with higher porosity lead to higher

water transport out of the cell and higher oxygen transport into the catalyst [44]. This leads to higher operating voltages and power densities. The rest of the models showed similar trends; models with higher porosity performed better.

2.5.2 Compressed GDL Models

Nitta et al. investigated the effect of inhomogeneous compression in the GDL on the transport properties using a 2-D single-phase flow model [49]. During operation, the cell is compressed by the endplates to help with sealing. Under compression, the sections of the GDL under the bipolar plate ribs are compressed while the sections of GDL under the open channels are uncompressed, as seen in Figure 15 (a) and (b). Under compression, the pores in the GDL will decrease and the transport of oxygen from the gas channel to the catalyst layer will be restricted.

In the model, the porosity of a compressed sample is related to the level of compression by Equation 2.15, given by,

$$\varepsilon_c = 1 - (1 - \varepsilon_0)\frac{h_0}{h(x)} \tag{2.15}$$

where ε_c is the compressed porosity, ε_0 is the original porosity, h_0 is the original thickness and $h(x)$ is the thickness as a function of the x- position, which changes based on the amount of compression. The compressed thickness is plotted against the compressed porosity, and the compressed permeability is calculated from an equation developed from a curve fit. While the gas permeability changes as a function of x-, the permeability is still considered isotropic.

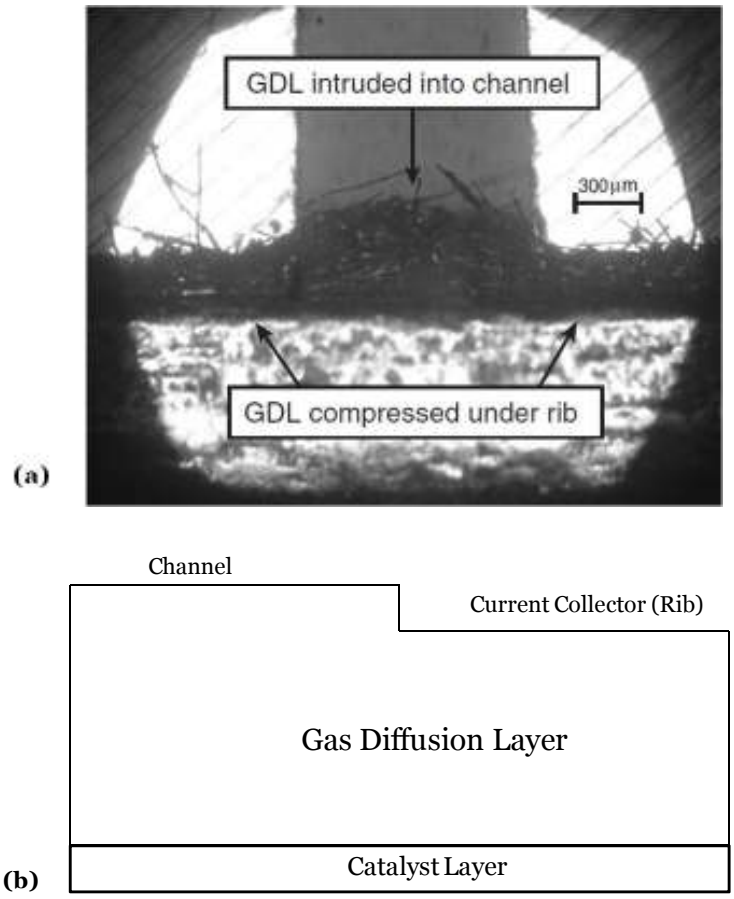

Figure 15: (a) Photograph of GDL under Compression [49] and (b) Model of GDL Under Compression adapted from [27]

The oxygen molar fraction at the catalyst layer/GDL interface for both a model that considers a change in permeability due to compression and a model that does not consider compression in the transport properties were studied by Nitta et al. and are shown in Figure 16. They found that there exists no significant change in oxygen molar fraction between the compressed GDL and the uncompressed GDL. They concluded that the decrease in permeability under the rib due to compression did not cause a change in the mass distribution of oxygen at the catalyst layer.

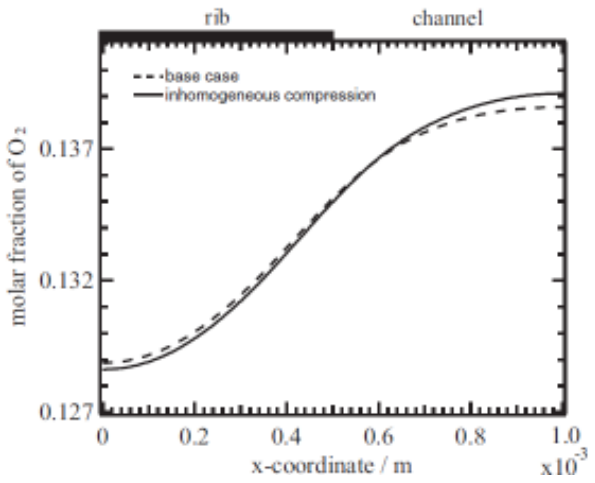

Figure 16: Oxygen Molar Fraction at GDL/Catalyst Layer Interface at a Cell Voltage of 0.5 V [49]

Sun et al. created a 2-D under-the-rib model to investigate the current density distribution under different levels of compression [27]. The area underneath the rib is assumed to be 15% thinner than the area under the channel. A compressed GDL was compared to an uncompressed GDL. They found that the total average current density in the uncompressed GDL was 640 mA/cm^2, while the average current density in the compressed GDL was 632 mA/cm^2, which is an insignificant difference. Sun et al. showed that when the GDL is compressed, mass distribution of oxygen is impeded by smaller pores, but electrical conductivity increases. In this model the effects seem to cancel out each other [27]. This illustrates an important trade-off between pore size and conductivity. Increasing pore size will help increase mass distribution, but it will also increase contact resistance between the carbon fibers which reduces electrical conductivity.

2.5.3 Anisotropic Permeability Modeling

Pharoah developed a 3-D model with a serpentine flow field to study the effect of isotropic and anisotropic permeability profiles on convective flow between channels in

the GDL [42]. It is discussed that GDLs are either made by pressing chopped carbon fibers together into a paper, or weaving bundles of carbon fibers together into a cloth, which creates a different structure in the in-plane and through-plane. This would imply that the flow characteristics should be different in the in-plane and through-plane directions. The pressure drop in the channel when comparing an isotropic model to two orthotropic models, based on Pharoah's work, can be seen in Figure 17.

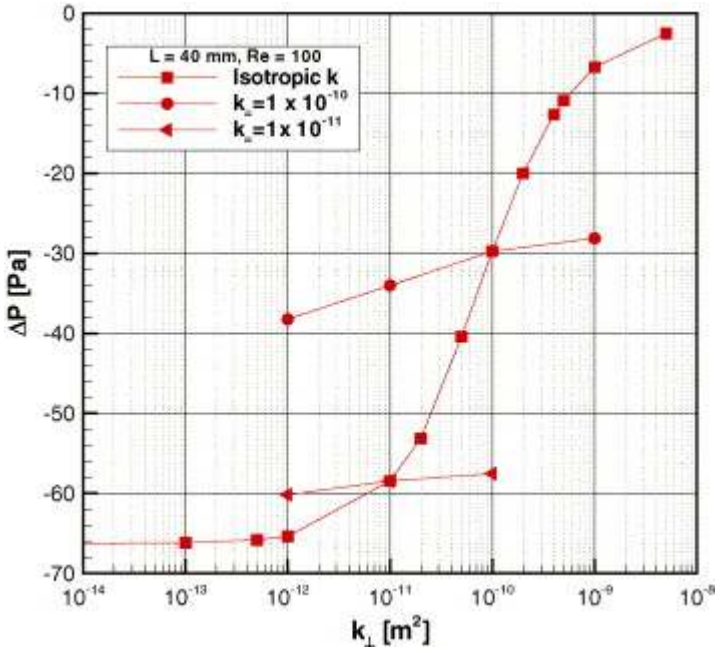

Figure 17: Effect of Anisotropic Permeability on Channel Pressure Drop [42]

Pharoah found that once the permeability is decreased to 1 x 10^{-12} m^2 there is a plateau, thus there is no further decrease in pressure drop. It was concluded that this indicates that none of the gas is making it into the GDL. On the other end, once the permeability increases to 1 x 10^{-9} m^2 there is another plateau, which indicates all of the gas is going through the GDL unimpeded [42]. For the two models with anisotropic permeability, Pharoah increased the through-plane permeability over two to three orders of magnitude while fixing the in-plane permeability. Pharoah found that significant

changes in through-plane permeability do not have a drastic effect on the resulting pressure drop, while changing the in-plane permeability by one order of magnitude, from 1×10^{-10} to 1×10^{-11} m^2, dramatically increases the pressure drop. This shows that the in-plane permeability has more of an effect on the resultant pressure drop than the through-plane permeability [42].

2.6 Permeability Testing

In addition to numerical simulations, many groups have conducted tests to characterize the air permeability of commercial GDLs. In this section, the test set-ups and results of five experimental studies are discussed.

2.6.1 Experimental Permeability Testing

Feser et al. used a radial flow apparatus, shown in Figure 18, to measure the in-plane air permeability of a carbon paper GDL, a non-woven carbon fiber GDL and a woven carbon cloth GDL under various levels of compression [50].

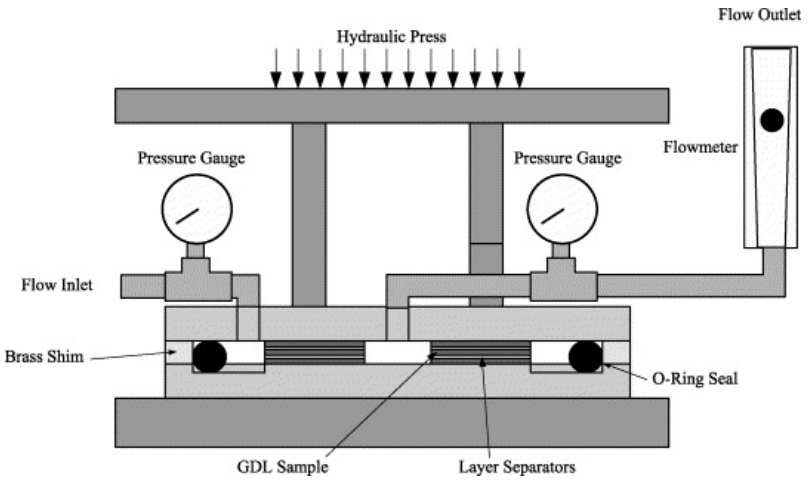

Figure 18: Radial Flow Apparatus used by Feser [50]

An expression relating flow rate to the pressure drop in radial coordinates was derived from Darcy's law. The original thickness of each sample was measured and averaged, then the samples were compressed using a hydraulic press. Air was pumped into an outer ring and through the GDL. The pressure drop and flow rate were measured with pressure gauges and a flow meter. The permeability of the samples tested is plotted against the porosity in Figure 19.

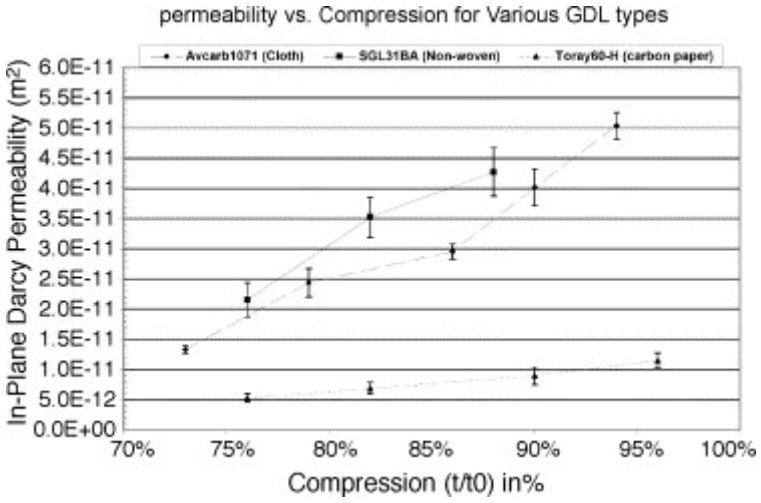

Figure 19: Permeability vs. Compression for Various GDLs [50]

Feser et al. found the non-woven carbon fibers (SGL 31BA) and the carbon cloth (Avcarb1071) had higher permeability under different levels of compression than the carbon paper (Toray 68-H).

Gurau et al. [51] tested the in-plane and through-plane permeability of four samples of carbon fiber cloth with different types of microporous layers, and one sample without a microporous layer to determine the permeability coefficients of the microporous layers. The permeability was assumed transversely isotropic in the in-plane direction, while the through-plane permeability had a different permeability. The in-plane and through-plane permeabilities were tested with equipment developed in-house.

The equipment allowed the flow rate to be controlled and the pressure drop to be measured. The Darcy-Forchheimer relationship, given by Equation 2.10, was used to determine the permeability coefficient using a least-squares fit. A typical set of data is shown in Figure 20.

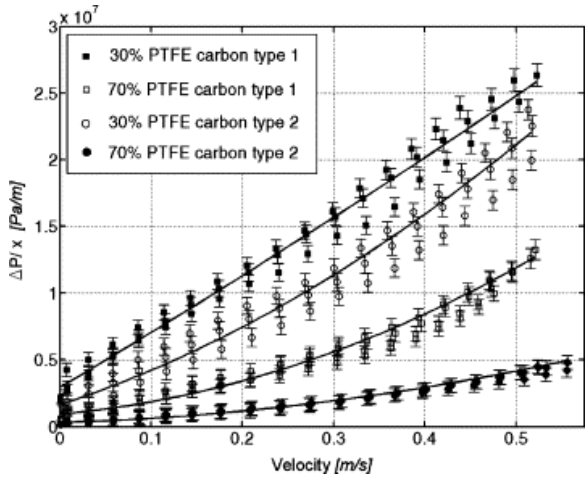

Figure 20: Pressure Gradient vs. Velocity for Various Carbon Cloth Samples [51]

The least-squares fit of these curves was set to the Darcy-Forchheimer equation to calculate the permeability coefficient. Gurau et al. found the in-plane and through-plane permeability values to be in a range of 1 x 10^{-12} m^2 to 20 x 10^{-12} m^2. They found that more PTFE in the microporous layer increased the permeability, which is contrary to literature that suggests higher PTFE content blocks pores and decreases air flow. The macroporous GDL exhibits higher permeability than GDLs with mircoporous layers which is consistent with literature. Also, the in-plane permeability tends to be higher than the through-plane permeability.

Ismail et al. [52] tested the through-plane permeability of a variety of untreated and PTFE-treated GDLs using an in-house test device, shown in Figure 21. They also ran a dimensional analysis on the Darcy-Forchheimer equation to study the effect of the Forcheimmer term on the permeability value. They used a mass flow controller to

control the flow from an air cylinder into the device and measured the pressure drop across the GDL.

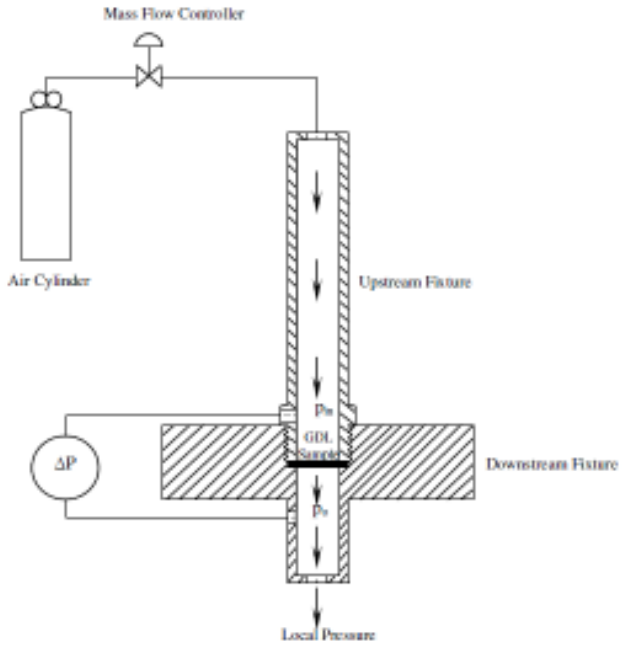

Figure 21: Through-Plane Permeability Test Set-Up [52]

The pressure drop was measured for at least 10 flow rates for each material and the mass flux of air vs. the pressure gradient was plotted for each material, as seen in Figure 22. A curve was fit to data and compared to the Darcy-Forchheimer equation to extract out the permeability for each sample.

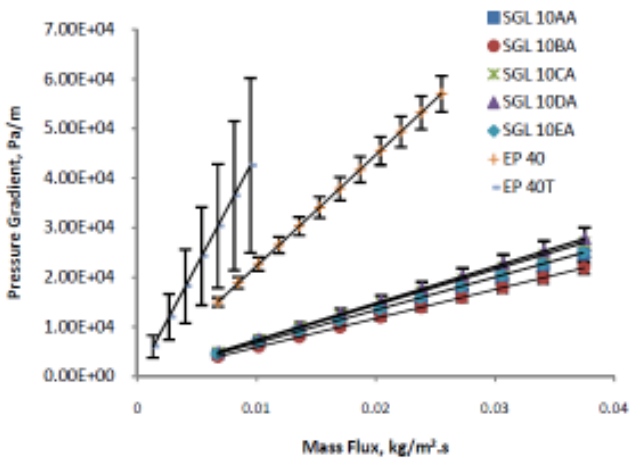

Figure 22: Pressure Gradient vs. Mass Flux for Through-Plane Permeability of GDL Samples [52]

Ismail et al. found there was an optimal amount of PTFE loading where the permeability was highest. Five samples, provided by SGL Technologies, had known PTFE loading while two samples provided by Ballard Power Systems had unknown properties. Therefore a comparison could not be made between the loading on the SGL materials and the Ballard materials. A dimensional analysis on the Darcy term and the Forchheimer term was conducted for a standard set of operating conditions. It was found that at the operating conditions used in the test, the Forchheimer term had a negligible effect on the results. Ignoring the Forchheimer effect only results in a 0.65% error, so the assumption that the Darcy term dominates and can be used to approximate through-plane permeability is valid.

Williams et al. [53] measured the through-plane permeability of four commercial carbon papers, three commercial carbon cloths and a carbon paper manufactured in-house. The test set-up was similar to the test set-up used by Ismail et al. A needle valve was used to control flow instead of a mass flow controller, and nitrogen was used as the impregnating gas. Each GDL was tested in a fuel cell. The limiting current is shown as a function of the permeability coefficient in Figure 23.

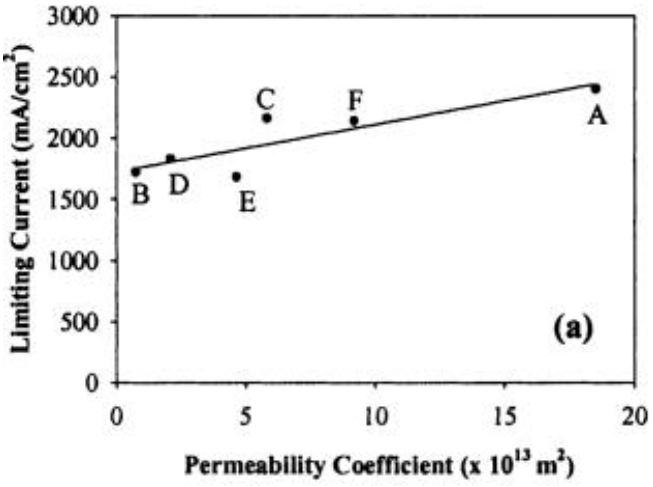

Figure 23: Limiting Current vs. Permeability Coefficient for GDLs [53]

It can be seen from the figure that the limiting current density increases as the permeability coefficient increases. They concluded that the limiting current increases because the GDL can remove water from the cell at higher current densities more efficiently so it does not block the pores needed for gas transport. The porosity of the GDLs was measured using mercury intrusion porosimetry and from weighing the samples before and after immersion in a wetting liquid which fills all the pores. The porosity found from the two techniques differed by less than 3.5%. A comparison of the porosity vs. the permeability coefficient for the materials tested is shown in Figure 24.

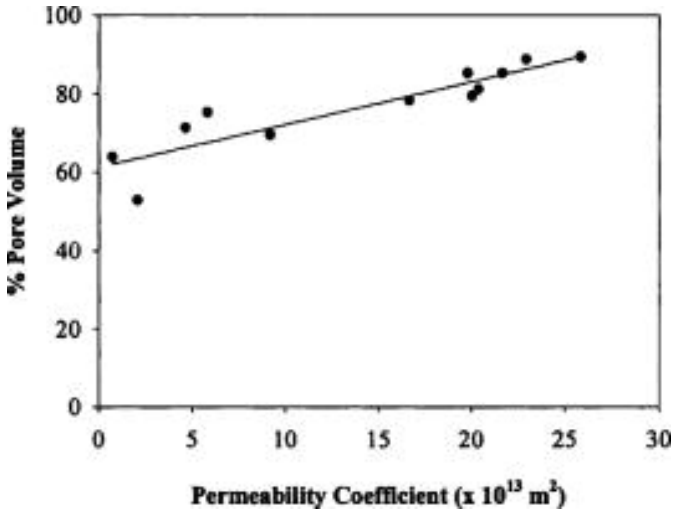

Figure 24: Pore Volume vs. Permeability Coefficient for Measured GDLs [53]

The graph shows the permeability coefficient increases with increasing pore volume, which makes sense because higher pore volume will decrease resistance to gas transport. This also shows that the common pore volumes for commercial GDLs are between 50% and 90%, which is an important parameter to consider in modeling.

Gostick et al. [34] measured the in-plane and through-plane permeability of six commercially available GDLs with two testing devices built in-house. In the in-plane testing device, shown in Figure 25 (a) - (c), a flow control valve was used to control the inlet flow rate into a channel. The sample was compressed to a known thickness using feeler gauges, and the flow rate was measured using a volumetric flow meter at the outlet. A pressure gauge measured the pressure drop between the two parallel channels on either side of the sample. The pressure drop was measured over a range of flow rates and feeler gauge thicknesses. The results for a typical material are shown in Figure 26.

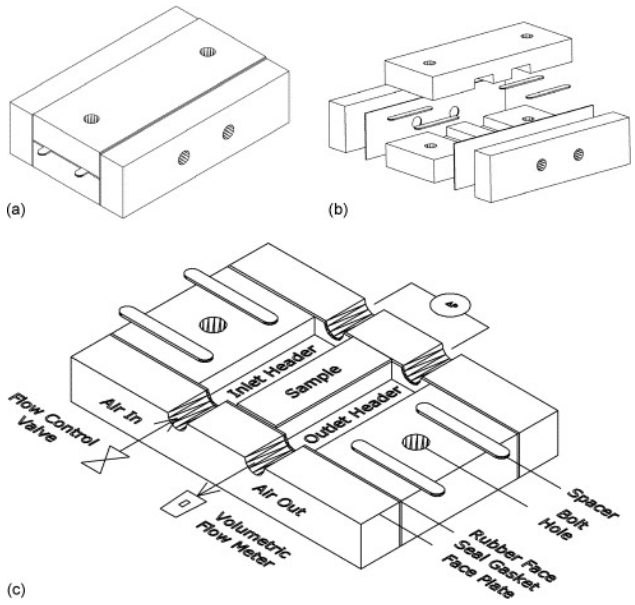

Figure 25: (a) In-Plane Permeability Testing Device, (b) Exploded View, and (c) Cutout View of the Inside of the Device [34]

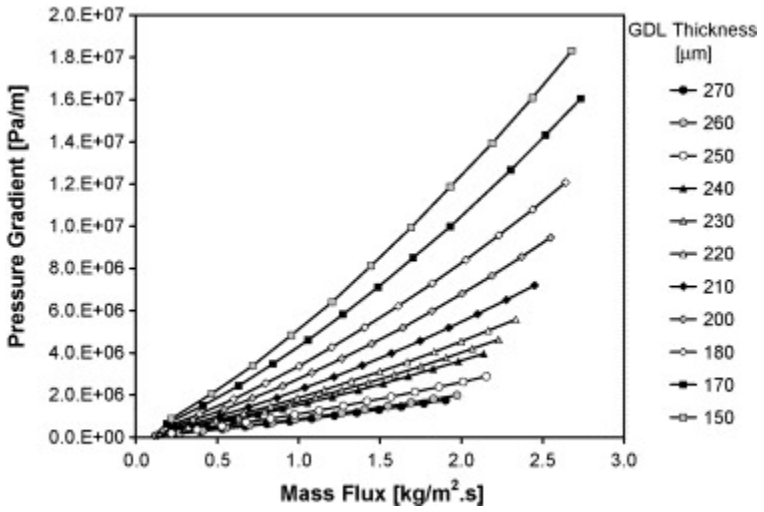

Figure 26: Pressure Gradient vs. Mass Flux for SGL 34BA [34]

Using a least-squares fit, the curve was compared to the Darcy-Forchheimer equation to calculate the permeability. The original porosity was measured using mercury intrusion porositmetry. After the permeability was calculated at each thickness, the permeability was plotted vs. the compressed volume fraction of material and the porosity of the material at each thickness, as shown in Figure 27 (a) and (b).

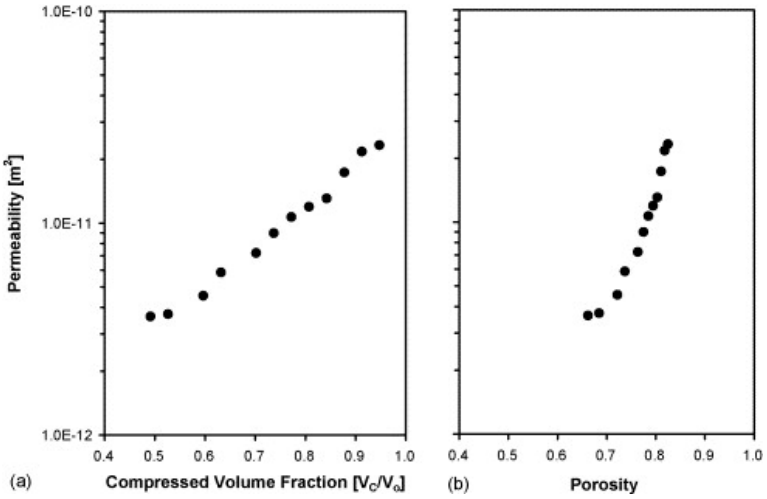

Figure 27: Permeabiliity vs. (a) Compressed Volume Fraction and (b) Porosity [34]

The uncompressed permeability could be backed out of the graph and compared to the through-plane permeability. To measure the through-plane permeability, circular samples were placed between two plates and compressed with bolt holes, as seen in Figure 28 (a) - (c).

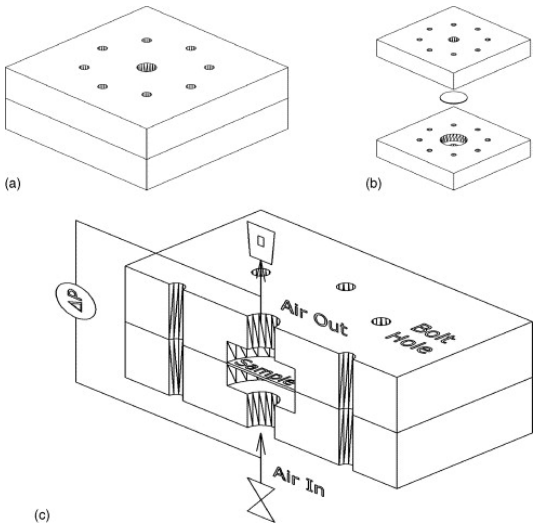

Figure 28: (a) Through-Plane Permeability Measurement Device, (b) Exploded View, and (c) Cutout View [34]

The pressure drop was again plotted against the inlet mass flux and the permeability coefficient was calculated from fitting the curve to the Darcy-Forchheimer equation. The Carman-Kozeny model and the Tomadakis-Sotirchos model were both compared to the curves of permeability vs. porosity and showed reasonable agreement. The Tomadakis-Sotirchos model showed better agreement, as it did not rely on a fitting parameter. It was found that the in-plane permeability was twice the through-plane permeability of commercial GDLs, which is consistent with the Gurau et al. Gostick et al. also state that the permeability range of typical commercially available GDLs is between 1 and 50 x 10^{-12} m^2, which is consistent with the findings of all the papers and is another parameter important for determining limits on modeling GDLs.

2.6.2 Permeability of Woven Structures

To the author's knowledge, there are no studies in literature linking the structure of woven GDLs to gas permeability. However, there are studies in textile research that look at the permeability of woven textile fabrics which are likely analogous to carbon fiber structures. The research in textiles exclusively looks at through-plane permeability, as through-plane permeability is more important than in-plane permeability in textiles.

Woven fabrics are manufactured by interlacing warp and weft fibers. Warp fibers are along the length of the fabric, while weft fibers are along the width of the fabric, as shown in Figure 29.

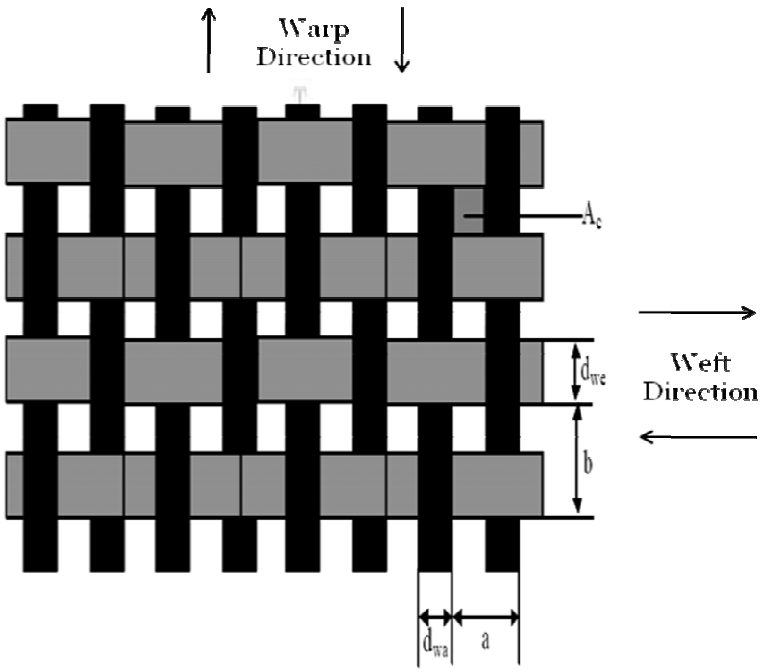

Figure 29: Diagram of Plain-Woven Fabric adapted from [54]

A_c is the cross sectional area of a pore. The diameter of the horizontal weft fibers is given by d_{we}, while the distance between the fibers is given by b. The diameter of the warp fibers is given by d_{wa} and the distance between warp fibers is given by a. The void spaces between the yarns and the voids between individual fibers that make up a yarn cause permeability of liquids and/or gases [54].

Permeability is determined by the structure of the weave, the amount of twist in the fibers, the size of the fibers and the density of fibers in the weave [55]. In a plain weave, a weft fiber goes over one warp fiber and under the next warp fiber. This single over-under pattern forms one unit which repeats itself. The same pattern is true for the warp direction. In a twill weave, one weft fiber will go over two consecutive warp fibers before going under two consecutive weft fibers, which forms a repeating unit. A twill-woven pattern is shown in Figure 30.

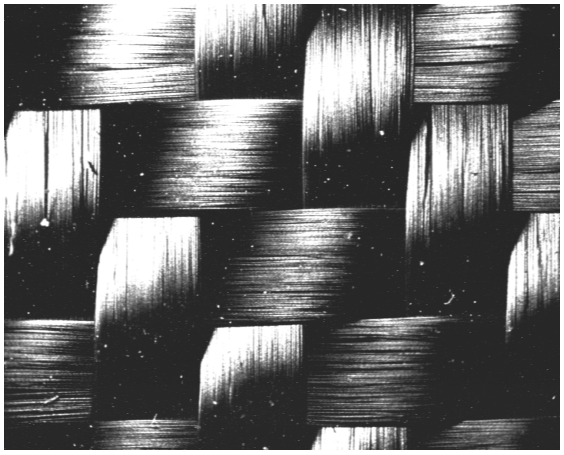

Figure 30: Twill Weave

Feather and Anderson [55] measured the permeability of plain, twill and hopsack weaves with varying tightness by increasing the number of fibers per unit length. They found that the through-plane permeability decreased as the fiber linear density increased. They also found that the plain weave had the lowest air permeability of all structures tested.

Epps and Leonas [56] investigated the permeability of ten different woven fabrics with a liquid porosimetry technique. They found that the permeability is highly correlated to the minimum pore size, but also depends on the mean pore size and porosity. Ogulata [54] studied the air permeability of woven structures with a different number of weft yarns per cm (i.e. tightness). He also found the permeability decreased with an increasing number of weft fibers per cm, which shows a correlation between the porosity and the air permeability. As the number of fibers increase, there is less void space between fibers, which decreases porosity and air permeability.

2.7 Summary

In this review, the theory behind PEM fuel cell performance measurement and modeling approaches were discussed. Porous media modeling and GDL modeling was discussed in more detail. Literature detailing the results of numerical simulations of permeability in GDLs, and literature detailing methods to test the gas permeability of conventional GDLs was presented. Also, some theory on the permeability of woven structures was discussed. In Chapters 3 and 4 of this thesis, two numerical studies in which the permeability of GDLs is varied are developed using the theory discussed in Sections 2.2 through 2.5. In Chapter 5, woven GDLs are made in-house and tested on equipment built in-house, which follow the analytical techniques presented in Section 2.6, in order to enhance our understanding of permeability and flow through GDLs in PEM fuel cells.

CHAPTER 3

FLUENT MODEL WITH CHANGE IN PERMEABILITY

3.1 Motivation

In the fuel cell stack design proposed by Bhamidipati et al. [22], the GDL needs to control the gas distribution over the face of the electrode. In order to distribute gas evenly and create a uniform current density, it is hypothesized that the GDL will need to exhibit an anisotropic and controlled resistance to flow. There is a significant in-plane pressure gradient due to the placing of the inlets on the sides of the GDL. This in-plane pressure gradient will cause the air to quickly exit the fuel cell through the outlet before it reaches the catalyst layer. To overcome this pressure gradient, the in-plane resistance must be higher to keep the air in the fuel cell.

In this chapter, the effects of changing the resistance profile, changing the thickness of an unconventional GDL and changing the air stoichiometry on the average current density and current density distribution are investigated with a numerical model. The model is solved using a commercial computational fluid dynamics software, Fluent 6.3.26. In the half-cell model of a fuel cell cathode, the gas flow is solved in 3-D, while a zero-D equation is used to solve for the expected current density. The half cell model is split into four regions with anisotropic permeability profiles, and the in-plane permeability near the inlet is increased. The purpose of this model is to see how permeability profiles affect gas flow trends through the GDL.

3.2 Computational Model

In the following section, the computational modeling domain, assumptions, governing equations, boundary conditions and modeling approach are discussed. A model from literature is replicated for validation.

3.2.1 Modeling Domain

Only the cathode side of the fuel cell will be modeled, because the kinetics are dominant in the region and the computational complexity and time will be significantly reduced. Models that only consider the cathode are called half-cell models and are common throughout literature [26-27, 35, 44, 57-58]. These models assume that the anode is run at conditions which can fully keep up with the current generated at the cathode. The anode reaction, called the hydrogen-oxidation reaction, involves platinum splitting a hydrogen atom into two electrons and two protons, given by the following chemical equation,

$$H_2 \Rightarrow 2H^+ + 2e^- \tag{3.1}$$

On the cathode, the oxygen-reduction reactions consists of platinum splitting an oxygen molecule into two oxygen atoms and combining them with the protons and electrons from the anode reaction to form water, which is given by the following chemical equation,

$$\frac{1}{2}O_2 + 2H^+ + 2e^- \Rightarrow H_2O \tag{3.2}$$

The kinetics of the oxygen-reduction reaction are much slower than the hydrogen-oxidation reaction, causing the activation overpotential from the cathode reaction to be much higher. Since fuel cell performance is so dependent on the oxygen transport and reaction at the cathode, it is reasonable to model only the cathode. The modeling domain includes the cathode catalyst layer and the cathode GDL, as depicted in Figure 31.

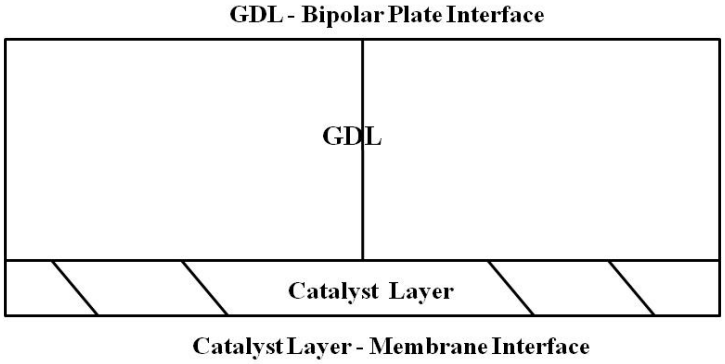

Figure 31: Side View of Modeling Domain

Only the gas flow is modeled in the GDL and catalyst layer. Electronic and ionic transport is considered in a future model. The model is split into four separate regions, labeled 1_1, 1_2, 2_1 and 2_2, where the gas permeability can be controlled in the two in-plane directions (x- and y-) and the through-plane direction (z-), as depicted in Figure 32.

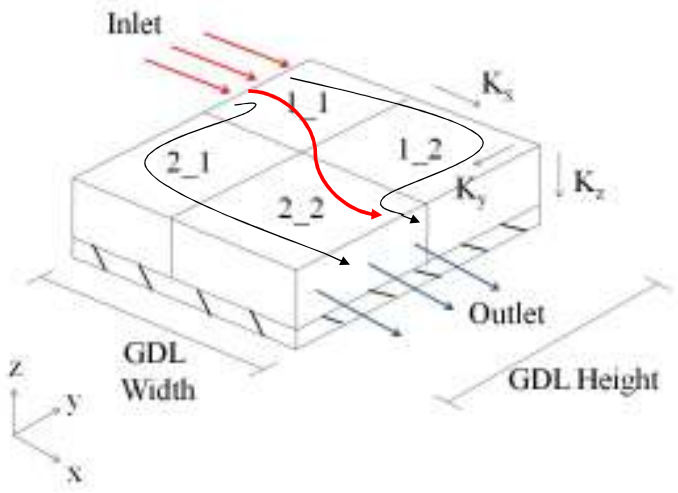

Figure 32: GDL and Catalyst with Subdomains Labeled

The placement of the inlets and outlets on the sides of the cell will induce a large in-plane pressure gradient which will force flow to go directly from the inlet to the outlet. This will create 'dead zones' in the corners of the cell furthest away from the inlet and outlet. It is desirable to create a flow resistance profile that will allow the oxygen rich air to reach the corners at the same rate it reaches the rest of the cell to attain uniform distribution of reactants and consequently, uniform current density.

3.2.2 Problem Solving Methodology

The first step is to find a desired point of operation for the fuel cell by generating a polarization curve. The Nernst potential is calculated using Equation 2.2. The operating voltage is found by subtracting the losses using Equation 2.6, and the three main types of losses are given in Equations 2.3, 2.4 and 2.5. The operating conditions and design parameters are given in Table 2.

Table 2: Operating Conditions and Design Parameters

Operating Condition or Design Parameter [units]	Value
GDL Height [mm]	10
GDL Width [mm]	10
Catalyst Layer Thickness [mm]	0.01
P_{op}**, Operating Pressure [atm]**	1
P_{std}**, Standard Pressure [atm]**	1
T**, Operating Temperature [°C]**	80
R**, Gas Constant [J/(mol·K)]**	8.314
F**, Faraday's Constant [C/mol]**	96,485
α**, Charge transfer coefficient**	0.5
r**, Area specific resistance [Ωcm^2]**	0.4
i_o**, Exchange current density [A/cm^2]**	$1 \cdot 10^{-5}$
i_l**, Limiting current density [A/cm^2]**	1.5
X_{O_2}**, Inlet Mol Fraction O_2**	0.2
$X_{H_2O_c}$**, Inlet Mol Fraction, H_2O cathode**	0.1
X_{N_2}**, Inlet Mol Fraction, N_2**	0.7
X_{H_2}**, Inlet Mol fraction H_2**	0.2
M_{O_2}**, Molar mass of oxygen [kg/mol]**	0.032
M_{H_2O}**, Molar mass of water [kg/mol]**	0.018
M_{N_2}**, Molar mass of nitrogen [kg/mol]**	0.028
ψ_{O_2}**, Diffusion volume O_2 [m^3/mol]**	$16.6 \cdot 10^{-6}$
ψ_{H_2O}**, Diffusion volume H_2O [m^3/mol]**	$12.7 \cdot 10^{-6}$
ψ_{N_2}**, Diffusion volume N_2 [m^3/mol]**	$17.9 \cdot 10^{-6}$
k**, diffusion pre-factor [Pa·m^2/s]**	$3.16 \cdot 10^{-8}$

Using these operating conditions, Figure 33 is obtained where the polarization curve is plotted against the power density. The power density is calculated by multiplying the current density and operating voltage. The operating point of 1 A/cm^2 is chosen for this study. At this operating point, the power density is near the maximum power density. A slight increase in current density would cause a significant decrease in voltage and power density as the concentration losses would become dominant. This is a typical operating point for modeling studies [35, 59].

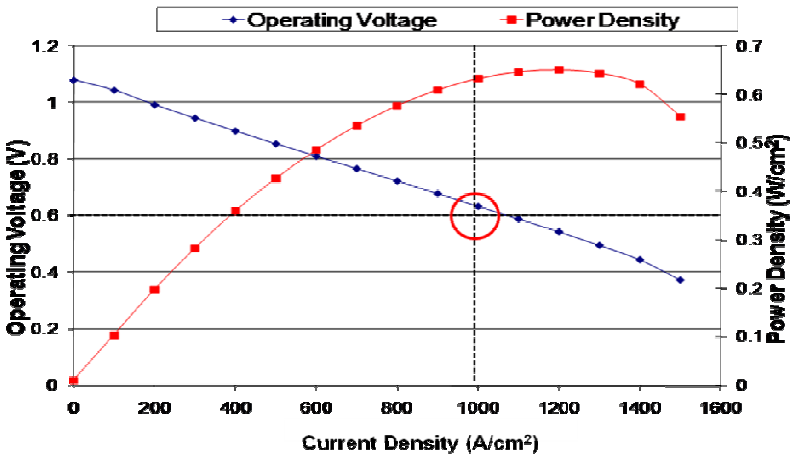

Figure 33: Polarization Curve

After choosing an operating point, the mass flux, q, of oxygen consumed at the electrode is calculated using Faraday's law, which relates the flux of oxygen consumed at the electrode to the current density,

$$q = \frac{M_{O_2} i}{4F} \tag{3.3}$$

The mass flow rate, $\dot{m}$, into the cell is found using the mass flux of oxygen consumed at the electrode, the amount of oxygen in the air stream and the air stoichiometry,

$$\dot{m} = \frac{q A_{electrode} \xi}{x_{O_2}} \tag{3.4}$$

where ξ is the air stoichiometry. After the model is run, the mass flux of oxygen at the interface between the catalyst layer and GDL from the simulation is put back into Equation 3.3 to find the expected current density.

3.2.3 Modeling Assumptions

The modeling assumptions for the simulations include:

- Sufficient cooling is provided to consider the cell isothermal,
- Steady state conditions,
- Ideal gas conditions,
- The current equations are not solved. Reactions are modeled in a thin catalyst layer as finite-rate volumetric source or sink terms (source terms for water production and sink terms for oxygen consumption),
- The flow is laminar and incompressible, and
- Water is treated as a single phase in its vapor form. While this assumption is a significant limitation, many investigators assume single-phase flow models [28-30, 35-36, 39-40, 49]. Since the operating point was chosen to stay away from the concentration loss region of the polarization curve, it is assumed water flooding effects will not be significant.

3.2.3.1 Isothermal Assumption

To justify the assumption of isothermal conditions, sufficient cooling must be provided to remove the heat generated by the electrochemical reactions. For a small system, air could be blown over cooling fins placed in between the two stacks. Equation 3.5 can be used as an approximation for how much heat is generated by a fuel cell stack.

$$Q = I(1.25 - V) \tag{3.5}$$

where Q is the heat flow, I is the current and V is the operating voltage. For the cell considered in this study, this heating rate is 0.65 watts. Since the heat will be removed by a cooling fan blowing over a fin, heat transfer will be due to convection, which is represented by Equation 3.6,

$$Q = h_c A(T_s - T_\infty) \tag{3.6}$$

where h_c is the convection coefficient, A is the area of the cooling fin, T_s is the temperature of the cell and T_∞ is the temperature of the surroundings, which are assumed to be 25 degrees Celsius. The convection coefficient is calculated using the equation for the Nusselt number for laminar flow over a flat plate,

$$Nu = \frac{h_c L}{k_T} = 0.664\,\mathrm{Re}^{1/2}\,\mathrm{Pr}^{1/3} \tag{3.7}$$

where Nu is the Nusselt number, L is the length of the plate, k_T is the thermal conductivity of the metal, Re is the Reynolds number, given by Equation 3.8, and Pr is the Prandtl number, which is assumed to be 0.707 for air at room temperature.

$$\mathrm{Re} = \frac{\rho v L}{\mu} \tag{3.8}$$

To cool a system on this scale, a small case fan could be used, which have volumetric flow rates between 20 and 80 ft^3/min. This translates to velocities between 1.9 and 7.5 m/s. Assuming a velocity of 5 m/s, the heat removal rate, calculated by Equation 3.6, is 0.95 W. This shows that a small case fan could easily cool this system and justifies the isothermal assumption.

3.2.4 Governing Equations

To solve for the reactant distribution in the porous media, fundamental equations of mass conservation, momentum conservation and species transport must be solved. In

this section, the governing equations for species transport and momentum transport are discussed.

3.2.4.1 Continuity

Mass conservation is modeled using the continuity equation given by,

$$\nabla(\rho v) = S_m \tag{3.9}$$

The source term, S_m, is given by the reaction rate in the catalyst layer. The source terms for oxygen consumption and water production are calculated from the form of Faraday's law given in Equation 3.3. Equation 3.3 is mulitiplied by the active area of the electrode and divided by the volume of the catalyst. For oxygen consumption and water production, this turns out to be Equations 3.10 and 3.11 respectively,

$$S_{O_2} = -\frac{M_{O_2} i A_{electrode}}{4F} \frac{1}{\forall} \tag{3.10}$$

$$S_{H_2O} = \frac{M_{H_2O} i A_{electrode}}{2F} \frac{1}{\forall} \tag{3.11}$$

where $\forall$ is the volume of the catalyst layer. The average mixture density is calculated by,

$$\rho = \sum_{i=1}^{k} X_i \rho_i \tag{3.12}$$

3.2.4.2 Momentum and Mass Transport

The pressure drop in the porous medium is modeled using Darcy's Law, given in Equation 2.11, which is discussed in Section 2.3. The species transport is governed by the species transport conservation equation,

$$\nabla \cdot \left(\rho v Y_i \right) = -\nabla \cdot N_i + R_i \tag{3.13}$$

where Y_i is the mass fraction of species i, N_i is the diffusion flux of species i, and R_i is the net rate of production of species i through chemical reaction. The diffusion flux vector can be solved for in the Maxwell-Stefan equation given in Equation 2.7 in Section 2.3.

3.2.5 Boundary Conditions

The boundary conditions at the inlet, outlet and walls for species and momentum transport include:

- *Inlet*

  At the inlet, the mass flow rate is specified as the result of Equation 3.4. The mass fraction of oxygen and water are specified at the inlet for the Maxwell Stefan diffusion equations.

  Mass Fraction O_2 : 0.230

  Mass Fraction H_2O : 0.065

  The remaining mixture is nitrogen.

- *Outlet*

  At the outlet, a pressure outlet is specified as gauge = 0

- *Walls*

A no-slip condition based on a Darcy factor of 10^{-6} is used. The no-flux condition is used for species transport at the walls. The wall conditions are applied at the top, bottom and side walls of the modeling domain.

In a porous medium, the gas interacts with the pore walls and the walls of the conducting plate, which is inconsistent with the no-slip boundary condition [60]. Parvazinia et al. showed that at low Darcy factors, which correspond to low permeability, the results between the slip and no-slip boundary conditions were negligible [60]. In this study, low permeabilities are considered, thus the no-slip boundary condition is used.

3.2.6 Validation Study

To validate the proposed operating conditions and boundary conditions, a comparative study has been conducted with work conducted by Wang et al. [61]. They developed a model to study the effects of the shape of the flow channels on the cell performance. They compared the interdigitated flow channel design to a parallel flow channel at two different operating voltages, 0.3 V and 0.7 V. The dimensions of the cell are 23 mm x 23 mm with a 0.4 mm thick GDL and a 0.005 mm thick catalyst layer and 12 gas channels. Wang et al. developed a polarization curve for the model shown in Figure 34.

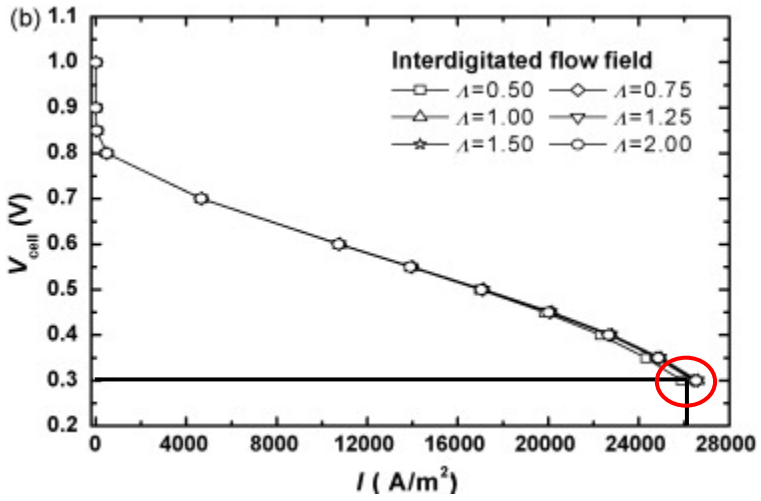

Figure 34: Interdigitated Flow Field Polarization Curve Developed by Wang et al. [61]

For an operating point of 0.3 V, an average current density of 26,000 A/m^2 was used as the desired current density. Wang et al. reported the oxygen mass flux between the cathode catalyst layer and the cathode GDL. The validation model was run under the operating conditions given in Table 3 in addition to the governing equations and boundary conditions discussed in the preceding sections.

Table 3: Operating Conditions for Validation Model

Operating Condition [units]	Value
Temperature [K]	323
Relative Humidity of Air	100%
Inlet Flow Rate [cm^3/min]	700
Operating Pressure [atm]	1
GDL Permeability [m^2]	1.76 x 10^{-11}

The mass flux of oxygen into the cathode catalyst layer from the validation study was compared to the results reported by Wang et al. The mass flux of oxygen is plotted against the x- position through the cell at a cross section of 11.5 mm in Figure 35.

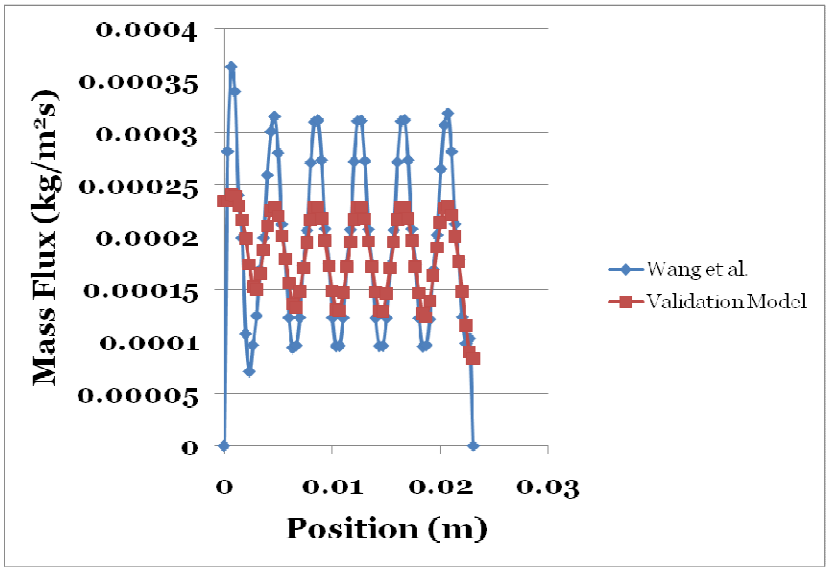

Figure 35: Mass Flux of Oxygen into Cathode Catalyst Layer vs. Position at 11.5 mm Cross Section

Wang et al. considers liquid water transport, fully coupled charge transport and a full cell model, while the validation model used in this study is single-phase, with a zero-D polarization model of a cathode half-cell. While the values from the validation model do not match the values given by Wang et al., as would be expected given the simplification of the half-cell model, the trend was in very good agreement. Since the purpose of this study is to see how changes in permeability affect gas flow trends, and the model used in this study can predict similar flow behavior, this model is considered sufficient for the purposes of this study. The next study in Chapter 4 considers a model with fully coupled charge transport in the GDL and the membrane.

3.3 Simulations

In this section, four permeability conditions for the half-cell model were considered in this study. As was discussed in Section 3.2.1, the model is split into four rectangular modeling domains where the permeability can be independently modified in the x-,y- and z- direction. The upper and lower limit for the range of chosen permeability

values, 1 x 10^{-10} to 1 x 10^{-12} m^2, was chosen based on values reported by groups that tested permeability of GDLs [34]. With the inlet and outlet on either side of the gas diffusion layer, there is a large in-plane pressure gradient which will cause the air to travel quickly through the GDL from the inlet to the outlet. The goal is to transport the oxygen-rich gas in the through-plane direction to the catalyst sites and achieve uniform distribution. To combat this in-plane pressure gradient, the GDL structure will be manipulated such that the in-plane permeability is much lower than the through-plane permeability. This is the opposite resistance profile seen with conventional GDLs [34].

The permeability in all four permeability test cases is transversely isotropic, meaning the permeability in the x- and y- direction is the same. The permeability values in the four regions for each test case are shown in Table 4. Region 1_1 is closest to the inlet, while region 2_2 is closest to the outlet. Since the region near the inlet is exposed to the most oxygen rich air, it is desirable to transport the fuel to the regions away from the inlet before the oxygen is consumed to help distribute reactants more uniformly. In Cases 1 - 3, the in-plane permeability is 1 x 10^{-12} m^2 and the through-plane permeability is 1 x 10^{-10} m^2 in every region except the region directly next to the inlet (Region 1_1). In Region 1_1, the through-plane permeability is set to 1 x 10^{-12} m^2, while the in-plane permeability is increased from 1 x 10^{-12} to 5 x 10^{-12} m^2. It is expected that as the in-plane permeability near the inlet increases, the average permeability throughout the GDL will decrease as the gas can reach the outlet easily. It is also expected that the uniformity will be better as the in-plane permeability in Region 1_1 increases because there will be less resistance for the air to reach the dead zones in the corners of the GDL.

The permeability values in Case 4 are representative of the permeability of a conventional GDL. The in-plane and through-plane permeability were calculated from the Tomadakis-Sotirchos equation, Equation 2.13, assuming a fiber diameter of 8 μm and a porosity of 0.8, which are typical values for common GDL materials [34].

Table 4: Permeability Values in GDL (m^2)

GDL region	Case 1	Case 2	Case 3	Case 4
1_1 in-plane	1E-12	2E-12	5E-12	1.1E-11
1_1 through-plane	1E-12	1E-12	1E-12	7E-12
1_2 in-plane	1E-12	1E-12	1E-12	1.1E-11
1_2 through-plane	100E-12	100E-12	100E-12	7E-12
2_1 in-plane	1E-12	1E-12	1E-12	1.1E-11
2_1 through-plane	100E-12	100E-12	100E-12	7E-12
2_2 in-plane	1E-12	1E-12	1E-12	1.1E-11
2_2 through-plane	100E-12	100E-12	100E-12	7E-12

3.3.1 Effects of Graduating Permeability on Distribution

The effects of the changing the permeability in the region near the inlet (Case 1-3) on the average current density and the uniformity of the current density distribution are compared to the traditional GDL (Case 4). Figure 36 (a-d) shows the expected current density distribution at the catalyst layer/GDL interface. Refer to Figure 32 for a reference on the position of the inlets and orientation of the modeling domain.

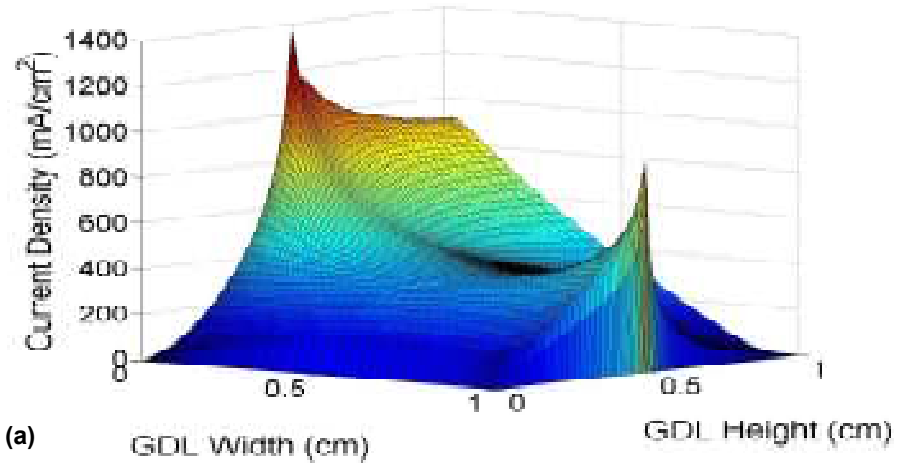
Current Density (mA/cm2)
1400
1200
1000
800
600
400
200
0
0.5
1
0
0.5
1
GDL Width (cm)
GDL Height (cm)

(a)

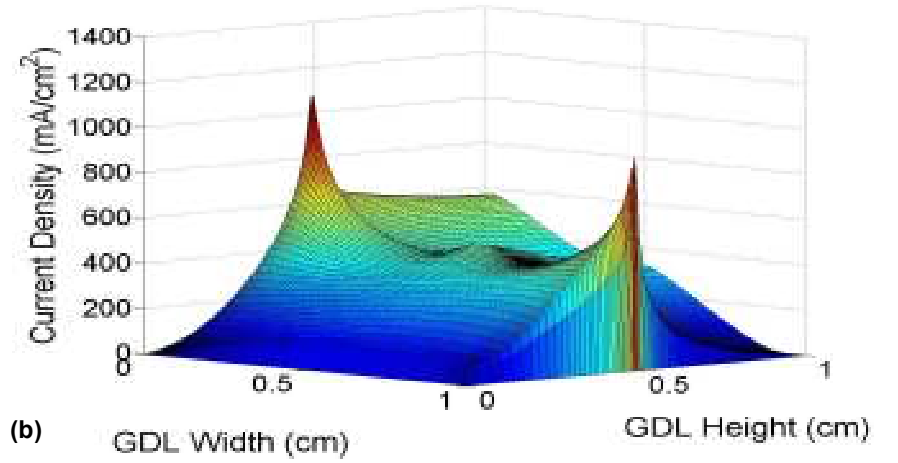
Current Density (mA/cm2)
1400
1200
1000
800
600
400
200
0
0.5
1
0
0.5
1
GDL Width (cm)
GDL Height (cm)

(b)

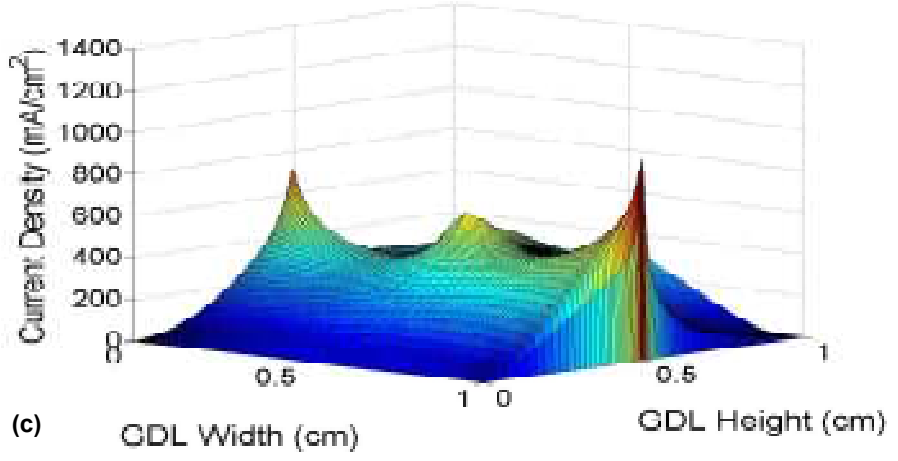
Current Density (mA/cm2)
1400
1200
1000
800
600
400
200
0
0.5
1
0
0.5
1
GDL Width (cm)
GDL Height (cm)

(c)

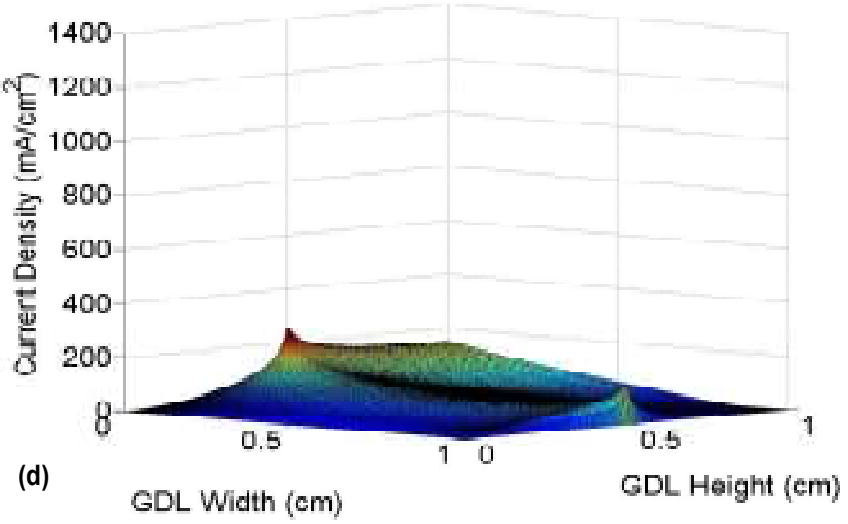

Figure 36: Effects of Varying Permeability on Current Density Distribution with a 0.4 mm Thick GDL at 1.33 Gas Stoichiometry: (1) Case 1, (b) Case 2, (c) Case 3, and (d) Conventional Case [62]

One trend seen in all the cases is high current densities in Region 1_1 near the inlet. Current density is dependent on the mol fraction of oxygen and the velocity at which oxygen is provided to the catalyst site. In Region 1_1, the oxygen has not been consumed which leads to higher mol fractions of oxygen and higher current densities. The current spikes near the inlet and outlet are due to high velocities as the gas flows around the edges at the corners of the manifold. Another similar trend is a 70-90% current density drop in the dead zones. The easiest path for the gas to travel is directly to the outlet which leads to lower velocities in the corners of the cell and lower current densities [62].

Further comparing the cases, Case 1 shows higher current densities near the inlet, where the in-plane permeability is lower, which causes more in-plane resistance as the air moves towards the outlet. This leaves more oxygen available for reactions near the inlet, which leads to higher current densities. In Cases 2 and 3, the current density values drop 20-40% because the air can travel with less resistance to other parts of the cell, but the

uniformity of the current density distribution is better [62]. The current density distribution in Case 4, the traditional case, appears more uniform than Cases 1-3, but the average current density values are 85% lower than Case 1. In conventional GDLs, the in-plane permeability is higher than the through-plane permeability, which allows the air to exit the cell before it can reach the catalyst sites.

To better understand the uniformity, it is necessary to look at how much the magnitude of the current density throughout the cell deviates from the average. The standard deviations of current density and average current density for each case are plotted in Figure 37.

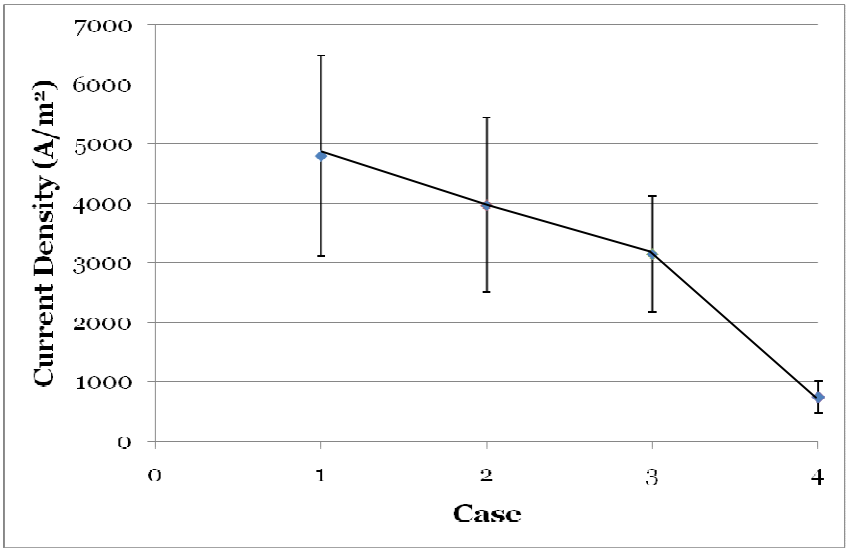

Figure 37: Average Current Density with Standard Deviation of Current Density for Each Case

A larger standard deviation of current density means current densities are further from the average value, which is a result of a non-uniform distribution. In Case 1, it can be concluded there is a non-uniform distribution at the catalyst layer due to the high standard deviation of current density, as seen in Figure 36 (a). Considering all 4 cases, it can be concluded there is a trade-off between standard deviation of current density and the magnitude of the average current density. As in-plane permeability increases, the

magnitude of the average current density and the standard deviation of current density both decrease. This shows that the distribution is more uniform, but the average amount of current produced is lower. There is a 21% drop in average current density between Cases 2 and 3, but the standard deviation only decreases 13%. This means the permeability profile in Case 2 can produce a higher average current density without a substantial decrease in uniformity [62]. This region will serve as a starting point for further optimization.

3.3.2 Effect of Changing Thickness

To study the effect changing GDL thickness has on performance, simulations were run at three different thicknesses (0.4, 0.5, and 0.6 mm). The mass flow rate is calculated at a gas stoichiometry of 1.33. The average current density as a function of GDL thickness is plotted in Figure 38, for all four cases.

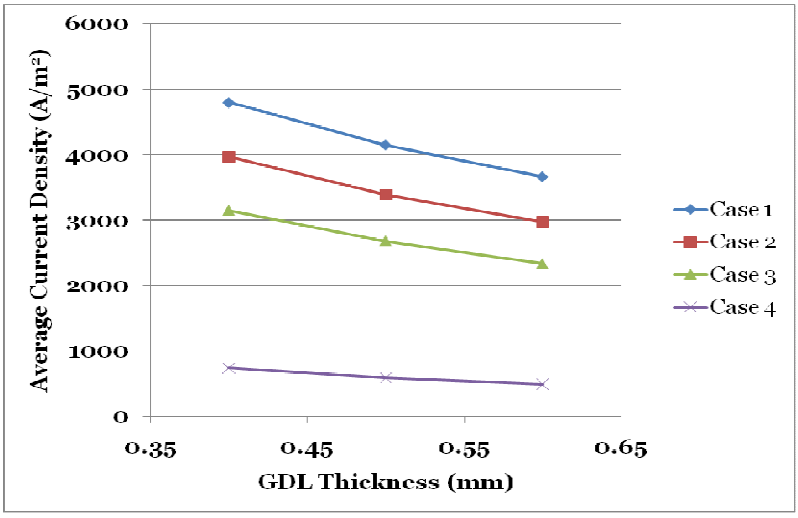

Figure 38: Average Current Density at Different Thicknesses

As the GDL thickness increases, the average current density decreases, as seen in Figure 38. In a thicker GDL, the same amount of air is supplied at a lower velocity due to the larger cross sectional area of the GDL. Thus, the rate at which each region is

supplied with fuel decreases resulting in lower current densities. This result is consistent with literature, which suggests thinner GDLs perform better. In order to study the uniformity, the standard deviation was considered as a metric to quantify the deviation in current density from the average current density at the catalyst sites. To better understand the mechanisms affecting overall uniformity, a ratio, defined by the standard deviation of current density /average current density, is introduced. For example, consider two cases with the same standard deviation of current density and different average current densities. The case with the higher average current density has a better overall uniformity because the current density deviates by the same amount from a higher average. In Table 5, the ratio of the standard deviation of current density to average current density is shown for the simulations in Figure 38.

Table 5: Ratio of Standard Deviation of Current Density at Varying Thicknesses

Thickness (mm)	Case 1	Case 2	Case 3	Case 4
0.4	0.70	0.56	0.62	0.74
0.5	0.69	0.55	0.63	0.75
0.6	0.69	0.55	0.64	0.76

A lower ratio is desirable because a lower ratio results from a lower standard deviation or a higher average current density. When comparing the standard deviations of current density between the four cases in Figure 37, Case 4, the conventional GDL, appears to have a better uniformity due to a lower standard deviation of current density. However, Case 4 has a much lower average current density than the other cases, which is undesirable. Case 4 represents conventional GDL material properties, which exhibit higher in-plane permeability than through-plane permeability. Thus, it is necessary to

design a GDL with higher through-plane permeability than in-plane permeability for the unconventional design. Case 2 is found to have the best overall uniformity when comparing the average values. This indicates the in-plane permeability near the inlet must be slightly higher than the in-plane permeability in the rest of the cell in order to transport the air to starved regions of the electrode. As shown in Table 5, the ratio is independent of the thickness. This means that as the GDL thickness increases and the average current density decreases, the standard deviation decreases at the same rate [62].

A limitation of this type of analysis is that the ratio does not necessarily provide a quantitative indication of the best conditions. For example, if a cell were running at an average current density of 10 mA/cm^2 with a standard deviation of 2 mA/cm^2, the ratio would be 0.2. This low ratio indicates good overall uniformity, but the average current density is too low for any realistic application. Therefore, the average current density must be considered per application when looking for the best conditions.

3.3.3 Effect of Gas Stoichiometry

To study the effect of changing the gas stoichiometry on current density and overall uniformity, simulations were run at a single thickness, 0.4 mm, at three different gas stoichiometries. The average current density as a function of stoichiometry is shown in Figure 39.

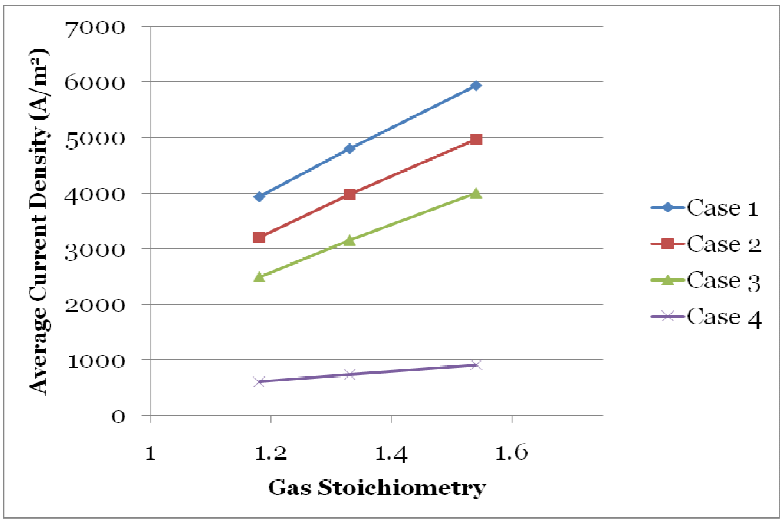

Figure 39: Gas Stoichiometry vs. Average Current Density

As expected, the average current density increases as the gas stoichiometry increases, because more air is pumped into the GDL. Similarly, the cases with the higher in-plane resistance show higher average current densities. In Table 6, the ratio of standard deviation of current density to average current density is shown.

Table 6: Ratio of Standard Deviation of Current Density to Average Current Density for Different Gas Stoichiometries

Stoichiometry	Case 1	Case 2	Case 3	Case 4
1.54	0.63	0.53	0.63	0.68
1.33	0.70	0.56	0.62	0.74
1.18	0.79	0.63	0.63	0.85

In contrast to changing thickness, which was shown to have an overall uniformity independent of GDL thickness, it can be seen in Table 6 that the ratio increases as the stoichiometry decreases. From this, it can be concluded that as the stoichiometry decreases and the average current density decreases, the standard deviation does not decrease at the same rate. Thus, a better uniformity can be achieved by operating at

higher current densities. Similar to the thickness study, Case 2 has the lowest ratio and best overall uniformity. In Case 3, the ratio does not change significantly with a change in stoichiometry. It is desirable for the ratio to be independent of gas stoichiometry, as the overall uniformity will not be affected if more gas is pumped into the cell in an attempt to increase the average current density. It can be concluded that an optimum permeability profile exists between Case 2 and Case 3, which provides efficient overall uniformity and is robust with changes in gas stoichiometry [62].

3.3.4 Conclusions

The effect of changing permeability, thickness and gas stoichiometry on current density magnitude and overall uniformity were investigated for an unconventional GDL. Results indicate that as the in-plane permeability increases, the magnitude of the current density decreases. For the unconventional design, it is necessary for the GDL to have an in-plane permeability, which is much lower than the through-plane permeability, such that the in-plane resistance is increased in order for the fuel cell to run at a reasonable current density and achieve better overall uniformity. As thickness increases, the magnitude of the current density decreases, while reactant distribution is independent of thickness. As a general trend, a decrease in gas stoichiometry leads to an increase in the magnitude of the current density while uniformity decreases [62].

From this study it has been learned that the permeability can be optimized to provide a higher current density and better uniformity. More work is needed to understand how different parameters affect different designs and the conditions which provide the highest overall current density with the optimal uniformity. Ideally, a more robust model that solves the partial differential equations for current, coupled to the mass

transport would give more accurate results. Also, a model that looks at spatially varying permeability rather than regions with a constant permeability is desired. The model in Chapter 4 considers a more robust 3-D flow model with the partial differential equations for potential coupled to the mass transport.

CHAPTER 4

FULLY COUPLED 3-D COMSOL MODEL

4.1 Motivation

In the previous model, gas flow trends were analyzed in four different regions of a GDL with varying permeability in four separate regions of the GDL. While this model was useful to see how permeability affects flow resistance, it utilized a simple equation for assessing the current density throughout the GDL which was not coupled to the equations describing the gas transport. The model also had four separate regions with abrupt changes in permeability. It is desirable to investigate the effect of a gradual change in a permeability profile to truly assess the effect the permeability has on the current density.

In this chapter, a model is developed which considers a gradual change in the permeability profile with space-varying permeability. The permeability changes as a function of position based on one of three polynomial expressions; a linear decreasing permeability, a convex parabolic decrease and a concave parabolic decrease. In the model considered in this chapter, the mass transport is coupled to the charge transport, and the partial differential equations for current are directly solved. The effect of the graduated permeability profile, changes in thickness and changes in gas stoichiometry on average current density and uniformity of current density are investigated and discussed. The unconventional fuel cell design is then compared to a traditional design with parallel flow channels in the bipolar plate.

4.1.1 Changes from Previous Model

COMSOL Multiphysics version 3.5 was chosen to model a half cell. Unlike the Fluent software package COMSOL has multiple types of physics built into the software making it easier to couple fluid dynamics to charge transport. Furthermore, the modeling domain is extended to include the membrane, thereby capturing more complex behavior of the fuel cell. Ionic charge transport is modeled in the membrane and electronic charge transport is captured in the GDL. The ohmic losses are captured from the ohmic resistance in the membrane, while the cathode activation losses are captured at the catalyst layer between the membrane and the GDL.

4.2 Modeling Parameter Study (Operating Conditions)

Fuel cell models throughout literature include many modeling parameters that can be altered to change the charge distribution or the trend of results. Some of these quantities, such as the charge transfer coefficient, are derived from theory and are hard to measure. However a small change in this value has a major impact on the electrochemical behavior. Measureable operating conditions such as humidity levels, reactant composition and operating temperature vary throughout numerical studies as well. Min et al. [24] conducted a parameter sensitivity analysis on a fuel cell model, systematically varying 13 parameters over a range of values presented in literature. They found that parameters directly related to the cathode reaction and the cathode kinetics have a high impact on the cell performance, while anode kinetics are not as important. In addition, they found that the conductivity of the membrane phase also had a significant impact on the cell polarization.

In order to choose reasonable modeling parameters for the simulations considered in this chapter, a thorough literature review was conducted to determine what numerical values are commonly assigned to various modeling parameters. The results of this review are shown in Table 7.

Table 7: Modeling Parameter Study

Parameter	Symbol	Range	Reference
Permeability [m^2]	K	1 x 10^{-15} to 1 x 10^{-9}	[63]-[37]
Stoichiometry	ξ	1.5-3	[30]-[35]
Current Density [A/m^2]	i	10,000 – 12,000	[59]-[32]
Pressure [atm]	P	1-3	[32]-[59]
Reference Concentration O_2	$c_{O2,}$ ref	0.85-35.7	[27]-[35]
Porosity	ε	0.3-0.8	[30]-[37]
Temperature [K]	T	343-353	[59]-[31]
Weight Fraction O_2	X_{O_2}	0.178-0.21	[32]-[64]
Weight Fraction H_2O	X_{H_2O}	0-0.5	[27]-[36]
Weight Fraction N_2	X_{N_2}	0.69-0.79	[64]-[27]
Electronic Conductivity [S/m]	σ_e	100-1000	[32]-[36]
Ionic Conductivity [S/m]	σ_i	1-17	[36]-[32]
Cathode charge transfer coefficient	α	0.5-1.15	[30]-[59]
(Specific Surface Area of Catalyst) x (Exchange Current Density) [A/m^3]	ai_{0c}	10-1 x 10^7	[65]-[66]
Cell Voltage [V]	V	0.3-0.7 [V]	[31]-[67]

As presented in Table 7, the permeability values, K, span over a range of six orders of magnitude, 1 x 10^{-15} to 1 x 10^{-9} m^2. For this study, values will range from 1 x 10^{-12} to 1 x 10^{-10} m^2 which were used in the previous study and were found to be a

reasonable range from experimental papers [34, 50]. The air stoichiometry, ξ, varies from 1.5 to 3. In this study, a nominal stoichiometry of 2 will be used unless otherwise stated. The nominal current density at which to run the cell will be 1 A/cm^2. This is a common operating point chosen in literature, and the point chosen for the Fluent study based on the polarization curve. This will help determine the amount of air needed at the inlet to supply the cell with fuel.

The inlet composition of oxygen, water and nitrogen in the air supplied to the cell varies throughout literature [27, 32, 36, 64]. Dry air has an oxygen/nitrogen ratio of about 21/79. Many numerical studies use dry air at the inlet. Other studies use humidified air while retaining a ratio of 21/79 for the weight fraction of the remaining dry air. Still other studies have seemingly random inlet conditions. For this study, dry air will be used. This study considers flow only in the gas phase, in practice using dry air would help prevent water clogging. A range of values (0.85-35.7 mol/m^3) for the reference concentration of oxygen, $c_{,O_2,ref}$, was found throughout literature. While it is unclear where these values come from, a reference concentration for this study will be chosen based on the concentration of oxygen in the air supply using the ideal gas law, given by,

$$c_{O_2} = \frac{X_{O_2} P}{RT}. \tag{4.1}$$

The temperature, T, used throughout literature is almost unanimously 80 degrees Celsius, which will also be used in this study. Porosity, ε, values used throughout literature are generally low values around 0.4. However, research conducted by Gostick

et al. [34] and Williams et al. [53] of actual GDLs shows the actual porosity of GDLs to be much higher (0.6 – 0.88). A porosity of 0.7 will be used in this study.

The electric conductivity of the GDL, σ_e, varies from 100 to 1000 S/m in literature. Simulations were run to study the difference between the final current density over the range of GDL conductivity (100-1000 S/m). The difference was negligible considering the conductivity of the GDL is much higher than the conductivity of the membrane. Since the effect of GDL conductivity was insignificant, a value of 1000 S/m will be used in this study. The ionic conductivity of the membrane, σ_i, varies over a range of 1 to 17 S/m. Based on Min et al.'s work [24], a value of 6 S/m will be used in this study, since it was used as the nominal value in their simulations. The charge transfer coefficient, α, tells the proportion of electrical energy applied that is harnessed in changing the rate of an electrochemical reaction. In literature, the value typically varies between 0.5 and 1. Weber et al. [25] reported that theoretical and experimental slopes of activation overpotentials fit well to a charge transfer coefficient of 1, which will be used in this study. The specific surface area of the catalyst multiplied by the exchange current density, ai_{0c}, describes how fast the oxygen is consumed at the cathode. A higher value means a higher rate of consumption. The value of 120 A/m^3 will be used based on Min et al.'s work [24], where a nominal value of 120 A/m^3 was chosen for simulations. The cell voltage will be 0.6 V in this work. This is a commonly used mid-operation for a steady state cell [39] and matches with the operating point from the polarization curve in Chapter 3. The initial operating conditions and modeling parameters that will be used in this study are given in Table 8.

Table 8: Operating Conditions and Modeling Parameters

Parameter	Symbol	Value
Gas Stoichiometry	ξ	2
Current Density [A/m^2]	i	10,000
Operating Pressure [atm]	P	1
Reference concentration O_2 [mol/m^3]	$c_{O_2,ref}$	6.51
GDL Porosity [-]	ε	0.7
Temperature	T	353
Weight Fraction O_2	x_{O_2}	0.21
Weight Fraction H_2O	x_{H_2O}	0
Weight Fraction N_2	x_{N_2}	0.79
Electronic Conductivity [S/m]	σ_e	1000
Ionic Conductivity [S/m]	σ_i	6
Charge Transfer Coefficient	α	1
(Specific Surface Area of Catalyst) x (Exchange Current Density) [A/m^3]	ai_{0c}	120
Operating Voltage [V]	V	0.6
Cell Height [mm]	h_{cell}	10
Cell Width [mm]	w_{cell}	10
GDL Thickness [mm]	δ_{GDL}	0.4
Catalyst Thickness [mm]	$\delta_{catalyst}$	0.025
Membrane Thickness [mm]	$\delta_{membrane}$	0.1

4.3 Computational Model

In the following section, the computational modeling domain is discussed. Following this, the governing equations, boundary conditions and modeling approach are

related. A mesh convergence study and a validation are presented to test the validity of the mesh and equations.

4.3.1 Modeling Domain

The modeling domain is a half cell model which consists of a membrane, catalyst layer and GDL, where the membrane and GDL interface with the anode and bipolar plate respectively. The modeling domain is shown in Figure 40.

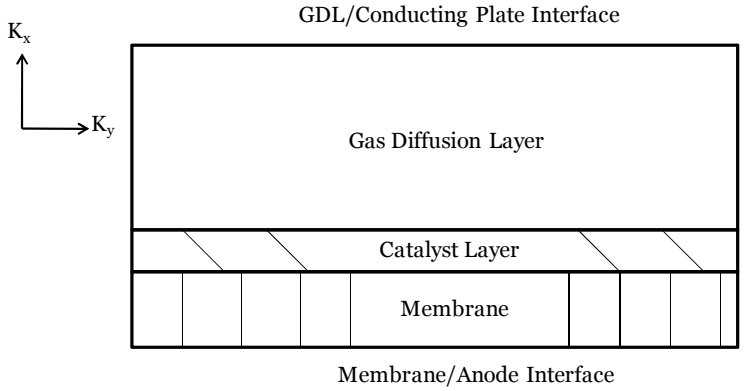

Figure 40: Modeling Domain

The permeability, *K*, changes as a function of position in the x- direction. The inlet and outlet are extended to cover the entire side of a GDL, as illustrated in Figure 41, which helps to eliminate high gradients around corners and spread the distribution more evenly. The addition of the membrane makes it possible for the ohmic losses in the membrane to add to the polarization losses, which are a function of the amount of water in the membrane [24]. Since liquid water transport is not considered in this study, the ohmic resistance will be assumed constant. The primary focus of this study is to understand the permeability of gas flow through the GDL to understand the charge transport through the half cell.

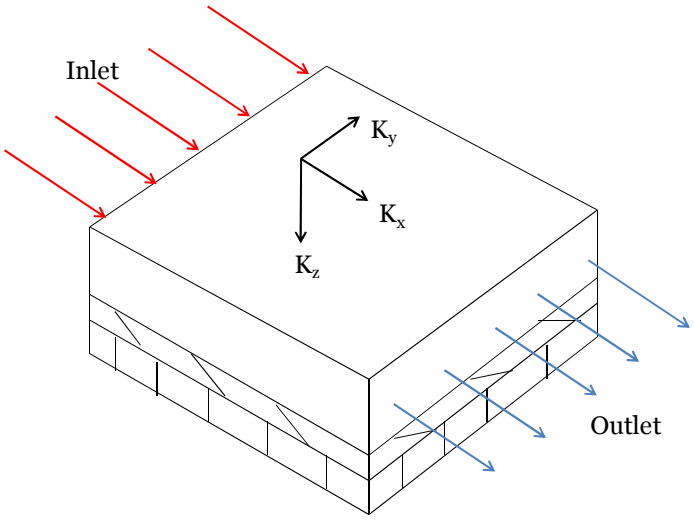

Figure 41: 3-D Modeling Domain with GDL, Catalyst and Membrane

4.3.2 Modeling Assumptions

The modeling assumptions for the simulation include:

- Sufficient cooling is provided to consider the cell isothermal,
- Steady state conditions,
- Ideal gas conditions,
- The flow is laminar and incompressible,
- Water is treated as a single phase in its vapor form, and
- The conductivity in the anode GDL is high enough to cause minimal ohmic losses and the activation overpotential in the anode is much smaller than the activation overpotential in the cathode.

4.3.3 Governing Equations

The governing equations for mass conservation, momentum and species transport and charge transport are presented in the following section.

4.3.3.1 Continuity

The continuity equation given in Equation 3.5 governs mass conservation. The reactions are modeled in the catalyst layer, so the source terms (S_{O_2} and S_{H_2O}), given by Equations 4.2 and 4.3 respectively, are only active in the catalyst layer. In this model, the reaction rate, j_c, is used as a variable to account for the changes in the source terms based on changes in the concentration of oxygen in the air and the potential of the membrane and GDL. Using this instead of the current density allows the source terms in the continuity equation to be calculated directly from Faraday's Law on a volumetric basis. The mass source terms are equal to 0 in the GDL and membrane because the reactions are considered to take place in the catalyst.

$$S_{O_2} = -\frac{M_{O_2} j_c}{4F} \tag{4.2}$$

$$S_{H_2O} = \frac{M_{H_2O} j_c}{2F} \tag{4.3}$$

4.3.3.2 Charge Transport

j_c is a measure of the electrochemical reaction rate and is derived from the Butler-Volmer Equation [31-32, 36, 39, 68], given by,

$$j_c = a i_{0c} \frac{c_{O_2}}{c_{O_2,ref}} \left(\exp\left(\frac{\alpha n F}{RT} \eta \right) - \exp\left(-\frac{\alpha n F}{RT} \eta \right) \right) \tag{4.4}$$

where the overpotential, η, is calculated by the expression,

$$\eta = \phi_e - \phi_i - E_{OCV} \tag{4.5}$$

The Butler-Volmer equation is valid for H_2 transport in a hydrated membrane [69], but has been used throughout literature to characterize dry conditions [30]. While the full form of the Butler-Volmer Expression captures the total cell polarization the Tafel expression has been found to be a good first approximation [28-30, 35, 49] and is given by,

$$j_c = ai_{0c}\frac{c_{o_2}}{c_{o_2,ref}}\exp\left(-\frac{\alpha nF}{RT}\eta\right) \tag{4.6}$$

This study was originally run with the Tafel expression. However, after an analysis into the accuracy of this formulation, it was decided to rerun the study with the full form of the Butler-Volmer Expression. This is discussed in Section 4.3.6. Both ionic and electronic charge transport are considered. Ionic transport is active in the membrane and catalyst layer, while electronic transport is active in the GDL and catalyst layer. Charge transport is described by the conservation of charge equation for ionic transport and electronic transport in Equations 4.7 and 4.8 respectively,

$$\nabla\cdot\left(-\sigma_i\nabla\phi_i\right) = j_c \tag{4.7}$$

$$\nabla\cdot\left(-\sigma_e\nabla\phi_e\right) = -j_c \tag{4.8}$$

4.3.3.3 Mass and Momentum Transport

Darcy's Law, Equation 2.11, is used to describe the relationship between the velocity and the pressure drop in porous media. The species transport equation, Equation 3.9, governs species transport and the Maxwell-Stefan equation, Equation 2.7, governs the gas diffusion in the GDL.

The binary diffusion coefficients are still calculated using Equation 2.9 from kinetic gas theory. In a porous medium, the diffusion is impeded by the pore walls. The Bruggeman correlation, given in Equation 2.8, is used to account for the resistance from the pore walls.

4.3.3 Boundary Conditions

In this section, the boundary conditions are presented.

- *Inlet*

  At the inlet, the velocity is specified according to Equation 4.9 [39, 70-71],

$$v = \xi \frac{i_{avg}}{4F} A_{membrane} \frac{1}{x_{O_2}} \frac{RT}{P} \frac{1}{A_{inlet}} . \tag{4.9}$$

  The mass fractions of oxygen, water and nitrogen in the dry air are specified for the Maxwell-Stefan Equations:

  Mass Fraction of Oxygen: 0.23

  Mass Fraction of Water: 0

  Mass Fraction of Nitrogen: 0.77

  The inlet is set as an insulation boundary for the electronic charge transport.

- *Outlet*

  At the outlet, the pressure is specified at 0 gauge pressure. The outlet is also electrically insulated.

- *GDL/Conducting Plate Interface*

A no-slip condition is set for the momentum transport at the bipolar plate interface. An insulation boundary condition is set for mass transport. To solve for the electronic charge balance, an operating voltage is set at this wall as

$$V_{cell} = 0.6 \text{ V}$$

- *Anode/Membrane Interface*

  The ionic transport is solved in the membrane. The anode voltage is set to 0V.

- *Walls*

  At all the other walls, a no-slip condition is set for momentum transport, an insulation boundary is set for mass transport, and electrical insulation is set for charge transport.

4.3.4 Model Solution

The conservation equations are solved using the PARDISO solver which utilizes a finite element method approach to directly solve the complex system of linear equations in COMSOL version 3.5. An LU-decomposition pre-conditioner is used to solve the non-linear equations iteratively. The Newton-Rhapson method is used to solve close coupled groups, while Gaussian elimination is used to solve the linear system of equations for each iteration [36]. Convergence is reached when the ratio of residuals to the maximum flux across a control surface is below 1×10^{-6}. Figure 42 shows a graphical representation of the solution method.

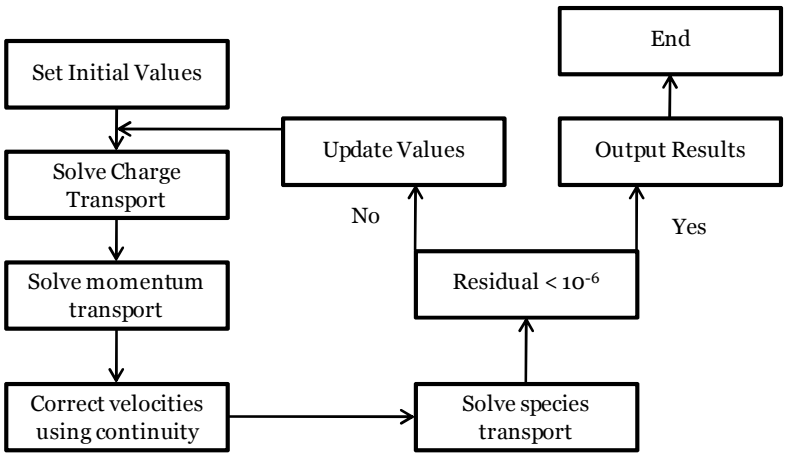

Figure 42: Solution Method adapted from [38]

4.3.5 Grid Independence and Validation

In this section, the results of a grid independence study and a model validation are presented to validate the accuracy of the mesh and model.

4.3.5.1 Grid Independence

The modeling domain is made up of three sudomains; the GDL, catalyst layer and membrane. For the PARDISO solver, a mesh with less than 100,000 degrees of freedom is necessary to avoid non-convergence. Hexadhedral mesh elements with an aspect ratio greater than 0.1 will maintain sufficient solution quality [72]. The aspect ratio is defined as,

$$a_{ratio} = \frac{24\sqrt{3}V}{\sum_{i=1}^{12} h_i^2} \tag{4.10}$$

where h_i are height of the edge elements.

It is desired to have multiple nodes in the through-plane direction in each layer to capture the reactions. However, adding elements in the through-plane direction reduces

the element quality because the aspect ratio will be much smaller than 0.1. Increasing in-plane elements will increase the aspect ratio and element quality because the longer in-plane elements will have lengths comparable to the much shorter through-plane elements (the in-plane direction is geometrically longer and consequently will have larger element lengths). In the following mesh convergence study, the number of elements in the through-plane and in-plane directions was varied to investigate the effect of the aspect ratio and element number on the average current density. Each simulation either had 1, 2, 3 or 4 through-plane elements in each of the three subdomains (i.e., GDL, catalyst and membrane). Three different grid patterns of in-plane meshes were used; 13 x 13, 19 x 19 and 24 x 24. The 24 x 24 mesh was only run with 1 element per subdomain in the through-plane direction, while the 19 x 19 mesh was run with 1, 2 and 3 elements per subdomain, and the 13 x 13 mesh was run with up to 4 elements per subdomain. The in-plane (x- and y-) and through-plane (z-) elements were varied systematically and are shown in Table 9 with the corresponding aspect ratio.

Table 9: Different Mesh Patterns and Corresponding Aspect Ratio

		Number of Through-Plane Elements			
		1	**2**	**3**	**4**
Number of In-Plane Elements	**13 x 13**	0.0597	0.0298	0.0199	0.0149
	19 x 19	0.0871	0.0436	0.0291	-
	24 x 24	0.1099	-	-	-

The only mesh with an aspect ratio over 0.1 is the 24 x 24 x 1 mesh, which contains 60,025 degrees of freedom. Additional through-plane elements for a 24 x 24 in-plane grid resulted in too many degrees of freedom and thus were not considered. The effect of

increasing the number of elements in the in-plane and through-plane on the average current density was of interest. The mesh quality with respect to the average current density for various mesh element configurations that had less than 100,000 degrees of freedom is presented in Figure 43.

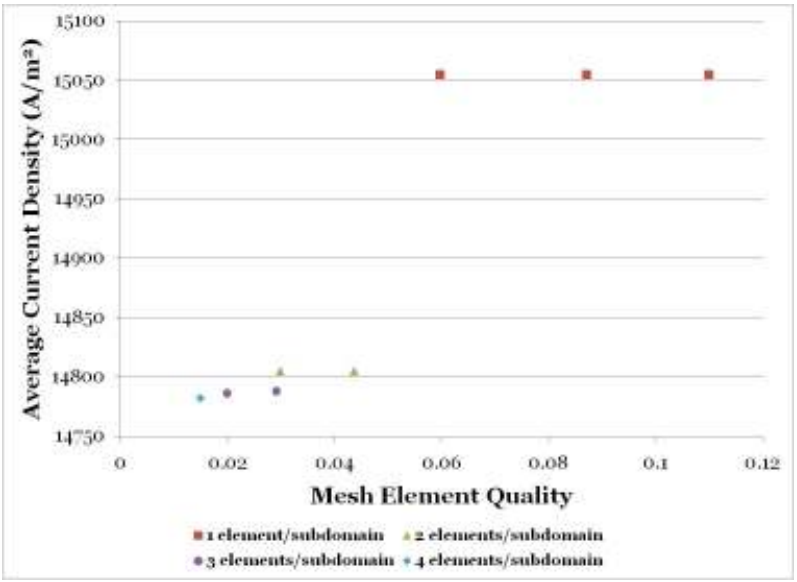

Figure 43: Effect of Changing Number of Elements in the In-Plane and Through-Plane

It can be seen in Figure 43 that the number of elements in the in-plane has no effect on the final average current density since the current densities in a given series are the same, regardless of the number of in-plane elements. However, increasing the number of elements in the through-plane direction causes the average current density to decrease. The change in current density due to increasing the number of through-plane elements is within a 1.6% difference. From this, it can be concluded that 1 element in the through-plane direction is sufficient. While there is virtually no difference between the current densities with different numbers of elements in the in-plane, a mesh of 24 x 24 x

1 will be used to maintain an aspect ratio greater than 0.1. The meshes used from this point forth will be 24 x 24 x 1 with 60,025 degrees of freedom.

4.3.5.2 Validation

A fuel cell model in the COMSOL library was used to validate the model in this study. It was desirable to investigate the effect of using the simplified Tafel expression for the charge transfer current vs. the full Butler-Volmer expression (BV). In addition, the effect of using the half cell model vs. the full cell with the anode was considered. The COMSOL modeling domain contained a single bipolar plate channel with the anode and cathode GDLs and the membrane. The current density at the cathode catalyst layer was plotted for a range of cell operating voltages. The results are shown in Figure 44.

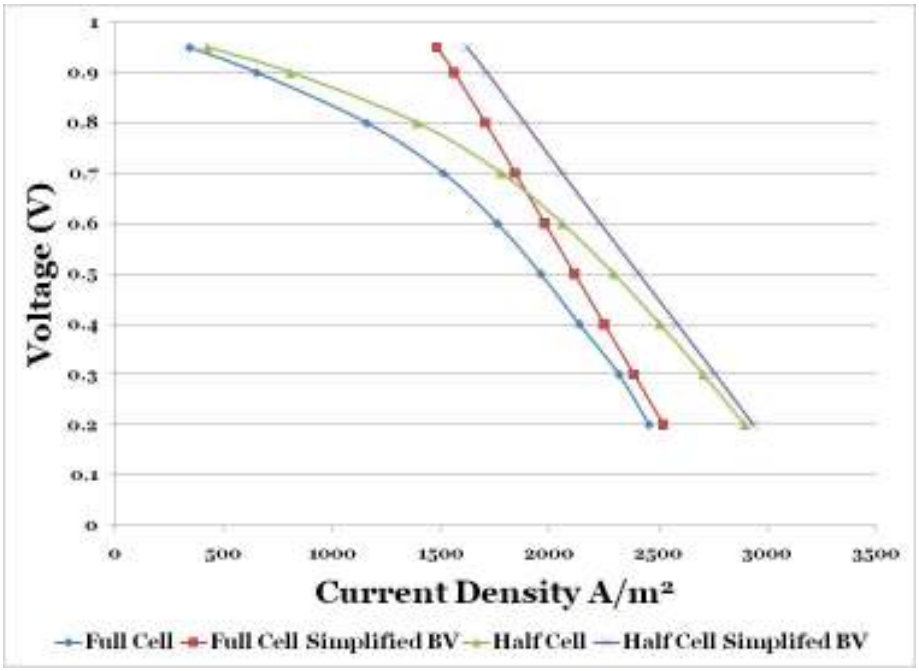

Figure 44: Validation

The first trend that can be seen in the graph is that the Tafel equation does not capture the exponential shape of the activation polarization. The exclusion of this portion

of the irreversible activation loss causes a significant over prediction of the current density by 20% at the operating voltage considered in this study, 0.6 V. It can also be seen that the half cell model also over predicts the current density compared to the full cell model, especially at lower operating voltages. Even at the lowest operating voltage of 0.2 V, the half cell model over predicts the current density by about 15%, although at 0.6 V the over prediction is about 10%. While the over prediction is around 10%, the half cell model with the full Butler-Volmer expression more accurately predicts the behavior of the polarization curve (i.e., voltage vs. current curve).

It can be concluded that using the Tafel expression instead of the Butler-Volmer expression to describe the charge transfer current has a much greater effect on over predicting the current density than using a half cell model as opposed to a full cell model. For the rest of the study, the full Butler-Volmer expression will be used with the half cell model.

4.4 Results

In order to study the effects of the permeability profile with a gradually changing permeability for the unconventional fuel cell design on the current distribution, a systematic study has been conducted. First the permeability profiles used in the simulations are discussed. Next, a study is conducted to understand the effect of the cell changing size. Following this, the effects of changing the permeability profiles, changing the thickness and changing the gas stoichiometry on the current density distribution are discussed. Then, the unconventional GDL is compared to a conventional parallel flow channel. Finally, there is a discussion about tradeoffs between pressure drop and current.

4.4.1 Permeability Profiles

From the previous study, it was learned that due to the high in-plane pressure gradient, there is a need have an in-plane resistance to keep the maximum amount of oxygen-rich air in the fuel cell for reactions to take place. In the present study, three different models of in-plane permeability are considered, and are described by functions based on position. In Section 2.4.1, Chu et al. ran simulations with four models each representing different amounts of water saturation [44]. A model with a linear decreasing porosity profile, a convex parabolic decreasing porosity profile, a concave parabolic decreasing porosity profile and a constant porosity profile were compared, shown in Figure 13 in Section 2.4.1. In this study, a linear decreasing, convex parabolic decreasing and concave parabolic decreasing permeability profile are used. The models were developed by inputting points to describe the desired shape into a Microsoft Excel 2007 spreadsheet and fitting a curve to the points. In each model, the permeability decreases from 1 x 10^{-10} m^2 to 1 x 10^{-12} m^2.

1) Model 1 is a linear decreasing permeability profile described by,

$$K_x = -9.9\times10^{-9}x + 1\times10^{-10} \tag{4.11}$$

2) Model 2 is a convex decreasing permeability profile. Halfway through the GDL in the x-direction (0.005 m), the permeability is at 75% the original value. This profile is described by,

$$K_x = -9.8\times10^{-7}x^2 - 1\times10^{-10}x + 1\times10^{-10} \tag{4.12}$$

3) Model 3 is a concave decreasing permeability profile. Halfway through the GDL in the x-direction (0.005 m), the permeability is at 25% the original value. This profile is described by,

$$K_x = 1.02\times10^{-6}x^2 - 2.01\times10^{-8}x + 1\times10^{-10} \tag{4.13}$$

Model 1, 2 and 3 for the in-plane permeability are shown in Figure 45.

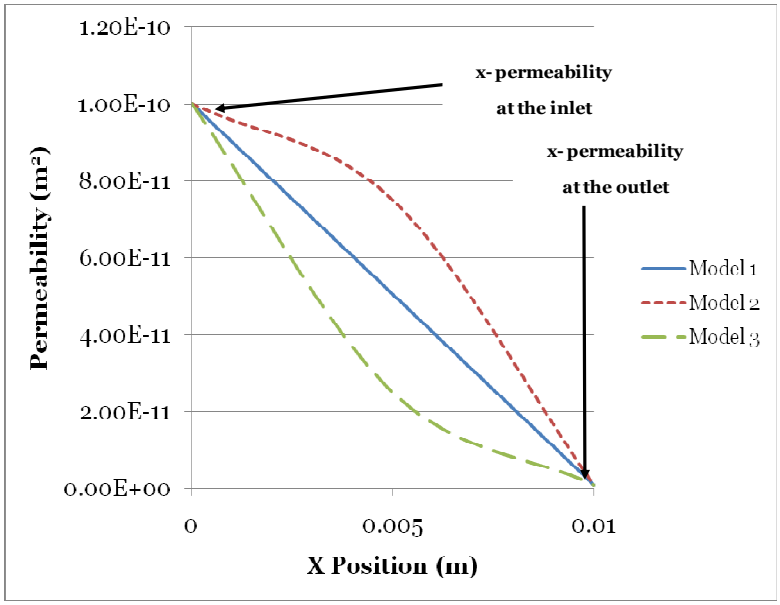

Figure 45: In-Plane x- Permeability Profiles as a Function of x- Position

In the through-plane direction, it is desirable to inhibit the air from reaching the catalyst near the inlet because the air is oxygen rich. Near the outlet it is desirable for the air to move forward to the catalyst layer rather than exit the cell through the outlet. In this study, three different models of through-plane permeability with an increasing permeability are considered. The models are developed by fitting a polynomial to points which make up the desired shape. In each model, the permeability increases from 1 x 10^{-12} m^2 to 1 x 10^{-10} m^2.

A) Model A is a linear increasing permeability profile described by,

$$K_z = 9.9\times10^{-9}x + 1\times10^{-12} \tag{4.14}$$

B) Model B is a convex increasing permeability profile. Halfway through the GDL in the x-direction (0.005 m), the z- permeability is at 75% the final value. This profile is described by,

$$K_z = -9.8\times10^{-7}x^2 + 1.97\times10^{-8}x + 1\times10^{-12} \tag{4.15}$$

C) Model C is a concave increasing permeability profile. Halfway through the GDL in the x-direction (0.005 m), the z- permeability is at 25% the final value. This profile is described by,

$$K_z = 1.02\times10^{-6}x^2 - 3\times10^{-10}x + 1\times10^{-12} \tag{4.16}$$

Model A,B and C for the through-plane permeability are shown in Figure 46.

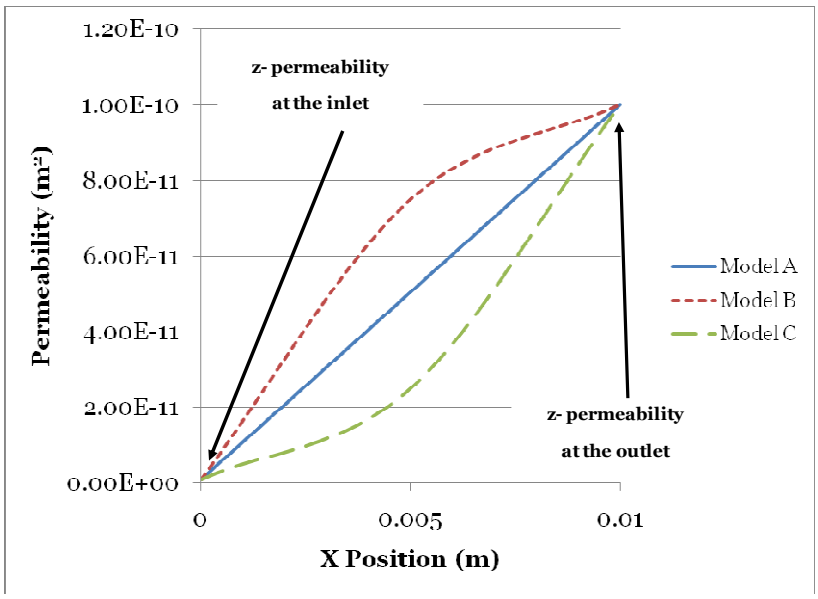

Figure 46: Through-Plane z- Permeability as a Function of x- Position

Since there is no flow in the y-direction, it is assumed the permeability in the y-direction will not affect the results. The y-permeability is given the value of 5×10^{-11} m^2, which is between the lowest and highest permeability considered.

4.4.2 Scaling of the Cell

Originally, the simulations were going to be run with a 4 cm x 4 cm cell, which is close to the size of a medium sized fuel cell. Numerically, this was a relatively large cell size causing the distance between the mesh nodes to produce an erroneous numerical effect along the lines in the grid pattern.

As such, the size of the cell was reduced until the nodes were close enough that the numerical effect was insignificant, which was determined to be a 1 cm x 1 cm cell. It is still desirable to know if the results change significantly when the size of the cell increases or decreases. The results of a 1 cm cell are compared to a 0.5 cm cell and a 1.25 cm cell. In cells larger than 1.25 cm, the ribbing effect is very noticeable, so no simulations were conducted for a larger cell. Each simulation was run with the same permeability profile, linear decreasing for the in-plane permeability, Model 1, and linear increasing for the through-plane permeability, Model A. The effect of changing the size on the average current density is shown in Figure 47. It can be seen from Figure 47 that the average current density is very close regardless of the size of the cell. The uniformity can be investigated by looking at the ratio of standard deviation of current density/average current density, which is shown in Table 10. The ratio in each case is small, showing that the uniformity is good and independent of the size of the cell. From this, it can be concluded that the current density distribution scales well when the size of the cell changes.

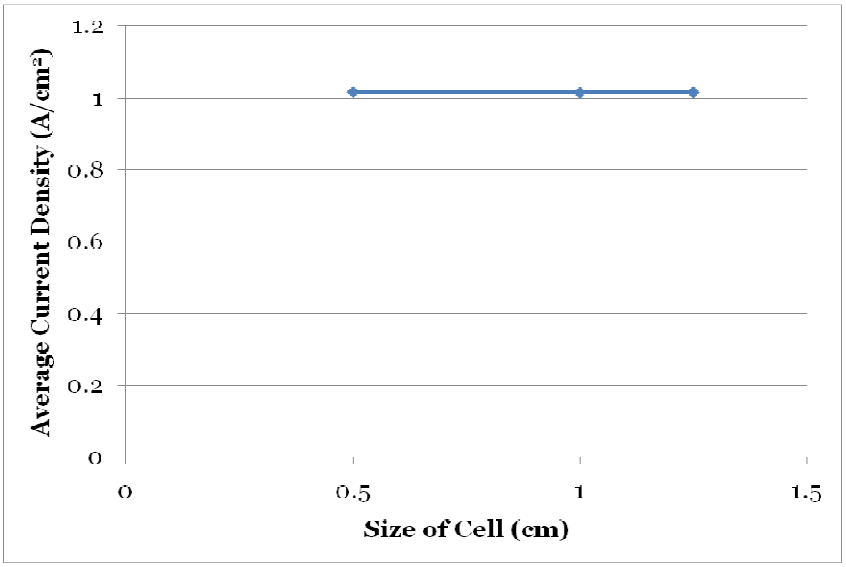

Figure 47: Effect of Changing the Size of the Cell on the Average Current Density

Table 10: Ratio of Standard Deviation of Current Density/Average Current Density at Different Cell Sizes

Size	Ratio
0.5 cm	0.045
1 cm	0.047
1.25 cm	0.047

4.4.3 Effect of Changing Permeability Profiles

To study the effect of changing the in-plane and through-plane permeability profile, each in-plane profile was run with each through-plane profile for a total of 9 simulations, employing a partial factorial design of experiments. A diagram of the simulations is shown in Table 11. The effect of the different permeability profiles on the current density can be seen in Table 12. The numbers 1, 2, and 3 refer to different in-

plane permeability profiles, where as the letters A, B, and C refer to different through-plane permeability profiles.

Table 11: Design of Experiments for Simulations

In-Plane All Decreasing	Through-Plane All Increasing
Model 1	Model A
	Model B
	Model C
Model 2	Model A
	Model B
	Model C
Model 3	Model A
	Model B
	Model C

Table 12: Effect of Graduating Permeability with Unconventional GDL

Simulation	Average Current Density (A/cm^2)	Standard Deviation of Current Density (A/cm^2)	Ratio Standard Deviation/ Average Current Density
1A	1.015	0.048	0.047
1B	1.015	0.048	0.047
1C	1.015	0.048	0.047
2A	1.016	0.049	0.048
2B	1.016	0.049	0.048
2C	1.016	0.049	0.047
3A	1.018	0.047	0.047
3B	1.018	0.047	0.047
3C	1.018	0.047	0.047

The first conclusion that can be drawn is that the through-plane permeability profile has no effect on the final current density. When the in-plane permeability is held constant and the through-plane permeability is changed, there is no difference in the results. The through-plane direction is very thin compared to the length of the in-plane direction. Since the gas only has to travel a short distance, the permeability does not affect the distribution noticeably. This is consistent with the results of Pharaoh et al. [42] who showed that through-plane permeability has less of an impact than the in-plane permeability.

The next conclusion that can be drawn is that the lower the in-plane permeability, the higher the average current density. Model 3 has the lowest in-plane permeability and has the highest current density. However, the difference in average current density and uniformity between the different in-plane permeability profiles is less than 0.3%, which is an insignificant change.

Four cases with constant permeability were run to compare the permeability profiles that change with position to isotropic permeability profiles. Values were chose at the lowest permeability used in the study, 1 x 10^{-12} m^2, the highest permeability 1 x 10^{-10} m^2, and two intermediate points. The results are shown in Table 13.

Table 13: Current Density with GDLs of Varying Isotropic Permeability

Simulation [m^2]	Average Current Density (A/cm^2)	Standard Deviation of Current Density (A/cm^2)	Ratio Standard Deviation/Average Current Density
1 x 10^{-12}	1.040	.034	0.033
2 x 10^{-12}	1.028	.041	0.040
5 x 10^{-11}	1.012	.050	0.050
1 x 10^{-10}	1.012	.051	0.050

The simulation with the lowest isotropic permeability, 1 x 10^{-12}, produces a current density 2.7% higher than the case with a permeability of 1 x 10^{-10}. Thus, two orders of magnitude difference in permeability changes the current density by a very small amount. Although it was hypothesized that the models with lower in-plane permeability would exhibit higher current densities because the air would move towards the catalyst layer rather than out of the cell, these results show that permeability has relatively no impact.

4.4.4 Effect of GDL Thickness

The effect of the thickness of the GDL on the average current density was studied by running Model 1A with three different GDL thicknesses, 350, 400 and 450 µm. Model 1A was chosen because both the in-plane and through-plane profiles are linear instead of parabolic, making it easier for the solver to converge. The GDL thickness is plotted against the average current density in Figure 48.

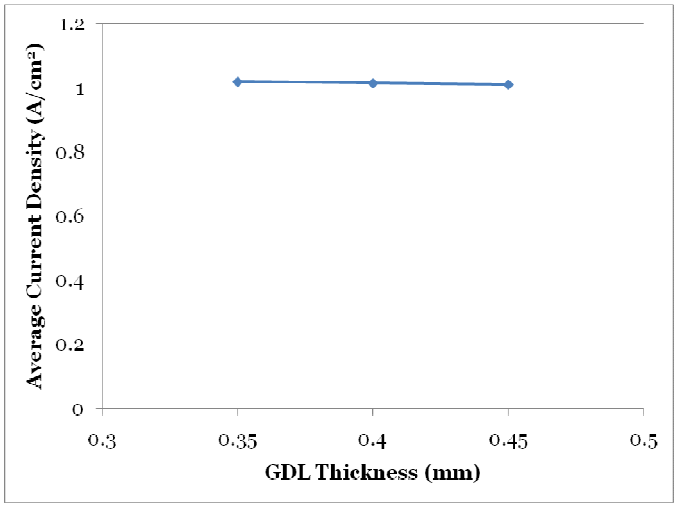

Figure 48: Effect of GDL Thickness on Average Current Density

As the thickness of the GDL decreases, the average current density increases, although insignificantly. The difference between a 450 micron GDL and a 350 micron GDL is less than 1%. With a thinner GDL, the air is closer to the catalyst sites and there is a higher concentration gradient causing more diffusion into the catalyst layer. The ratio of standard deviation of current density to average current density is shown in Table 14.

Table 14: Current Density at Varying GDL Thickness

Thickness [mm]	Average Current Density (A/cm^2)	Standard Deviation of Current Density (A/cm^2)	Ratio Standard Deviation/Average Current Density
0.350	1.019	0.048	0.047
0.400	1.015	0.048	0.047
0.450	1.010	0.048	0.048

The ratio confirms that the uniformity of current density across the cell is independent of thickness. This is the same trend seen in the Fluent study discussed Chapter 3.

4.4.5 Effect of Gas Stoichiometry

The effect of increasing the gas stoichiometry on the current density is investigated using Model 1A for four different gas stoichiometries. The gas stoichiometry vs. the average current density is shown in Figure 49.

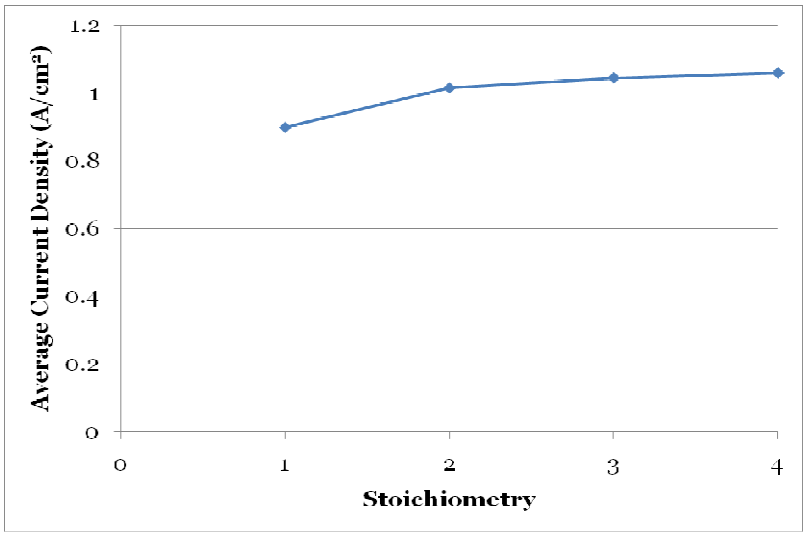

Figure 49: Stoichiometry vs. Average Current Density

At a stoichiometry of 1, the oxygen is depleted from the air near the inlet, and there is not enough oxygen to sustain a higher current density near the outlet. This results in a 12% difference in current density between a stoichiometry of 1 and 2. As the stoichiometry of air increases, there is an increase in the average current density. Between a stoichiometry of 2 and 4, there is only a 4.2% increase in the average current density. Yuan et al. [71] saw an increase in the stoichiometric ratio helped cell performance at high current densities, but had little effect at low current densities. They employed a two-phase model and hypothesized increased air flow rate helped remove liquid water from the GDL. Hung et al. [70] came to a similar conclusion, showing a 20% decrease in the air stoichiometry only had a 1.7% decrease in the average current density. At lower current densities where there is no liquid water, the air stoichiometry does not affect the final current density as long as there is enough air to sustain the reaction. The uniformity of the current density is considered in Table 15.

Table 15: Current Density at Different Air Stoichiometries

Stoichiometry	Average Current Density (A/cm^2)	Standard Deviation of Current Density (A/cm^2)	Ratio Standard Deviation/Average Current Density
1	0.900	0.133	0.148
2	1.015	0.048	0.048
3	1.045	0.030	0.029
4	1.059	0.023	0.021

As the air stoichiometry increases, the ratio is lower revealing the uniformity is better. In the case with a stoichiometry of 1, the ratio was 0.148, which is 3-5 times higher than the ratio at higher stoichiometries. Between a stochiometry of 2 and 3, the average current density only increases by 3%, while the ratio drops by 40%. From a stoichiometry of 3 to 4, there is a 1.3% increase in current density with a 27% drop in the ratio. This is further evidence that as the stoichiometry increases, its effect on the current density decreases.

4.4.6 Comparison to Parallel and Serpentine Flow Field

In order to quantify the benefits of the unconventional GDL with a side inlet, it was necessary to compare to a conventional fuel cell of the same size. The unconventional GDL was compared to a state-of-the-art fuel cell with a *parallel flow field* in the bipolar plate. The parallel flow field is shown in Figure 50. The permeability profile used in the unconventional GDL was Model 1A, while the permeability for the state-of-the-art GDL was set to an isotropic permeability of 5×10^{-12} m^2. The operating

parameters and inlet conditions were the same as in Table 8, with the exception of air stoichiometry, which was set to 4. The results are shown in Table 16, and the current density distribution on the GDL/catalyst layer interface for the unconventional model and the parallel flow field model are shown in Figure 51 (a) and (b) respectively.

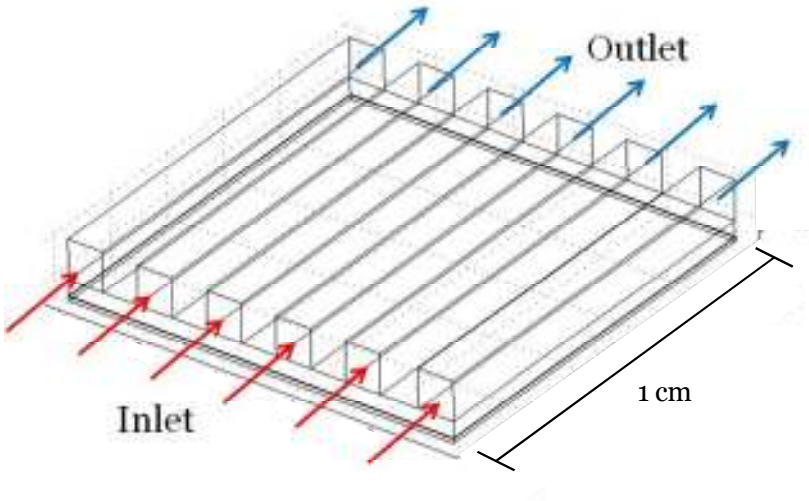

Figure 50: Parallel Flow Field

Table 16: Current Density Comparing the Unconventional Model with Graduated Permeability to a State-of-the-Art Parallel Channel Model

Simulation	Average Current Density (A/cm^2)	Standard Deviation of Current Density (A/cm^2)	Ratio Standard Dev: Average
Unconventional Model	1.059	0.023	0.021
State-of-the-Art Parallel Channel	0.462	0.328	0.709

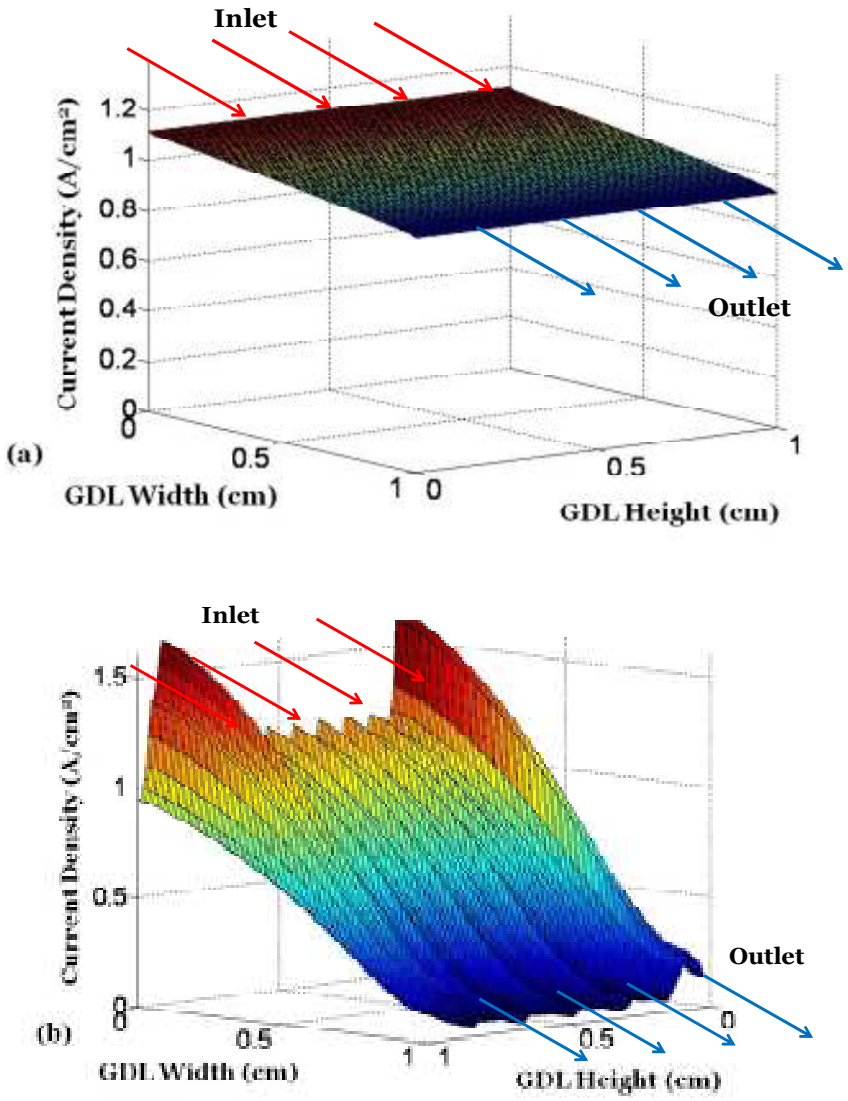

Figure 51: Current Density Profile for (a) Unconventional GDL and (b) Parallel Flow Field

The unconventional GDL design (which has a graduated permeability) performed better than the parallel flow channel in every metric. The average current density in the parallel channel design was 56% lower than the unconventional GDL design, and the ratio of the standard deviation to the average current density was 97% lower for the unconventional GDL, which can be seen when comparing Figure 51 (a) and (b). This suggests that an unconventional GDL with a side inlet and a graduated GDL drastically increases the performance by forcing the air through the GDL. In the parallel flow field,

the oxygen is transported to the catalyst through diffusion, and most of the oxygen rich air leaves the system through the outlet channels before it reaches the catalyst. Low current densities near the outlet for the parallel flow field in Figure 51 (b) show that there was little oxygen present for the electrochemical reactions.

The range of the current density distributions of the graduated GDL were then compared to *serpentine flow fields*, based on three existing studies. Only the range is reported because the standard deviation of current density could not be calculated from the information given in the literature. The results of this study are shown in Table 17.

Table 17: Comparison of Range of Current Density Distribution

Simulation	Current Density Distribution (A/cm^2)	Average Current Density (A/cm^2)
Unconventional (graduated) GDL	1.12-0.93	1.02
Zhang et al. [39]	1.2-0.5	0.75
Shimaplee et al. [37]	1.33-0.85	1.14
Al-Baghdadi [32]	1.35-0.7	N/A

The graduated GDL shows the highest uniformity. The difference in current density distribution is 0.7 A/cm^2 for Zhang et al., 0.5 A/cm^2 for Shimaplee et al., and 0.65 A/cm^2 for Al-Baghdadi et al, while the difference in the graduated GDL is approximately 0.2 A/cm^2. This suggests that the unconventional design may exhibit higher uniformity. It is important to note that the operating voltages for the simulations were not the same, but they ranged from 0.6 to 0.7 V.

Interdigitated flow fields have been shown to provide a more uniform current distribution with the forced convection through the GDL. This suggests that the

graduated GDL has promise in producing a more uniform current density than conventional flow channels, as the graduated GDL shares the advantage of forcing flow into the GDL with interdigitated flow fields.

4.4.7 Tradeoff with Pressure Drop

After investigating the effect of different permeability profiles, changing thickness and changing gas stoichiometry, it can be concluded that the current density and uniformity will remain nearly the same regardless of the changing conditions, as long as the cell is provided with enough fuel to operate. This can be explained by the velocity boundary condition. At the inlet, a velocity is prescribed which prescribes a mass flow rate of air at the inlet. Regardless of the fluid resistance, the model will provide the prescribed amount of air to the cell. According to Darcy's Law, setting the permeability and velocity will increase the pressure gradient. The effect of changing the permeability profile on the pressure drop across the cell is shown in Table 4.18.

It is shown that as in-plane resistance increases, pressure drop will increase. Of the graduated models, the concave parabolic model (Model 3) has the lowest in-plane permeability and highest in-plane resistance. This model has the highest pressure drop of the graduated models.

Table 18: Effect of Permeability Profile on Pressure Drop

	Simulation	Pressure Drop (Pa)	Average Current Density (A/cm^2)
Anisotropic (Graduated Models)	**1A**	1800	1.015
	1B	1800	1.015
	1C	1800	1.015
	2A	1100	1.016
	2B	1100	1.016
	2C	1100	1.016
	3A	6400	1.018
	3B	6400	1.018
	3C	6400	1.018
Isotropic	**1.00E-12**	42,800	1.040
	2.00E-12	20,000	1.028
	5.00E-11	800	1.012
	1.00E-10	400	1.012

The highest pressure drop, 42,800 Pa, corresponds to the simulation with the highest current density (1.04 A/cm^2) and lowest permeability, (1 x 10^{-12} m^2). The simulation with the lowest pressure drop, 400 Pa, is the cell with the highest permeability (1 x 10^{-10} m^2) which also corresponds to the lowest current density (1.012 A/cm^2). A decrease of 2.7% in current density corresponds to a 99% decrease in pressure drop between the case with the highest and lowest current density. The pressure drop of the graduated models is compared to pressure drops of some common gas diffusion layer designs taken from literature in Table 19.

Table 19: Effect of Flow Field Design on Pressure Drop

Simulation	Type of Flow Field	Pressure Drop	Distance over Drop (cm)
Pharoah [42]	Serpentine	0-125	4-8
Yi and Nguyen [30]	Interdigitated	3000	0.3
Yi and Nguyen Scaled	Interdigitated	10,000	1
Model 1	Graduated	1800	1
Model 2	Graduated	1100	1
Model 3	Graduated	6400	1

The serpentine flow field exhibits the smallest pressure drop. This is because the air is not forced into the GDL. There is only diffusion through the GDL so the drop is through the length of the channel. Yi and Nguyen reported a pressure drop of 3000 Pa in a 0.3 cm long channel. Darcy's Law was used to scale this result to the 1 cm long GDL in the unconventional design with the graduated GDL. Darcy's Law states that the pressure drop is directly related to the distance over the drop. Therefore, if the distance increases, the pressure drop must increase by the same factor. In the interdigitated flow field and the graduated GDL, the pressure drops are much higher because the gas is forced into the GDL. The graduated GDL showed a lower pressure drop than the interdigitated when the distance of the pressure drop is considered, but both models were much higher than the serpentine design.

4.5 Conclusions

In practice, a fuel cell would be provided with fuel using a device which regulates flow, such as a mass flow controller, to provide enough fuel for the cell under different loading conditions. These devices also regulate the pressure at the inlet to prescribe a

flow rate regardless of the resistance to flow. If the pressure is set as a constant at the inlet, and the permeability of the GDL is changed, the velocity through the GDL will follow the path of least resistance. However, in a real world system with flow controllers, the pressure would be regulated to overcome the resistance.

This study shows that as long as the cell has enough fuel to run, the permeability will not affect the final current density or the uniformity of the current density for the graduated GDL design. The trade-off is an increased pressure and parasitic power loss to push the gas through the small inlet and into the porous GDL.

In the parameter sensitivity study by Min et al. [24], the permeability was varied over 7 orders of magnitude. The pressure drop across the flow channels was not reported, and they did not use a cell with forced convection as the dominant transport mechanism. They found that the permeability had almost no influence on the average current density, which is consistent with the results of this study.

The previous two numerical studies addressed graduating the permeability in GDLs, but they were numerical studies where the permeability can be adjusted to the desired values. In order to manufacture an anisotropic GDL with the desired permeability characteristics, the structure of the GDL must be designed to control the flow of the reactant gases. In the following chapter, woven GDLs are manufactured in-house using a hand loom in an attempt to characterize the relationship between the structure of a GDL and its in-plane and through-plane permeability.

CHAPTER 5

EXPERIMENTAL PERMEABILITY TESTING

5.1 Introduction and Motivation

In chapters 3 and 4, computational models were developed to investigate the effect of graduating the permeability profile on the current density distribution in the cell. While the models looked at theoretical permeability profiles, there was no discussion as to how a graduated GDL would be manufactured.

The permeability of a porous structure is dependent on the pore structure and overall porosity. In this chapter, GDLs with anisotropic permeability profiles are woven using a hand loom. The in-plane permeability and through-plane permeability are tested using a permeability testing device made in-house, and the permeability is characterized for two different weave types. In addition to weave type, the tightness of the fibers in the weave is varied to create different pore structures, which will results in different permeability. The purpose of this study is to characterize the in-plane and through-plane permeability based on weave type and tightness.

5.2 Methodology

In this section, the experimental test set-up for the in-plane and through-plane tests and the experimental test method for each set-up along with the materials used for verification and testing are discussed.

5.2.1 Through-Plane Permeability Test Set-up

The through-plane permeability was measured using the test set-up shown in Figure 52 (a) and (b). In this arrangement, air was supplied from a compressor at 100 psi gauge. A pneumatic regulator with a 15 micron filter removed water and particulates from the incoming air stream and reduces the pressure to 40 psi gauge. Using a mass flow controller (Alicat 0-2 SLPM, accuracy ± 0.4% reading ± 0.2% full scale), the mass flow rate into the device was adjusted. The samples were clamped between two aluminum plates with a 1cm x 1cm channel cut in the center of the plates to allow air to pass through the sample. A mixture of soap and water was applied to the outsides of the device to insure a gas tight seal, which was possible without further sealing due to the low pressures involved. A differential pressure sensor (Omega PX653, accuracy ± 0.1% full scale) spanning a range of -0.05 to 0.05 in. of water column corresponds to -12.5 to 12.5 Pa. The local barometric pressure was taken from the mass flow controller and was assumed to be the outlet pressure in the calculations. At least ten pressure measurements were taken for each sample, corresponding to ten flow rates. Four different samples for each weave design were measured.

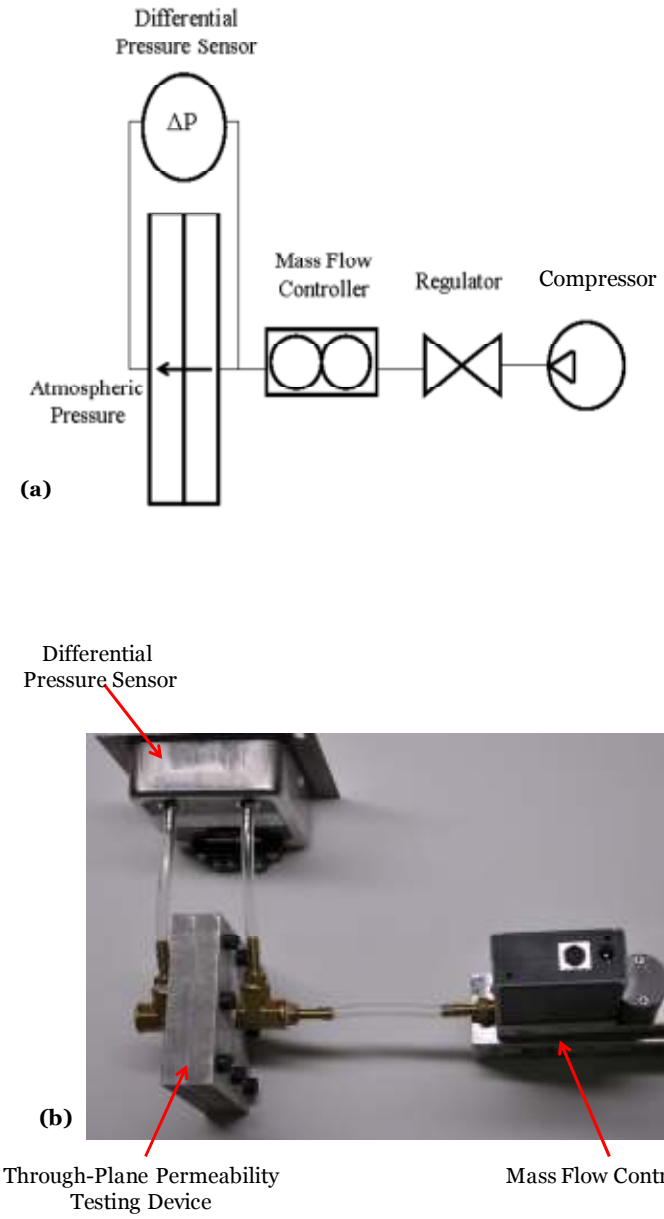

Figure 52: (a) Through-Plane Permeability Set-up and (b) Close up of the Device with Mass Flow Controller and Differential Pressure Sensor

5.2.2 In-Plane Permeability Test Set-up

The in-plane permeability was measured using the set-up shown in Figure 53 (a) and (b). Like the through-plane set up, a compressor provided air to a pneumatic regulator which reduced the pressure from 100 psi gauge to 40 psi gauge and filtered out water and particulates in the air. The flow rate was set on the mass flow controller to

supply the air to the inlet channel of the permeability testing device. Rubber gaskets sealed the gaps between the top and bottom of the test rig, and plumbers putty was used to seal the back of the channels, as seen in Figure 53 (b). The top and bottom of the test rig were compressed onto steel feeler gauges of a known thickness to determine the compressed thickness of the sample. After the air entered the inlet channel, it flowed through the 1.5cm x 1.5 cm samples, which were compressed between the top and bottom of the test rig, in the in-plane direction. The inlet pressure was extracted from the mass flow controller, and the outlet pressure was assumed to be atmospheric pressure. At least ten measurements were taken for each sample. Calibration tests were run without a sample to ensure the pressure drop in the channel and between the plates was negligible. In addition, the system was pressurized at 40 psi gauge before each test to ensure the system was free of leaks. In-plane permeability data was obtained for three levels of compression for each sample.

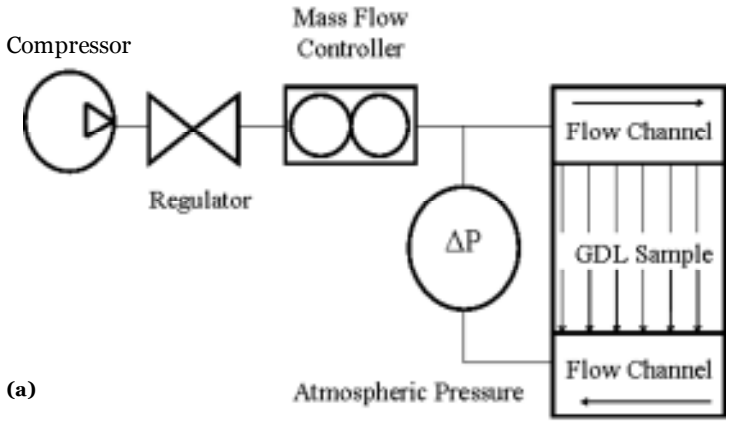

(b)

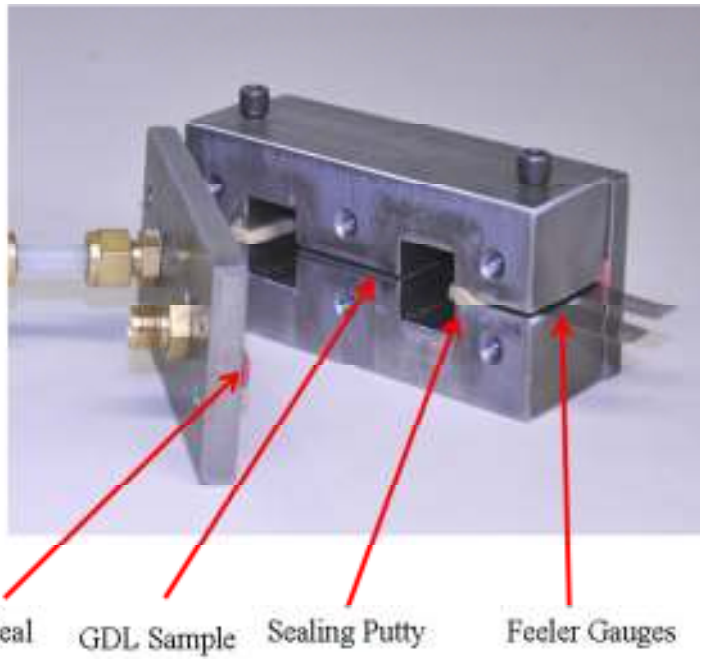

Figure 53: (a) In-Plane Permeability Test Set-up and (b) In-Plane Permeability Test Device

5.2.3 Hand Loom

The woven carbon fibers structures tested in this study were made in-house on a 16" Ashford 8 Harness hand loom, which is shown in Figure 54. The warp fibers were fixed onto a ruler with tape at the desired spacing corresponding to the desired tightness. The weft fibers were inserted between the warp fibers and perpendicular to the length of the warp fibers. After each weft fiber was inserted between the warp fibers, the beater was used to push the weft fiber into the pattern. After two weft fibers were added to the pattern, a ruler was used to ensure the desired tightness was achieved.

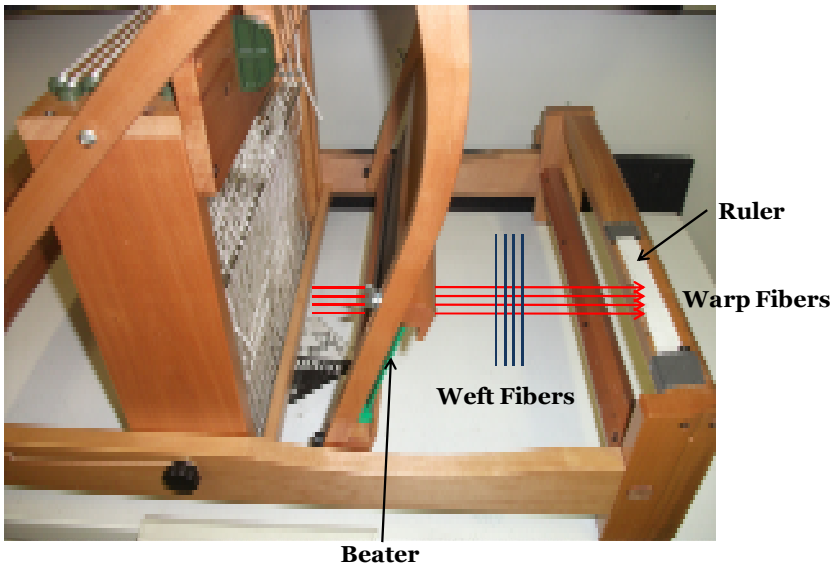

Figure 54: Hand Loom Used to Weave the Woven GDLs

5.2.4 Materials

To determine the accuracy of the through-plane and in-plane test equipment, a non-woven carbon paper, SGL 34BA made by SGL Technologies GmbH, was used to compare the experimental permeability results to those found in literature. The original thickness of the SGL 34BA was 285 microns, which was provided by the manufacturer and verified with a Mitutoyo micrometer (± 0.01 mm). The woven samples were made from T-300 carbon fibers provided by Cytec Inc. Each carbon fiber tow was comprised of 3000 carbon fibers.

5.3 Analysis

In the following section the approach used to analyze the permeability and compressed porosity of the samples are discussed. From this analysis, the through-plane and in-plane permeability profiles for woven samples of different tightness can be classified.

5.3.1 Darcy-Forchheimer Formulation: Permeability

The Darcy-Forchheimer equation, which was discussed in Section 2.3, describes the relationship of pressure drop and velocity through a porous medium. Using this relationship, given in Equation 2.10, the permeability of gas (air) through the samples can be obtained. The velocity of the gas flowing through the pores is given by Equation 5.1, which holds for 1-D flow of compressed air. Air is compressible and if one-dimensional flow is assumed, this is a reasonable assumption given the uni-directional pressure gradient in the test set-ups.

$$v = \frac{\dot{m}}{\rho A_{perpendicular}} = \frac{m'}{\rho} \tag{5.1}$$

where $\dot{m}$ is the mass flow rate, $A_{perpendicular}$ is the area of the GDL perpendicular to the flow and m' is the mass flux. Assuming the air is an ideal gas, which is a reasonable assumption at standard conditions, the density (ρ) can be represented by,

$$\rho = \frac{PM}{RT}. \tag{5.2}$$

If Equation 5.2 is substituted back into Equation 5.1, the velocity can be represented by,

$$v = \frac{RT}{PM} m'. \tag{5.3}$$

Substituting Equation 5.3 back into Equation 2.10 (the original Darcy-Forchheimer equation) and simplifying gives,

$$-\nabla P = -\frac{\delta P}{\delta x} = \frac{\mu}{K}\frac{RT}{PM} m' + \beta \frac{RT}{PM} m'^2. \tag{5.4}$$

Separating variables and integrating, Equation 5.4 becomes,

$$\frac{P_{in}^2 - P_{out}^2}{2LRT} M = \frac{\mu}{K} m' + \beta m'^2 \tag{5.5}$$

where L is the length the gas travels through the sample.

In order to obtain the permeability term, the mass flow rate is increased over 10-15 data points within a range of 0.001 standard liters per minute (SLPM) to 2 SLPM, and the corresponding pressure drop across the sample is recorded. Increasing the mass flow rate increases the mass flux, which can be calculated based on the cross sectional area perpendicular to the flow. The inlet pressure was measured using the mass flow controller based on the pressure drop between the inlet and outlet. Then, the mass flux was plotted against the pressure term on the left hand side of Equation 5.5, which was used to generate a plot similar to Figure 55. A 2nd order polynomial was fit to the data, which was compared to Equation 5.5. Assuming a constant gas viscosity of 1.85 x 10^{-5} Pa-s [73], the permeability can be calculated from the linear term in the polynomial fit from the graph.

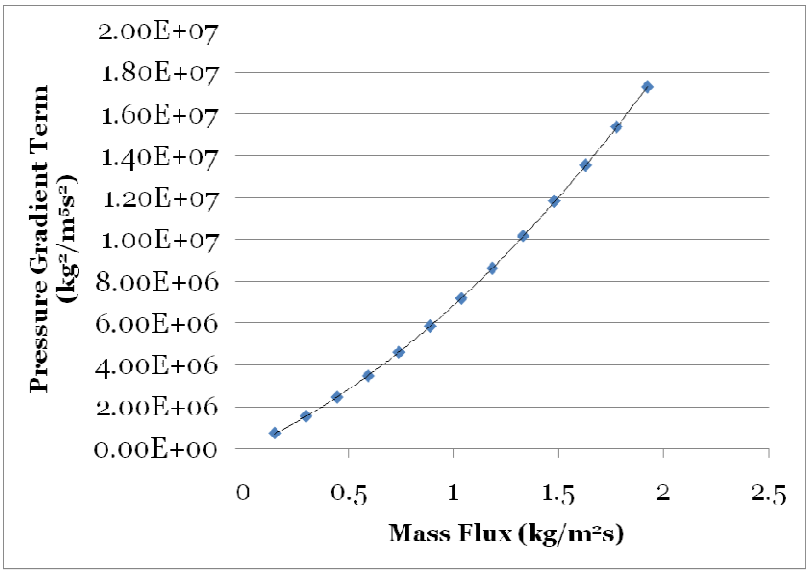

Figure 55: Representative Plot for Permeability Test

5.3.2 Calculation of Uncompressed Porosity for In-Plane Tests

A relationship between permeability and porosity is desired to determine the in-plane permeability of an uncompressed GDL. In order to relate permeability to porosity, the porosity needs to be related to the bulk volume while the sample is compressed to a known thickness because the volume during compression can be measured. It is assumed the compression is one-dimensional. To this end, the in-plane permeability of the samples was tested under three levels of compression which was dictated by compressing the sample down to steel feeler gauges of known thickness. The pressure gradient term was plotted against the mass flux for each sample at each level of compression, as seen in Figure 56 for a twill 8x4 weave. A least-squares fit was used to match an equation to each data set. The equation is fit to the Darcy-Forchheimer equation using the analysis in Section 5.3.1 to calculate the permeability at each level of compression.

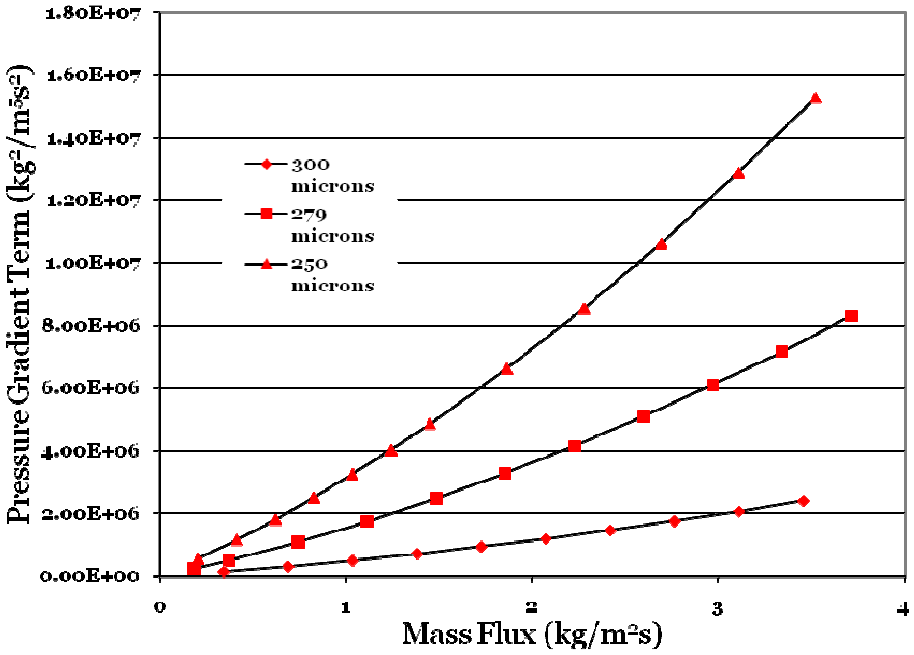

Figure 56: Mass Flux vs. Pressure Gradient Term for Twill 8x4 at 3 Levels of Compression

It is assumed that the fibers are incompressible, that is all the reduction in volume is due to a reduction in the open space between the fiber [34]. Under these assumptions, the compressed thickness can be determined by Equation 5.6 [34].

$$V_{p,C} = V_{b,C} - V_s = V_{b,C} - (1-\varepsilon_0)V_{b,0} \tag{5.6}$$

where $V_{p,C}$ is the compressed pore volume, $V_{b,C}$ is the compressed volume of the bulk volume of the sample, V_s is the volume of the solid, ε_0 is the original porosity and $V_{b,0}$ is the original bulk volume of the sample. Rearranging Equation 5.6, the porosity of the compressed sample is given by,

$$\varepsilon_C = \frac{V_{p,C}}{V_{b,C}} = 1 - \frac{1-\varepsilon_0}{V_{b,C}/V_{b,0}} \tag{5.7}$$

where ε_C is the compressed porosity. After calculating the compressed porosity, the porosity can be compared to the permeability at different levels of compression. An exponential equation is fit to the plot of permeability vs. porosity, as seen in Figure 57, which gives the permeability as a function of porosity at each level of compression. Using this equation and the uncompressed porosity, the uncompressed in-plane permeability can be determined in both in-plane directions.

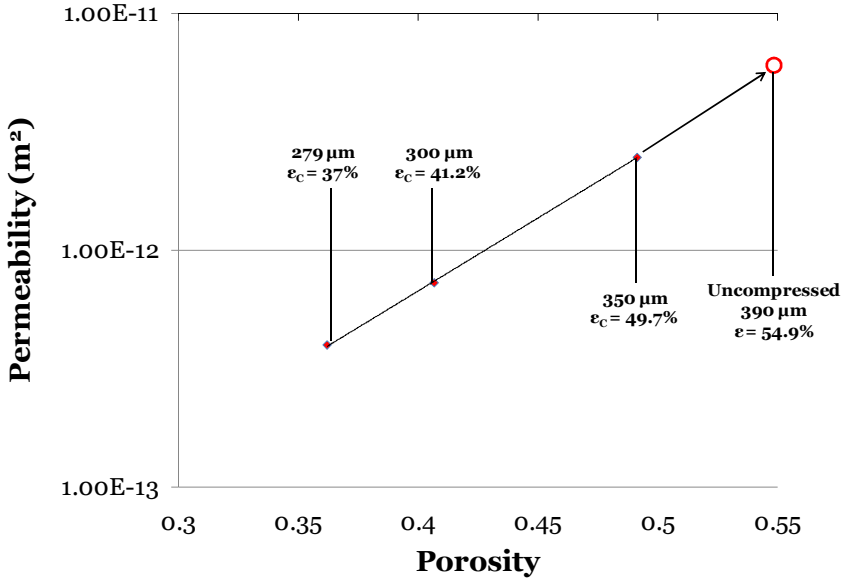

Figure 57: Permeability vs. Porosity for a Twill 8x8 Weave

5.4 Design of Experiments

Samples of two different types of weaves (i.e., plain and twill) at three different tightnesses (i.e., 8x8, 8x6, and 8x4) were manufactured using a hand loom. In this section, the weave types and design of experiments are discussed.

The two types of weave structures considered are the plain weave and twill weave, which were discussed in Section 2.5.2. To characterize the permeability with respect to tightness, a maximum tightness for the weave was determined. The individual

fiber tows of the T-300 3K tow carbon fibers are 1.25 mm in length, as shown in Figure 58. Each tow comprises 3000 individual fibers. The maximum number of tows that can be woven without deforming the carbon fibers is 8 tows/cm. Thus, 8 tows/cm was chosen as the maximum tightness. A woven structure with 8 tows/cm in the warp direction and 8 tows/cm in the weft direction will be classified with a tightness of 8x8.

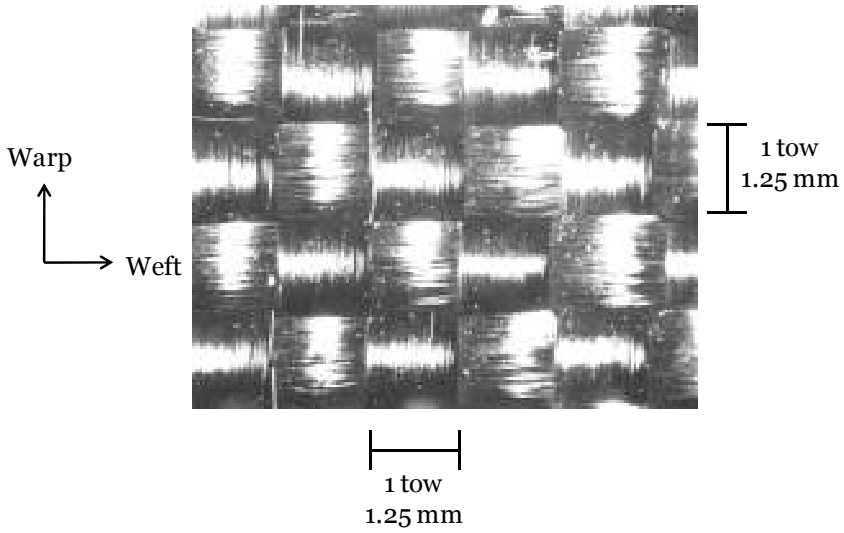

Figure 58: Plain-Woven Fabric with a Tightness of 8x8

The linear fiber density (i.e., the number of fibers per unit length) was varied over a range of tightness for the plain and twill woven fabrics. For instance, 8 tows were maintained in the warp direction while the number of tows in the weft direction ranges from 4 to 8, where an 8x4 is classified as the loosest weave. When the linear density of fibers was less than 4 fibers in the weft direction, the individual tows fall apart, and the sample could not sustain its structure. The samples also could not sustain their structure when the warp fiber linear density was decreased below 8 tows/cm. The two weave types and the respective weave tightnesses are illustrated in Table 20.

Table 20: Weave Samples

Plain (tows/cm, warp x weft)	Twill (tows/cm, warp x weft)
8x8	8x8
8x6	8x6
8x4	8x4

During through-plane testing, the permeability was independent of the weave's placement in the testing device because the flow was perpendicular to the weave pattern. However, during in-plane testing, the flow entered the side of the sample and was parallel to the weave pattern. Thus, the samples were tested in both in-plane directions to investigate the anisotropic in-plane permeability.

5.5 Through-Plane Permeability Results

The through-plane test results are discussed. The test set-up was validated by comparing to results for the same material in literature. Next, the through-plane permeability is tested for 6 types of woven samples (2 weave patterns at 3 tightnesses). The tests are repeated 3 times to ensure repeatability.

5.5.1 Validation

To validate the through-plane test set-up, the through-plane permeability of a SGL 34BA carbon paper was compared to results reported by Gostick et al. [34]. The pressure gradient term was plotted against the mass flux and is shown in Figure 59 for both the validation and data adapted from Gostick et al.

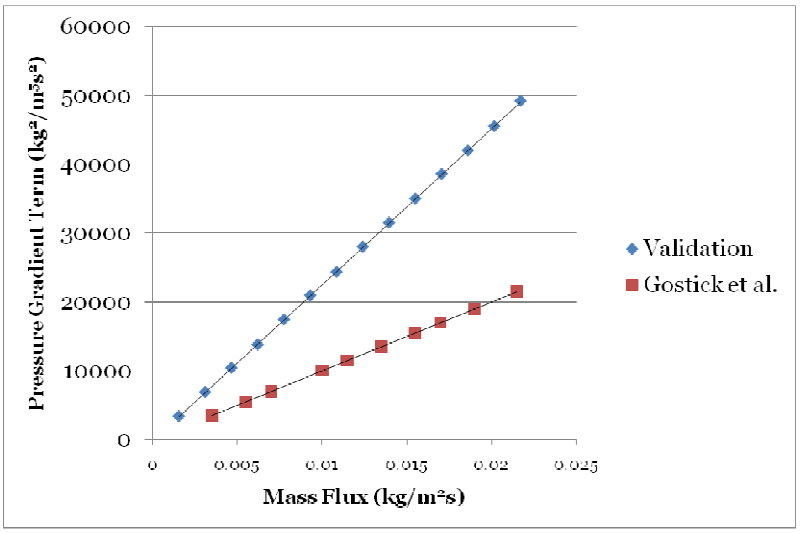

Figure 59: Pressure Gradient Term vs. Mass Flux for Validation

The through-plane permeability of SGL 34BA carbon paper was found to be 8.4 x 10^{-12} m^2, while Gostick et al. reported a value of 16.1 x 10^{-12} m^2 for the same material [34]. While the permeability is ½ the permeability reported by Gostick et al., this is seen as a reasonable result. Because, for a similar material (SGL 10BA), Gostick et al. reported a permeability of 37.4 x 10^{-12} m^2, while Ihonen et al reported a value of 18 x 10^{-12} m^2 [74], which are off by a factor of 2 also. Although the permeability is off by a factor of 2, it is believed that this is insignificant because the range of experimental through-plane permeability reported in the literature is from 10^{-12} to 10^{-10} m^2. Therefore, the through-plane test equipment is considered accurate for the desired measurements.

5.5.2 Through-Plane Permeability of Woven GDLs

The through-plane permeability for the 6 woven samples is shown in Table 21. The reported permeability values are the average permeabilities from 3-4 samples.

Table 21: Through-Plane Permeability of Woven Samples

	Plain Weave		Twill Weave	
	Permeability x 10^{-12} (m^2)	**Average Deviation x 10^{-12} (m^2)**	**Permeability x 10^{-12} (m^2)**	**Average Deviation x 10^{-12} (m^2)**
8x4	12.5	±0.65	57	±3.44
8x6	0.95	±0.10	14.1	±1.4
8x8	2.15	±0.63	5.8	±0.035

It can be seen from Table 21 that the through-plane permeabilities of the twill weaves are higher than the permeabilitoes of the plain weaves. The permeability of 8x4, 8x6, and 8x8 twill weaves compared to the 8x4, 8x6, and 8x8 plain weaves are 4.6, 14.8, and 2.7 times higher respectively. This is consistent with the literature, which states that plain weaves have the lowest permeability.

It is expected that the permeability will increase as the number of weft fibers decreases. This is due to the fact that there is less solid volume and larger pores for the air to pass through. More pores will create less resistance, which should cause higher permeability. This trend is seen with the twill weave, and is shown in Figure 56. However, the same trend is not seen with the plain weave, as shown in Figure 61.

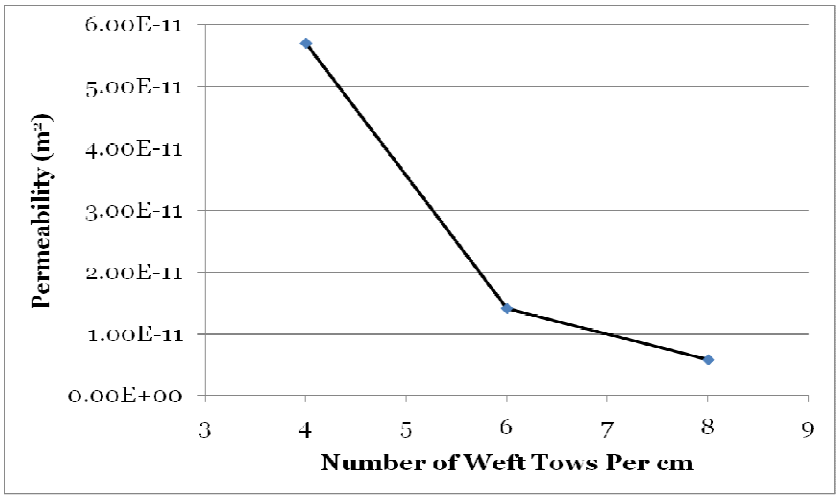

Figure 60: Through-Plane Permeability of Twill Woven GDL with Varying Tightness

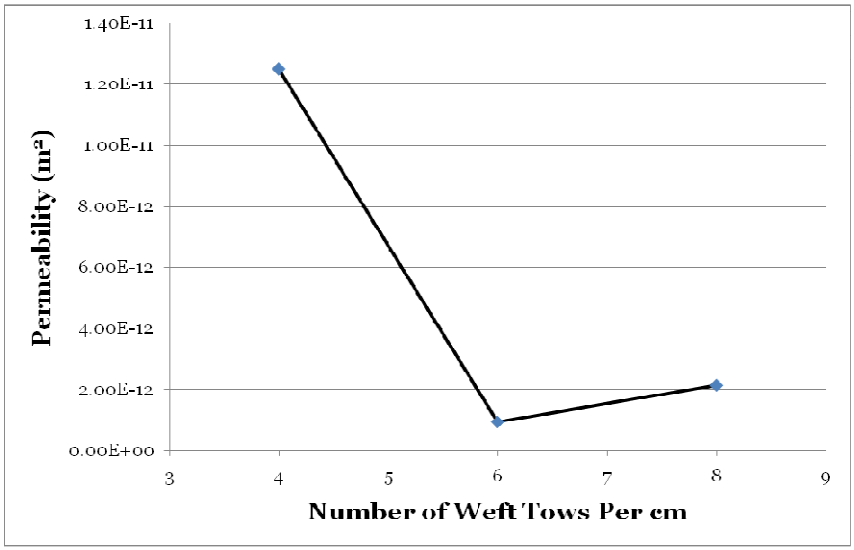

Figure 61: Through-Plane Permeability of Plain Woven GDL with Varying Tightness

In both cases, the permeability was highest for the 8x4 pattern, which was expected. However, for the plain weave the permeability was 2.26 times higher for the 8x8 pattern than the 8x6 pattern, as seen in Figure 61. However, the 8x8 pattern has the most solid volume of carbon fiber per unit area and should have the lowest permeability. To ensure manufacturing error did not play a role in obtaining the unexpected trend,

another batch of plain 8x8 and plain 8x6 samples was made and tested. The same trend was found for the second batch confirming the results from the first tests.

The plain 8x6 and plain 8x8 samples were examined under a microscope to look more closely at the pore structure. It was seen that the 8x8 sample had larger pores between the fibers, which possibly caused the higher permeability. One explanation for this is that the fibers deformed in the in-plane direction during the weaving process.

5.6 In Plane Permeability Results

The in-plane permeability was tested for 6 woven structures at three levels of compression. The permeability at each level of compression was calculated and plotted against the compressed porosity. Using a curve fit and the uncompressed porosity, the uncompressed permeability was calculated. The uncompressed porosity was measured using mercury intrusion porosimetry (MIP). The results of the MIP tests are discussed and related to the calculated permeability values.

5.6.1 Validation

To validate the in-plane test set-up, the in-plane permeability of SGL 34BA by SGL Technologies at a compression of 230 microns was compared to results reported by Gostick et al. [34]. The pressure gradient term was plotted against the mass flux in Figure 62 for both the validation and data adapted from Gostick et al. As seen in Figure 62, the in-plane permeability test set-up built in house was able to closely match the pressure gradient reported by Gostick et al. for SGL 34BA.

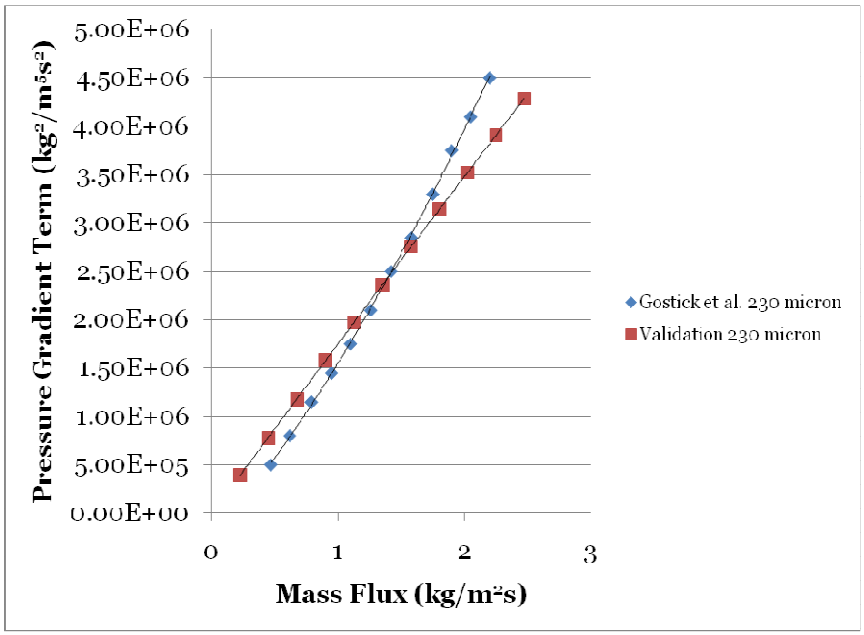

Figure 62: Pressure Gradient Term vs. Mass Flux for Validation

5.6.2 In-plane Permeability of Woven GDLs

The in-plane permeability was measured under three levels of compression over a range of 250-400 µm for the six designs shown in Table 20. The feeler gauge used for each test was dictated by the original thickness of the sample. Tests were repeated for each design, and tests were run to ensure the permeability of the 8x8 samples were transversely isotropic. Samples with a different number of tows/cm in the warp and weft direction (i.e., 8x4, 8x6) were measured in both in-plane directions. To distinguish which direction is measured, the direction reported is the number of tows/cm perpendicular to the flow (e.g., in an 8x4 sample, the 4 direction is the in-plane direction where the impregnating air will encounter 4 tows/cm perpendicular to the direction of flow.) This is illustrated in Figure 63.

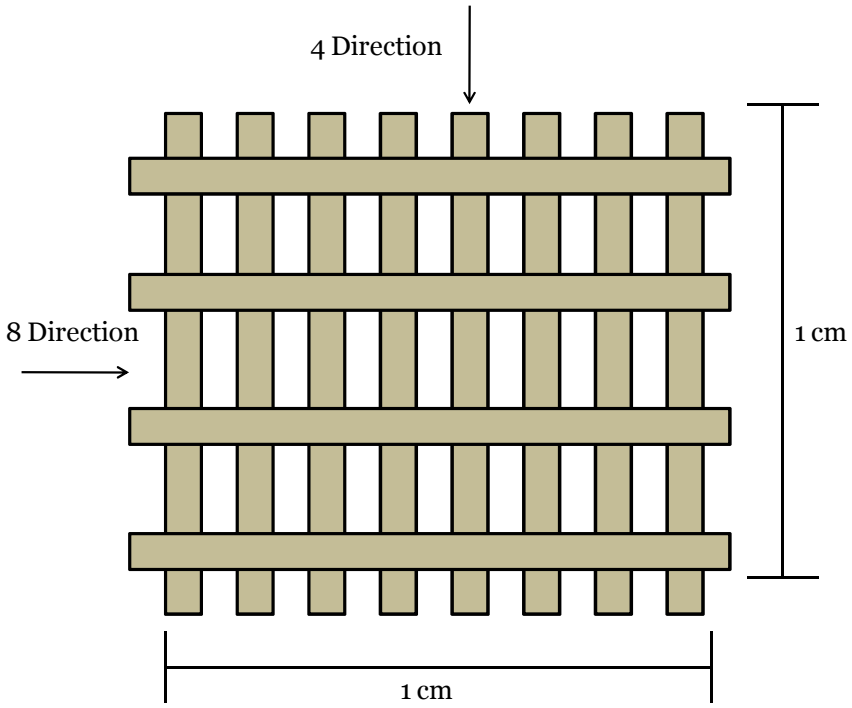

Figure 63: Naming Convention for 8x4 Sample

The uncompressed in-plane permeability for each weave pattern is shown in Table 22. It can be seen that in an anisotropic pattern (i.e., 8x4 or 8x6) the in-plane permeability is consistently higher in the direction where the air flows perpendicular to more tows/cm (i.e., the permeability is higher in the 8 direction than in the 4 direction for an 8x4 pattern). It would be reasonable to assume that the permeability in an 8x4 pattern would be higher than the permeability in an 8x8 pattern. Since there are fewer fibers in an 8x4 pattern, there is less resistance to flow. This trend is seen with the plain weave, where the in-plane permeability for a plain 8x4 in the 8 direction is 39 times higher than the in-plane permeability of a plain 8x8 pattern. However, for the twill weave, the in-plane permeability in the 8-direction has a 2.5% variation between the 8x4 and the 8x6 in the 8 direction. The in-plane permeability is also higher for 8x6 than the 8x4 twill weave in the 8 direction, which is contrary to the expected results.

The inconsistency of in-plane results can be due to the difficulty in testing the samples in the in-plane direction. If the sample is not cut to the exact dimension of the in-plane testing device (1.5 cm x 1.5 cm), air can flow around the sample instead of through the sample. Since the air does not pass through the sample, there is less resistance, and this effect will appear as a decrease in pressure drop, as seen in Figure 64. Care was taken to avoid this problem by placing a sample slightly larger than 1.5 cm into the test platform and cutting the sample down to size while it was in the device. Other causes of error can be the destructive nature of the tests. The same sample was used for all tests of a single pattern. This cycle of recompressing the sample could permanently damage the sample and affect the succeeding results.

Table 22: Uncompressed In-Plane Permeability for Woven Patterns

	8 direction (Permeability x 10^{-12} m^2)	6 direction (Permeability x 10^{-12} m^2)	4 direction (Permeability x 10^{-12} m^2)
Twill 8x8	61.6	**X**	**X**
Twill 8x6	117	109	**X**
Twill 8x4	114	**X**	47.4
Plain 8x8	126	**X**	**X**
Plain 8x6	248	116	**X**
Plain 8x4	4860	**X**	321

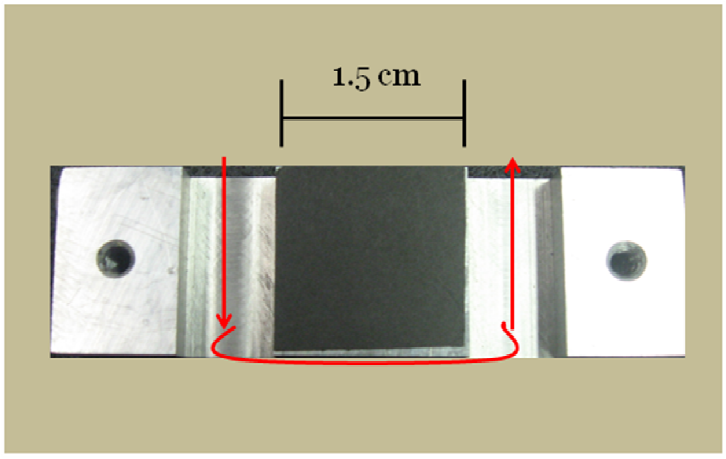

Figure 64: Example of a Sample Slightly Smaller than the In-Plane Test Device Allowing Air to Pass around the Sample Resulting in a Decreased Pressure Drop

Comparing Tables 21 and 22, it can be seen that the in-plane permeabilities are all higher than the through-plane permeabilities with the exception of one weave design, the twill 8x4. The through-plane permeability of the twill 8x4 in the 4 direction is 47.4 x 10^{-12} m^2, while the in-plane permeability of the twill 8x4 is 57 x 10^{-12} m^2, which shows it is possible to create a weave pattern with lower in-plane permeability. To the author's knowledge, there is limited research on the in-plane permeability of woven carbon fiber structures, but research has shown that the permeability of non-woven carbon fibers and carbon papers have a higher in-plane permeability as discussed in Section 2.5.1. From this work, it appears this trend holds true for woven structures, also.

5.6.3 Mercury Intrusion Porosimetry Measurements

To calculate the compressed porosity using the analysis in Section 5.3.2, the uncompressed porosity of the sample is needed. The goal of the study is to find the in-plane permeability of a sample under no compression. However, the in-plane permeability can only be measured under compression because the flow is perpendicular to the direction of compression in an in-plane test. Thus, the uncompressed porosity is needed to calculate the level of compression for each test to extrapolate the uncompressed permeability. Mercury intrusion porosimetry (MIP) is one method to measure the porosity of a porous material. In MIP, a sample is placed in a test chamber, which is evacuated of air. The chamber is filled with mercury, which has a high surface tension, and thus is reluctant to adhere to surfaces. As the pressure is increased, mercury is pushed into the smaller pores. At each incremental pressure increase, the amount of mercury which has not been forced into the pores is measured, and the size of the pores can be calculated. The MIP tests were conducted by Micromeritics Corp., USA, on 2 cm

x 4 cm strips of each weave sample. A hardening resin was spread around the edges of each 2 cm x 4 cm sample on a master sheet of each weave pattern and then cut out to prevent fraying. Further, the resin was used to ensure the weave patterns did not fall apart during transport and testing. The pore size distribution of a plain 8x8 sample is shown in Figure 65, which is typical for other weave designs as well.

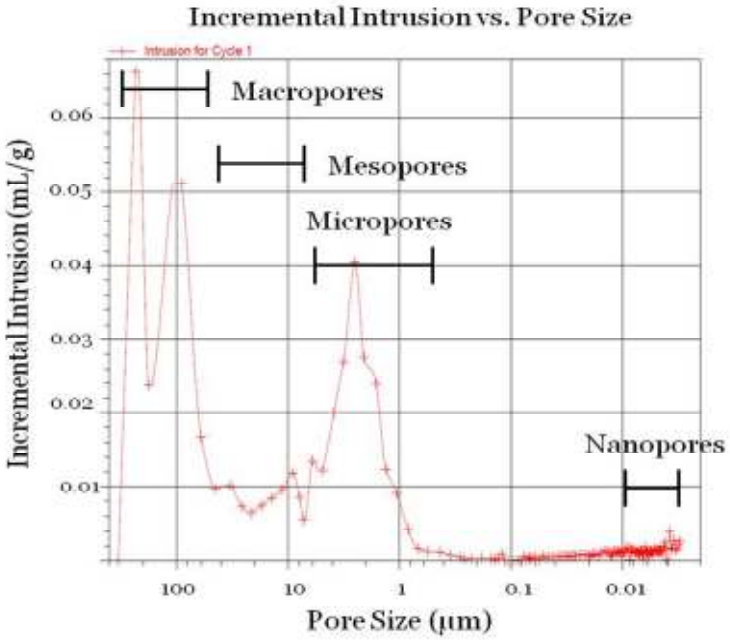

Figure 65: Pore Size Distribution for an 8x8 Plain Weave

From the graph of pore size distribution, Figure 65, four distinct peaks can be seen, which correspond to four different dominant pore sizes. The macropores, 50-400 µm, represent the interfiber pores, or the pores between the individual fiber tows. The mesopores, 5-50 µm, correspond to the pores between the interlacing layers of individual tows, shown graphically in Figure 66. The micropores, 0.5-5 µm, are the intrafiber pores, which are the pores between the individual fibers that make up a single tow. The nanopores, smaller than 0.01 µm, correspond to the actual pores inside a single carbon

fiber and possibly the resin. A plain 8x8 weave pattern is shown under a microscope in Figure 67 (a) and (b), with the macro, micro and nanopores labeled. The mesopores could not be imaged because a cross section would need to be cut from a sample and placed vertically in the microscope. In this configuration, the tows at the edge of the material will fray and make it difficult to see between the interlacing tows.

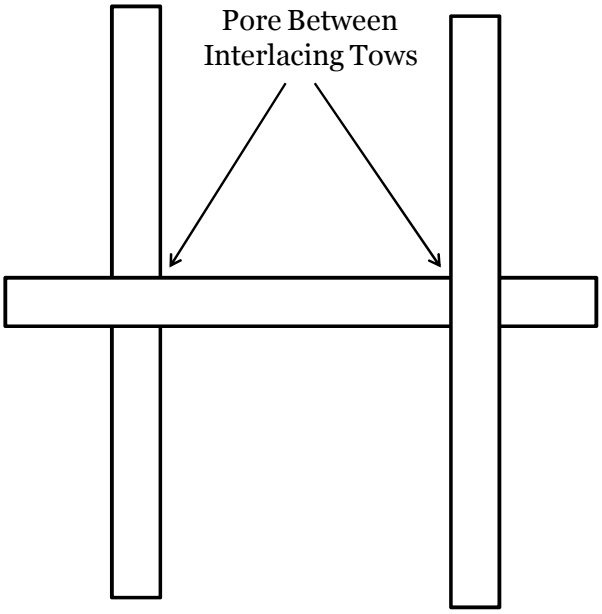

Figure 66: Graphical Representation of the Pores Between Interlacing Tows

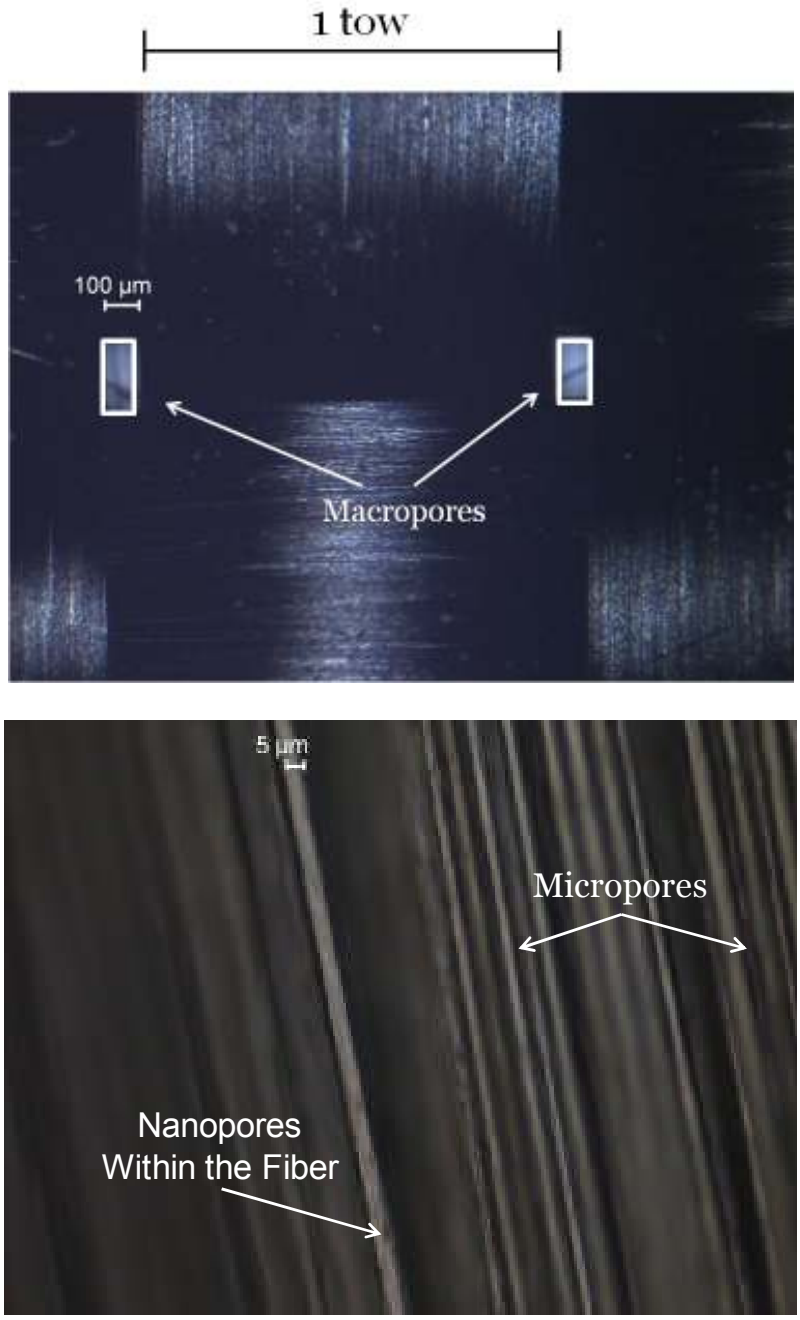

Figure 67: High Resolution Microscope Image of (a) Macropores and (b) Micropores and Nanopores

To find the percentage of each type of pore, the cumulative pore distribution graph, shown in Figure 68, can be used to calculate the percentage of pores in each range. The percentage of each type of pore is shown in Table 23.

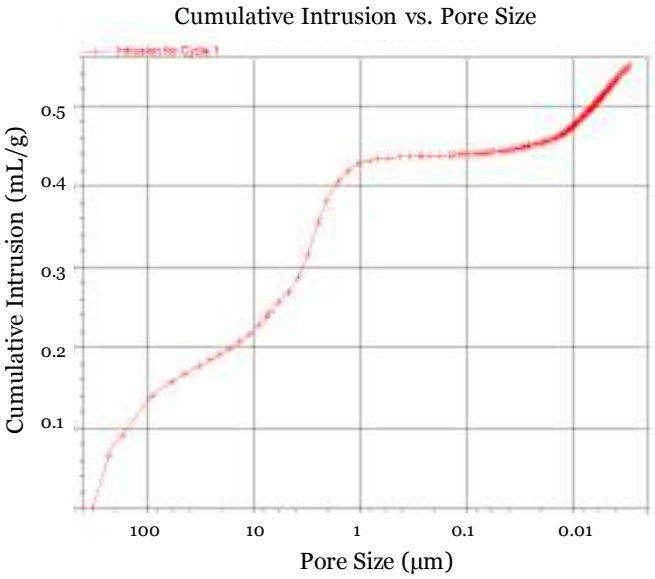

Figure 68: Cumulative Pore Distribution for an 8x8 Plain Weave

Table 23: Percentage of Each Type of Pore Based on Mercury Intrusion Porosimetry

Weave Type	Macro	Meso	Micro	Nano
	50-400 (µm)	5-50 (µm)	0.5-5 (µm)	.005-.03 (µm)
Plain 8x8	29.09%	12.73%	36.36%	21.82%
Plain 8x6	25.00%	17.86%	35.71%	21.43%
Plain 8x4	31.43%	34.28%	20.00%	14.29%
Twill 8x8	30.30%	30.31%	27.27%	12.12%
Twill 8x6	36.84%	26.32%	23.68%	13.16%
Twill 8x4	42.86%	21.42%	21.43%	14.29%

It can be seen from Table 23 that the plain 8x8 sample has a higher percentage of macropores than the plain 8x6 sample. The plain 8x4 sample has the highest number of macropores of the plain weave samples. Referring back to Figure 61, this explains why the through-plane permeability for plain 8x6 weave was lower than the plain 8x8 weave. The percentage of macropores seems to be the driving factor in through-plane permeability. This trend follows for the twill weave samples. The twill 8x4 has the highest percentage of macropores, followed by the twill 8x6 and the twill 8x8. When referring to Figure 60, the twill 8x4 had the highest through-plane permeability, followed

by the twill 8x6 and the twill 8x8, which confirms that the number of macropores is important in determining the through-plane permeability.

CHAPTER 6

CONCLUSIONS

6.1 Overall Conclusions

In this thesis, two numerical studies were conducted to investigate the effect of introducing a graduated permeability profile in the GDL of an unconventional PEM fuel cell on the uniformity of the current density distribution. In addition to permeability, the effect of changing the thickness of the GDL and the stoichiometry of the air supply were considered. An experimental study was also conducted to study the in-plane and through-plane permeabilities through the unconventional GDL to ensure that the permeability of gas through the structure could be controlled.

In the first numerical study, a half-cell model of a PEMFC cathode was built in Fluent version 6.3.26 and used to analyze 3-D single-phase gas flow, and a zero-D equation was used to calculate the gas flow to the current density distribution. It was found that higher in-plane resistance resulted in higher current densities, while the effect of changing the permeability profile on the uniformity could be optimized with different permeability patterns. Thicker GDLs showed higher average current densities due to higher velocities, but the uniformity was independent of thickness. GDLs with a higher air stoichiometry had higher average current densities due to higher velocitites, however the uniformity of the current distribution was not directly correlated to the stoichiometry. A limitation of this model was that the current transport equations were not solved, and the current density was not directly coupled to the mass transport. As such, a second

numerical study was conducted which couples the current equations to mass transport and solves the equations for the electrochemical reactions.

In the second numerical study, a half-cell model of a PEMFC cathode was built in COMSOL Multiphysics version 3.5 and was used to analyze 3-D single-phase flow, which coupled the mass transport to the charge transport. It was found that the permeability profile through the GDL had little effect on the average current density or the uniformity of the current density distribution. The permeability profile had a minimal effect on the current density distribution because the solver increased the pressure at the inlet to overcome the increase in resistance. The pressure profile through the GDL was recorded, and it was found that cases with lower permeability resulted in a higher pressure drop due to increased resistance. Changes in thickness also had little effect on the current density distribution. When studying the effect of changing the gas stoichiometry, it was found that at a stoichiometry of 1, the air was deficient of oxygen near the outlet and the average current density was lower. When increasing the stoichiometry to 2, the average current density increased by 12%. Further increases in stoichiometry from 2 to 4 resulted in only a 4.2% increase in the current density. It can be concluded that once the fuel cell has enough oxygen to sustain the reactions, pumping more oxygen into the cell will not significantly increase the average current density.

In the experimental study, the through-plane permeability and in-plane permeability were measured for 6 different weave patterns. The pore structure was analyzed with mercury intrusion porosimetry and a high resolution microscope. It can be concluded that the plain weave has a lower through-plane permeability than the twill weave. According to the analysis of the pore structure, the macropores, pores greater

than 50 microns, are a driving factor in determining the through-plane permeability. The in-plane permeability for the woven structures was higher than the through-plane permeability, with the exception of the twill 8x4 weave in the 4 direction which showed a through-plane permeability which was 20% higher than the in-plane permeability. This shows it is possible to create a weave pattern with higher through-plane permeability than in-plane permeability. However, the woven structures generally followed the same trend of non-woven structures, which show higher in-plane permeability than through-plane permeability.

6.2 Contributions

While it was found that a graduated permeability does not affect the performance when considering gas flow, this thesis lays the ground work for a future study in which two-phase (i.e., gas and liquid water) permeability in the GDL of the unconventional GDL is considered. When comparing the results in Chapter 3 and 4, the expected current densities at the GDL/catalyst interface were very different. This underlines the importance of coupling current transport to differential equations that govern mass transport in electrochemical modeling.

This thesis shows it is possible to create a GDL with a higher through-plane permeability than in-plane permeability, which has not been shown in literature. While work has been conducted to study permeability of commercial GDLs, this is the first study to try to characterize a relationship between the in-plane and through-plane permeability of woven GDLs based on structure (i.e., weave pattern and tightness). This thesis serves as a starting point for future studies to quantify the relationship between the

structure and the permeability, and also the correlation between the pore structure and the permeability.

CHAPTER 7

FUTURE WORK

7.1 Simulations

The goal of the numerical simulations discussed in Chapters 3 and 4 was to regulate the permeability to create a uniform current density profile. Since the permeability was found to have little effect on the current density profile, other factors that affect the permeability should be considered. One factor that affects the current density is the reaction rate at the catalyst layer. There are several ways to increase the reaction rate at the catalyst layer such as increasing the platinum loading or increasing the surface area of the catalyst active area by increasing the roughness of the surface [3, 75]. Increasing the reaction rate is captured by the modeling parameter, ai_{0c}, which represents the surface area multiplied by the exchange current density. For the study in chapter 4, this variable was kept constant at 120 A/m^3. It would be interesting to see if graduating the consumption rate would help produce a more uniform current density, which is suggested by Baghdadi [32]. A graphical representation of this concept is shown in Figure 69.

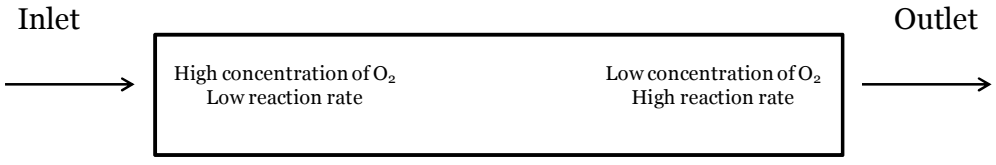

Figure 69: Graded Reaction Rate due to Non-Uniform Catalyst Loading as Oxygen is Consumed through the Cell

A preliminary study was run in which ai_{0c} was increased as a linear function based on position. This is much like the increasing permeability profile in the aforementioned simulations. At the exit, ai_{0c} is set to 120 A/m^3. The starting values of ai_{0c}, the average current density and the ratio are shown in Table 24.

Table 24: Current Density as a Function of Rate of Consumption, ai_{0c}

Range of ai_{0c} (A/m^3)	Average Current Density (A/cm^2)	Standard Deviation of Current Density (A/cm^2)	Ratio of Std. Deviation/Average Current Density
10 – 120	0.871	0.094	0.108
40 – 120	0.930	0.027	0.029
50 – 120	0.944	0.016	0.017
55 – 120	0.950	0.012	0.013
60 – 120	0.957	0.011	0.011
65 – 120	0.963	0.012	0.012
70 – 120	0.968	0.015	0.015
120 (constant)	1.015	0.048	0.047

It is observed that as the value of ai_{0c} near the inlet increases, the average current density increases. This is because the catalyst can utilize more of the fuel. When comparing the standard deviation of current density and the ratio of the standard deviation to the average current density for all simulations, it is found that there exists an optimum, as evidenced by the lower ratio. The optimum occurs when the starting value of ai_{0c} is at 60 [A/m^3]. This suggests that it is possible to obtain a better current density distribution with non-uniform catalyst loading. This study does not take into account effects of non-uniform heat generation and the effects on conductivity. A future study

which takes into account the heat generation coupled to two-phase water transport will be necessary for further optimization.

7.2 Permeability Testing

The goal of chapter 5 was to create an anisotropic permeability pattern with higher through-plane permeability than in-plane permeability by varying the weave tightness for two different weave patterns. It was found that the in-plane permeability was higher than the through-plane permeability, which is consistent with literature on non-woven GDLs. One exception is an 8x4 twill weave in the 4 direction, in which the through-plane permeability was 20% higher than the in-plane permeability. This shows it is possible to manufacture a GDL with higher through-plane permeability. In future work, different woven materials could be tested. Materials with a lower number of fibers per tow could be tested, and the durability of the materials could be tested to make sure the GDL will be able to sustain the stresses of operation and compare to the lifetime of conventional systems. Two weave patterns, plain and twill weave, were considered in this study. In future work, more weave patterns could be tested. Since water is created in fuel cell cathodes, water could be used as the impregnating fluid to test the relative liquid permeability and compare to the gas permeability. It would also be interesting to test the conductivity of different woven structures. While a more porous structure improves gas transport, higher porosity causes an increase in contact resistance due to lower electrical conductivity of air. Ideally, GDLs with different woven patterns could be tested in a fuel cell to investigate the trade-off between conductivity and air permeability.

REFERENCES

1. *U.S. Energy Information Administration Independent Statistics and Analysis*. 2010 [cited 2010 2/9]; Available from: http://www.eia.doe.gov/cneaf/electricity/epm/table1_1.html.

2. Snyder, B. and M.J. Kaiser, *Ecological and economic cost-benefit analysis of offshore wind energy.* Renewable Energy, 2009. **34**(6): p. 1567-1578.

3. O'Hayre, R., et al., *Fuel Cell Fundamentals*. 2009, Hoboken, NJ: John Wiley and Sons.

4. Larminie, J. and A. Dicks, *Fuel Cell Systems Explained*. 2003, West Sussex, England: John Wiley and Sons Ltd.

5. Campanari, S., G. Manzolini, and F. Garcia de la Iglesia, *Energy analysis of electric vehicles using batteries or fuel cells through well-to-wheel driving cycle simulations.* Journal of Power Sources, 2009. **186**(2): p. 464-477.

6. Caux, S., et al., *On-line fuzzy energy management for hybrid fuel cell systems.* International Journal of Hydrogen Energy, 2010. **35**(5): p. 2134-2143.

7. *Flow Field Designs*. [cited 2010 3-29]; Available from: http://www.me.udel.edu/research_groups/prasad/proj/img/PIV_fig1.jpg.

8. Barreras, F., et al., *Fluid dynamics performance of different bipolar plates: Part I. Velocity and pressure fields.* Journal of Power Sources, 2008. **175**(2): p. 841-850.

9. Boddu, R., et al., *Development of bipolar plates with different flow channel configurations for fuel cells.* Journal of Power Sources, 2009. **189**(2): p. 1083-1092.

10. Kumar, A. and R.G. Reddy, *Effect of gas flow-field design in the bipolar/end plates on the steady and transient state performance of polymer electrolyte membrane fuel cells.* Journal of Power Sources, 2006. **155**(2): p. 264-271.

11. Li, X. and I. Sabir, *Review of bipolar plates in PEM fuel cells: Flow-field designs.* International Journal of Hydrogen Energy, 2005. **30**(4): p. 359-371.

12. Wang, L. and H. Liu, *Performance studies of PEM fuel cells with interdigitated flow fields.* Journal of Power Sources, 2004. **134**(2): p. 185-196.

13. Yan, W.-M., et al., *Effects of operating conditions on cell performance of PEM fuel cells with conventional or interdigitated flow field.* Journal of Power Sources, 2006. **162**(2): p. 1157-1164.

14. Zhang, G., et al., *Comparison of current distributions in proton exchange membrane fuel cells with interdigitated and serpentine flow fields.* Journal of Power Sources, 2009. **188**(1): p. 213-219.

15. Gerteisen, D., T. Heilmann, and C. Ziegler, *Modeling the phenomena of dehydration and flooding of a polymer electrolyte membrane fuel cell.* Journal of Power Sources, 2009. **187**(1): p. 165-181.

16. Cindrella, L., et al., *Gas diffusion layer for proton exchange membrane fuel cells--A review.* Journal of Power Sources, 2009. **194**(1): p. 146-160.

17. Litster, S. and G. McLean, *PEM fuel cell electrodes.* Journal of Power Sources, 2004. **130**(1-2): p. 61-76.

18. Wang, Y., C.-Y. Wang, and K.S. Chen, *Elucidating differences between carbon paper and carbon cloth in polymer electrolyte fuel cells.* Electrochimica Acta, 2007. **52**(12): p. 3965-3975.

19. Reddy, R.G., *Fuel cell and hydrogen economy.* Journal of Materials Engineering and Performance, 2006. **15**(4): p. 474-483.

20. Hermann, A., T. Chaudhuri, and P. Spagnol, *Bipolar plates for PEM fuel cells: A review.* International Journal of Hydrogen Energy, 2005. **30**(12): p. 1297-1302.

21. Yousfi-Steiner, N., et al., *A review on PEM voltage degradation associated with water management: Impacts, influent factors and characterization.* Journal of Power Sources, 2008. **183**(1): p. 260-274.

22. Bhamidipati, K.L., et al., *Numerical Simulation of an Innovative PEM Fuel Cell Stack*, in *Sixth International Fuel Cell Science, Engineering and Technology Conference*. 2008: Denver, Colorodo.

23. *Internal Manifolding*. [cited 2010 3-29]; Available from: http://www.sovereign-publications.com/images/ballard/PEM-fuel-cell-large.jpg.

24. Min, C.H., et al., *Parameter sensitivity examination and discussion of PEM fuel cell simulation model validation: Part II: Results of sensitivity analysis and validation of the model.* Journal of Power Sources, 2006. **160**(1): p. 374-385.

25. Weber, A.Z. and J. Newman, *Modeling Transport in Polymer-Electrolyte Fuel Cells.* Chemical Reviews, 2004. **104**(10): p. 4679-4726.

26. Gurau, V., T.A.Z. Jr., and J.A.M. Jr., *Two-Phase Transport in PEM Fuel Cell Cathodes.* Journal of Fuel cell Science and Technology, 2008. **5**.

27. Sun, W., B.A. Peppley, and K. Karan, *Modeling the Influence of GDL and flow-field plate parameters on the reaction distribution in the PEMFC cathode catalyst layer.* Journal of Power Sources, 2005. **144**(1): p. 42-53.

28. Ubong, E.U., Z. Shi, and X. Wang, *Three-Dimensional Modeling and Experimental Study of a High Temperature PBI-Based PEM Fuel Cell.* Journal of the Electrochemical Society, 2009. **156**(10): p. B1276-B1282.

29. Wu, J. and Q. Liu, *Simulation-Aided PEM Fuel Cell Design and Performance Evaluation.* Journal of Fuel cell Science and Technology, 2005. **2**.

30. Yi, J.S. and T.V. Nguyen, *Multicomponent Transport in Porous Electrodes of Proton Exchange Membrane Fuel Cells Using the Interdigitated Gas Distributors.* Journal of the Electrochemical Society, 1999. **146**(1): p. 38-45.

31. Zamel, N. and X. Li, *A parametric study of multi-phase and multi-species transport in the cathode of PEM fuel cells.* International Journal of Energy Research, 2007. **32**.

32. Sadiq Al-Baghdadi, M.A.R., *Performance comparison between airflow-channel and ambient air-breathing PEM fuel cells using three-dimensional computational fluid dynamics models.* Renewable Energy, 2009. **34**(7): p. 1812-1824.

33. Schmitz, A., et al., *Modelling Approach for Planar Self-Breathing PEMFC and Comparison with Experimental Results.* Fuel Cells, 2004. **4**(4).

34. Gostick, J.T., et al., *In-plane and through-plane gas permeability of carbon fiber electrode backing layers.* Journal of Power Sources, 2006. **162**(1): p. 228-238.

35. Hwang, J.J., et al., *A three-dimensional numerical simulation of the transport phenomena in the cathodic side of a PEMFC.* Journal of Applied Electrochemistry, 2004. **34**.

36. Hwang, J.J., et al., *Mass/electron co-transports in an air-breathing cathode of a PEM fuel cell.* Journal of Power Sources, 2006. **160**(1): p. 18-26.

37. Shimpalee, S., U. Beuscher, and J.W. Van Zee, *Investigation of gas diffusion media inside PEMFC using CFD modeling.* Journal of Power Sources, 2006. **163**(1): p. 480-489.

38. Yu, L.-j., et al., *Transport mechanisms and performance simulations of a PEM fuel cell with interdigitated flow field.* Renewable Energy, 2009. **34**(3): p. 530-543.

39. Zhang, Z., et al., *Optimizing the Performance of a Single PEM Fuel Cell.* Journal of Fuel cell Science and Technology, 2008. **5**.

40. Zhukovsky, K.V., *Three Dimensional Model of Oxygen Transport in a Porous Diffuser of a PEM Fuel Cell.* AIChE Journal, 2003. **49**(12).

41. Miao, Z., Y.-L. He, and J.-Q. Zou, *Modeling the effect of anisotropy of gas diffusion layer on transport phenomena in a direct methanol fuel cell.* Journal of Power Sources, 2010. **195**(11): p. 3693-3708.

42. Pharoah, J.G., *On the permeability of gas diffusion media used in PEM fuel cells.* Journal of Power Sources, 2005. **144**(1): p. 77-82.

43. Chen, F., M.-H. Chang, and P.-T. Hsieh, *Two-phase transport in the cathode gas diffusion layer of PEM fuel cell with a gradient in porosity.* International Journal of Hydrogen Energy, 2008. **33**(10): p. 2525-2529.

44. Chu, H.-S., C. Yeh, and F. Chen, *Effects of porosity change of gas diffuser on performance of proton exchange membrane fuel cell.* Journal of Power Sources, 2003. **123**(1): p. 1-9.

45. Tomadakis, M.M. and T.J. Robertson, *Viscous Permeability of Random Fiber Structures: Comparison of Electrical and Diffusional Estimates with Experimental and Analytical Results.* Journal of Composite Materials, 2005. **39**(2).

46. Tomadakis, M.M. and S.V. Sotirchos, *Ordinary and transition regime diffusion in random fiber structures.* AIChE Journal, 1993. **39**(3): p. 397-412.

47. Tomadakis, M.M. and S.V. Sotirchos, *Effective diffusivities and conductivities of random dispersions of nonoverlapping and partially overlapping unidirectional fibers.* The Journal of Chemical Physics, 1993. **99**(12): p. 9820-9827.

48. Tomadakis, M.M. and S.V. Sotirchos, *Transport properties of random arrays of freely overlapping cylinders with various orientation distributions.* The Journal of Chemical Physics, 1993. **98**(1): p. 616-626.

49. Nitta, I., et al., *Modelling the Effect of Inhomogeneous Compression of GDL on Local Transport Phenomena in a PEM Fuel Cell.* Fuel Cells, 2008. **8**(6).

50. Feser, J.P., A.K. Prasad, and S.G. Advani, *Experimental characterization of in-plane permeability of gas diffusion layers.* Journal of Power Sources, 2006. **162**(2): p. 1226-1231.

51. Gurau, V., et al., *Characterization of transport properties in gas diffusion layers for proton exchange membrane fuel cells: 2. Absolute permeability.* Journal of Power Sources, 2007. **165**(2): p. 793-802.

52. Ismail, M., et al., *Through-Plane Permeability for Untreated and PTFE-Treated Gas Diffusion Layers in Proton Exchange Membrane Fuel Cells*, in *Seventh International Fuel Cell Science, Engineering and Technology Conference*. 2009: Newport Beach, California.

53. Williams, M.V., et al., *Characterization of Gas Diffusion Layers for PEMFC.* Journal of the Electrochemical Society, 2004. **151**(8).

54. Ogulata, R.T., *Air Permeability of Woven Fabrics.* Journal of Textile and Apparel, Technology and Management, 2006. **5**(2).

55. Feather, D.G. and S.L. Anderson, *Some Physical Properties of a Range of Worsted Fabrics.* Journal of the Textile Institute, 1967. **58**(6).

56. Epps, H.H. and K.K. Leonas, *The Relationship Between Porosity and Air Permeability of Woven Textile Fabrics.* Journal of Testing and Evaluation, 1997. **25**(1).

57. Birgersson, E. and M. Vynnycky, *A quantitative study of the effect of flow-distributor geometry in the cathode of a PEM fuel cell.* Journal of Power Sources, 2006. **153**(1): p. 76-88.

58. Gurau, V., F. Barbir, and H. Liu, *An Analytical Solution of a Half-Cell Model for PEM Fuel Cells.* Journal of the Electrochemical Society, 2000. **147**(7): p. 2468-2477.

59. Sui, P.C. and N. Djilali, *Analysis of coupled electron and mass transport in the gas diffusion layer of a PEM fuel cell.* Journal of Power Sources, 2006. **161**(1): p. 294-300.

60. Parvazinia, M., et al., *Finite Element Modeling of Flow Through a Porous Medium Between Two Parallel Plates Using the Brinkman Equation.* Transport in Porous Media, 2006. **63**: p. 71-90.

61. Wang, X.-D., et al., *Effects of flow channel geometry on cell performance for PEM fuel cells with parallel and interdigitated flow fields.* Electrochimica Acta, 2008. **53**(16): p. 5334-5343.

62. Caston, T.B., et al., *Graduated Flow Resistance Through a GDL in a Novel PEM Stack*, in *Seventh International Fuel Cell Science, Engineering and Technology Conference*. 2009: Newport Beach, California.

63. Wang, Y. and C.-Y. Wang, *Modeling Polymer Electrolyte Fuel Cells with Large Density and Velocity Changes.* Journal of the Electrochemical Society, 2005. **152**(2).

64. Kurgan, E. and P. Schmidt, *Distribution of the potential and current density in the electrode of the PEM fuel cell.* COMPEL: The International Journal for Computation and Mathematics in Electrical and Electronic Engineering, 2006. **25**(1).

65. Bernardi, D.M. and M.W. Verbrugge, *A Mathematical Model of the Solid-Polymer-Electrolyte Fuel Cell.* Journal of the Electrochemical Society, 1992. **139**(9).

66. Wöhr, M., et al., *Dynamic modelling and simulation of a polymer membrane fuel cell including mass transport limitation.* International Journal of Hydrogen Energy, 1998. **23**(3): p. 213-218.

67. Shimpalee, S., et al., *Predicting the transient response of a serpentine flow-field PEMFC: II: Normal to minimal fuel and AIR.* Journal of Power Sources, 2006. **156**(2): p. 369-374.

68. Berg, P., et al., *Water Management in PEM Fuel Cells.* Journal of the Electrochemical Society, 2004. **151**(3).

69. Chedester, C.R., *Transport phenomena in microchannels and proton exchange membrane assemblies of fuel cells*, in *Mechanical Engineering*. 2002, Georgia Institute of Technology: Atlanta, GA. p. 175.

70. Hung, A.-J., et al., *Operation-relevant modeling of an experimental proton exchange membrane fuel cell.* Journal of Power Sources, 2007. **171**(2): p. 728-737.

71. Yuan, W., et al., *Model prediction of effects of operating parameters on proton exchange membrane fuel cell performance.* Renewable Energy, 2010. **35**(3): p. 656-666.

72. *Comsol Multiphysics User's Guide Version 3.5a*.

73. *Viscosity calculator*. Available from: http://www.lmnoeng.com/Flow/GasViscosity.htm.

74. Ihonen, J., M. Mikkola, and G. Lindbergh, *Flooding of Gas Diffusion Backing in PEFCs.* Journal of the Electrochemical Society, 2004. **151**(8): p. A1152-A1161.

75. Litster, S., et al., *Computational analysis of heat and mass transfer in a micro-structured PEMFC cathode.* Journal of Power Sources, 2006. **156**(2): p. 334-344.